Scholars' Mine

Fall 2012

Process simulation and inclusion characterization in stainless steel ingot casting

Jun Ge

Recommended Citation

PROCESS SIMULATION AND INCLUSION CHARACTERIZATION IN

STAINLESS STEEL INGOT CASTING

By

JUN GE

A THESIS

Presented to the Faculty of the Graduate School of the

MISSOURI UNIVERSITY OF SCIENCE AND TECHNOLOGY

In Partial Fulfillment of the Requirements for the Degree

MASTER OF SCIENCE

In

MATERIAL ENGINEERING

2012

Approved by

Lifeng Zhang, Advisor
Kent Peaslee, Co-Advisor
Von Richards

iii

ABSTRACT

For the ingot casting process, fluid flow of steel plays an important role in quality control and industrial operations. Using CFD software (FLUENT), this study overviews the fluid flow pattern in the bottom-teeming ingot filling process with three different swirl-modified upgate designs. Turbulent flow and mass transfer are considered main factors in controlling the process. The motion of the slag phase was also considered. In addition to the modeling studies, inclusions in stainless steel poured into ingots with a traditional and a swirl-modified upgate system were investigated using an optical microscope, SEM-EDS and ASPEX automated feature analysis technology. The main inclusions observed were Al_2O_3, MnS, and oxide-sulfide. This work provides a comprehensive description and understanding of the morphology and distribution of inclusions in bottom-poured ingot casting. Fewer inclusions were observed at the center and mid-radius of the swirl-modified ingot than that of the traditional ingot. More inclusions were found at the center of the ingot than nearer the walls. The re-designed upgate system did have positive effect on the flow pattern in the ingot and indirectly cause fewer inclusions in size range of 0~10μm, but made no major difference beyond the change in the smallest size range.

ACKNOWLEDGMENTS

TABLE OF CONTENTS

LIST OF ILLUSTRATIONS

LIST OF TABLES

NOMENCLATURE

Symbol	Description
β	Angle of Attack
α	Change in Coupler Angle

1. INTRODUCTION AND LITERATURE REVIEW

1.1. INGOT CASTING PROCESS

Although more and more industrial facilities have replaced ingot casting with continuous casting due to advantages like high quality and high yield, ingot casting as a traditional steel making technology still has considerable use in industry for large forgings and rolled products and therefore has value for investigation. Ingot cast material accounts for 5.0% of the total world steel production, which contains special applications and different grades [1]. The use of special steels with improved toughness, ductility, and fatigue life in industry is becoming increasingly widespread [2]. Ingot casting is still the first choice for the steel industry in some of the low alloy steels, most of the high alloy steels and specialty steels including high carbon chromium bearing steel for thick plate, seamless tube, and bars for forging. The production of crude steel ingots in 2011 was about 2.1 million metric tons in United States, 12.0 million metric tons in China, and 71.0 million metric tons worldwide [1].

Casting is a process, wherein liquid metal is poured from the ladle into the mold where it solidifies. Ingot casting is usually bottom poured to take advantage of quality advantages including fewer defects on the surface and inside of ingots (Figure 1.1).
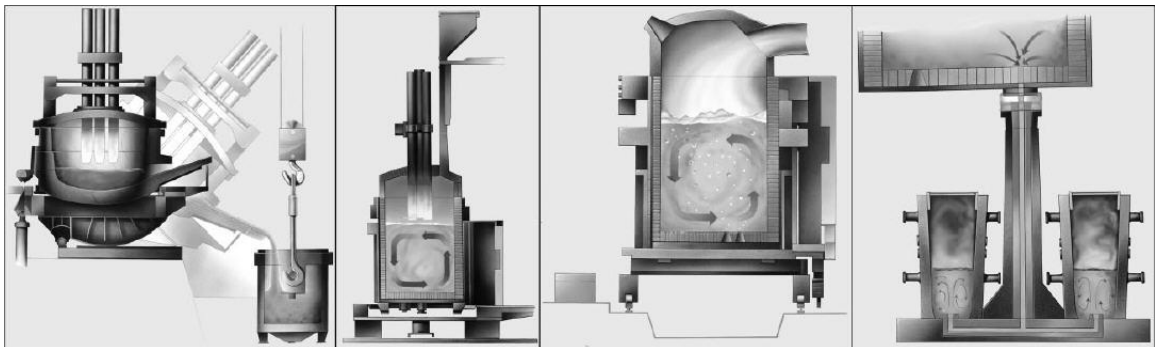
Figure 1.1 General Process of Ingot Casting [1]

Most ingot casting plants melt in electric arc furnaces followed by a variety of steel refining processes which could include ladle metallurgy treatments such as ladle stirring, vacuum degassing, and calcium treatment. After reaching the proper composition and temperature, heats are bottom teemed into ingots at a designated temperature and a controlled rate. Argon shrouding may be employed during teeming to minimize the re-oxidation and the pick-up of hydrogen and nitrogen.

During teeming, molten steel flows through the well and slide gate at the bottom of the ladle, entering the trumpet and passing through the spider into the runners. The system is often flooded with inert gas to minimize re-oxidation. Molten steel then enters the ingot mold through an upward-facing ingate near the end of the runner. The rising steel level burns through suspended bags to release mold powder. The powder spreads and melts to form a slag layer, floating on top of the molten steel, which protects the molten steel from oxidation and absorbs part of the inclusions. After teeming, the ingot remains in place to solidify for the optimal time for easy removal from the mold.

1.2. INCLUSIONS AND CLEANLINESS OF STEEL

The ever-increasing demands for higher quality have made steelmakers increasingly aware of the necessity for production to meet stringent "cleanliness" requirements [4]. To lower the content of non-metallic oxide inclusions and control their morphology, size distribution, and composition, clean steel requires control of sulfur, phosphorous, hydrogen, nitrogen and carbon, minimizing metallic impurity elements such as As, Sn, Sb, Se, Cu, Zn, Pb, Cd, Te and Be [5]. In the process of casting, which is the last step of steelmaking, inclusions can be either removed from or introduced into the steel. Inclusion size distribution is particularly important to steel cleanliness, because large macro inclusions are detrimental to mechanical properties. Table 1.1 shows typical restrictions of maximum inclusion size for many products [6].

Table 1.1 Typical Steel Cleanliness Requirements Reported for Various Steel Grades [6]

Steel products	Maximum steel fraction	Maximum inclusion size
IF steel	[C]≤30ppm, [N] ≤40ppm, T.O. ≤40ppm	
Automotive & deep-drawing sheet	[C]≤30ppm, [N] ≤30ppm	100μm
Drawn and ironed cans	[C]≤30ppm, [N] ≤30ppm, T.O. ≤20ppm	20μm
Alloy steel for pressure vessels	[P]≤70ppm	
Alloy steel bars	[H]≤2ppm, [N] ≤10-20ppm, T.O. ≤10ppm	
HIC resistance steel (sour gas tubes)	[P]≤50ppm, [S] ≤10ppm	
Line pipes	[S]≤30ppm, [N] ≤35ppm, T.O. ≤30ppm	100μm
Sheet for continuous annealing	[N]≤20ppm	
Plate for welding	[H]≤1.5ppm	
Ball bearings	T.O. ≤10ppm	15μm
Tire cord	[H]≤2ppm, [N] ≤40ppm, T.O. ≤15ppm	10μm
Non-grain-orientated Magnetic sheet	[N]≤30ppm	
Heavy plate sheet	[H]≤2ppm, [N] ≤30-40ppm, T.O. ≤20ppm	Single 13μm Cluster 200μm
Wire	[N] ≤60ppm, T.O. ≤30ppm	20μm
Electric sheet	[N] ≤20ppm	
Electric resistance weld pipe		150μm
Offshore steel	[N] ≤80ppm	
Rail steel	[H]≤1.5ppm	
Shadow mask for CRT		5μm
Source gas pipes plus sulfide shape control	[S] ≤10ppm	

1.2.1. Methods of Steel Cleanliness Measurements. In order to evaluate steel cleanliness, measurement ranges from direct methods to indirect methods. There are two categories of direct methods, inclusion evaluation of solid steel sections and of solid steel volumes [5]. Methods for inclusion evaluation of solid steel sections includes metallographic microscope, image analysis, scanning electron microscope, optical spectrometry with pulse discrimination analysis, laser microprobe mass spectrometry, X-ray photoelectron spectroscopy [6]. Conventional ultrasonic scanning, scanning acoustic

microscope, X-ray detection, slime electrolysis, electron beam melting, cold crucible melting, and fractional thermal decomposition are methods to evaluate solid steel volume [6]. Coulter counter analysis, photo scattering, and laser-diffraction particle size analysis are methods for evaluating the inclusion size distribution after inclusion extraction [6]. Ultrasonic techniques for liquids and liquid metal cleanliness analysis are methods for inclusion evaluation in liquids. For indirect methods, total oxygen and nitrogen are the two main measurements used to indicate the level of inclusion content [6].

1.2.2. Relation Between Mechanical Properties of Steel and Inclusions. The mechanical properties of steel are significantly affected by the volume fraction, size distribution, composition and morphology of nonmetallic inclusions. Metallic impurity elements, which are traditionally found only in trace amounts, are becoming an increasing problem due to their accumulation in the scrap supply. These elements cause intergranular segregation leading to cracks, detrimental precipitates and other problems, which are often manifested as slivers in the final product [4]. Ductility decreases when the amounts of oxide or sulfide inclusions increase. Fracture toughness will be lower with more inclusions especially in higher-strength low ductility steels. Long stringer macro inclusions are found to be responsible for cyclic fatigue stress failure [5]. The presence of hard spinel inclusions, even small in size, has a detrimental effect on the polishability of steel [3]. Inclusions also cause voids, which will induce cracks if larger than a critical value. Large exogenous inclusions cause inferior surface appearance, poor polishability, reduced resistance to corrosion, and, in severe cases, laminations. The source of most fatigue problems in steel are hard and brittle oxide inclusions. Large inclusions have a more negative effect on the fatigue life than smaller ones. In general, rolling contact fatigue life decreases as the total oxygen content increases [4]. Ultra-clean, high-strength steels with improved properties at high temperature are required by modern industries like power plants. Strict requirements of sulfur content (max. 0.004 wt%) and deoxidizing elements are demanded for those steels. In order to avoid these problems, the size and frequency of detrimental inclusions must be carefully controlled. The life of bearing steels greatly depends on controlling the amount of nonmetallic inclusions (especially hard and large aluminum oxides). Although the solidification morphology of inclusions is of most importance in steel castings, the morphology of inclusions in

wrought products is largely controlled by their mechanical behavior during steel processing.

1.2.3. Inclusion Classification and Their Formation. Dekkers has classified inclusions into spherical, faceted, platelike inclusions, dendrites, clusters and aggregates with respect to size and composition in low carbon steel [7]. Small spherical inclusions could account for a large part of the inclusions observed; however, large inclusions which are mostly represented by oxides are considered more detrimental for global steel quality [7]. Two types of alumina containing inclusions are typically found in ingot cast tool steel generated from reoxidation [8]. Park found that inclusions in stainless steel could contain alumina even when the steel was mainly deoxidized by silicon; moreover, one type of spinel inclusion $MgO-Al_2O_3$ could crystallize in the calcium silicate matrix [9]. Tripathi and Sichen show that the increase in sulfur activity of the steel melt during casting is the cause of the formation of oxy sulfide and calcium sulfide phases in the inclusions in aluminum killed tool steel [10]. A recent research paper of Doostmohammadi shows that sulfides dominate other types of inclusions in the size range larger than 1 µm and oxide inclusions with a sulfide layer are often found in bearing steels by ingot casting [11]. In Dub's work, aluminates have been classified into five types with different molecular ratios between Al_2O_3 and CaO [12]. Globular inclusions and stringers are the main shape of aluminates and sulfides [12]. Gigovic states that the excessive content of sulfur in the raw material could be the reason for the presence of sulfides in 100Cr6 steel [13]. Zhang summarized that the alumina inclusions in low carbon Al-killed steel and silica inclusions in Si-killed steel generated by the reaction between the dissolved oxygen and the added aluminum and silicon deoxidants are typical deoxidation inclusions. Exogenous inclusions arise primarily from the incidental chemical and mechanical interaction of liquid steel with its surroundings, and act as heterogeneous nucleation sites for precipitation of new inclusions during their motion in molten steel [5].

Several sources could be the origin of inclusions. Deoxidation products formed by added deoxidents (Al and Si) and dissolved oxygen, refractory and ceramic lining erosion of the ladle and metal delivery system, re-oxidation in the mold from air entrainment and oxides in slag phase, endogenous inclusions formed in solidification, and exogenous

inclusions originated from mold flux entrainment are major sources [5]. In many studies, aluminates were considered to originate from deoxidation and large multiphase inclusions are formed by entrained mold flux [3]. Alumina inclusions readily form three-dimensional clusters via collision and aggregation due to their high interfacial energy. Silica inclusions are generally spherical, owing to their liquid or glassy state in molten steel. Sulfides form inter-dendritically during solidification and often nucleate on oxides already present in the liquid steel [5].

Air is the main source of re-oxidation. Strong turbulence will mix the molten steel with air during teeming in the ingot or at the connection of ladle and trumpet. Air also can transport from the surface of steel to the body of the liquid steel in the ingot [5]. The exposure of molten steel to the atmosphere will rapidly form oxide films on the surface of the flowing liquid, which are folded into the liquid, forming weak planes of oxide particles in the solidified product [5]. Deoxidizing elements such as Al, Ca, and Si are preferentially oxidized by environmental oxygen, and their re-oxidation products develop into nonmetallic inclusions. Methods used to protect the teeming stream in ingot casting can be classified as shrouding by an inert gas curtain injected, purging inert gas into the runner system and mold before teeming, and using a vacuum environment. Another reoxidation source is SiO_2, FeO, and MnO in the slag and lining refractory [5].

Mold flux is used to prevent the dissolution of oxygen transporting into the steel from the top surface, and as a heat isolator in order to prevent freezing [4]. During the process of casting, strong turbulence of the molten steel would result in the entrainment of mold powder. Steelmaking operations including mixing of mold flux and steel produce liquid particles suspended in the steel [5]. Many liquid particles can coalesce and be removed by transport and floatation to the top surface and absorption into the slag. However, those which remain can nucleate further inclusions and interact chemically with refractories, giving rise to complex inclusions. Mold flux entrainment in the mold is affected mainly by the following: vortexing, method of powder addition, runner and upgate design, filling rate, turbulence at the meniscus, and slag properties [4].

During the initial entry when molten steel flows into the bottom of the mold especially with a high filling rate, the momentum of the inflow can rise upward into the ingot to form a disturbance on the free surface of the molten steel and entrain the mold

powder [5]. With the filling process continues the disturbance will disappear and the molten steel may push the floating mold powder to the sides. Excessive turbulence at the slag metal interface is one of the causes of reoxidation and exogenous inclusions. Zhang states that the effect of the shape of the runner outlet (mold upgate) on the molten steel flow pattern in the mold was examined using a water model and numerical simulation [4]. Moreover, he concluded that in order to avoid turbulence flow with high velocity, the ratio of the linear length of the upgate to its minimum diameter should be larger than 6. The direction and velocity of the inlet jet depends on the details of the upgate geometry. The recent computational results illustrate the great importance of upgate shape on the direction of the spout [3]. The calculation of the fluid flow and inclusion trajectory in the runner indicates that inclusions tend to move along the top wall, so they might be trapped by weirs or inclusion-entrapment cavities near the end of runners. Using ceramic foam filters at the runner system near the upgate is another method to remove more inclusions before they enter the ingot mold [5].

Erosion of refractories is a very common source of large exogenous inclusions, which are typically solid and based on the materials of the trumpet, runner, and mold themselves. It was reported that almost all of the inclusions in a tool steel ingot originated as oxides from the erosion of the ladle glaze, and the amount of inclusions increased with ladle age [6]. Lining erosion generally occurs at areas of turbulent flow, especially when combined with reoxidation, high pouring temperatures, and chemical reactions.

In the review work of controlling inclusions in ingot casting, Zhang et al stated that optimizing the runner shape, ingate geometry design, teeming rate and suspended height of the powder bags were effective on steel cleanliness improvement [3]. Zhang also studied large inclusions ($>20\mu m$) in plain carbon bottom-poured steel ingots and found that 59% consist of alumina clusters and lumps which could be originating from entrained mold flux and 31% were from eroded refractory [5]. Eriksson also states that a new type of inclusion containing mostly alumina has been detected during mold filling in the upper part of the ingots [15]. The erosion of the inner as well as outer nozzles and the slide gates has been found to be responsible for the presence of these alumina-based inclusions. The examination of steel samples from ingots has shown that inclusions distribute unevenly in the solidified ingot [15]. The inclusion populations have been

found to be the highest in the central part of the ingot. Also, the inclusion populations in steel samples from the final product are higher than in the steel before casting. The number of heats on a ladle has also been linked to the number of inclusions in the final products. The inclusions generated by the ladle glaze affect the quality of the final product [15].

1.3. MATHEMATICAL MODELING IN INGOT CASTING

Inclusion formation in ingot casting is strongly affected by the flow pattern of molten steel in the process of uphill teeming, as shown in Figure 1.2. The liquid steel will enter the mold with high velocity through the runner and entrance nozzle. With increasingly more stringent requirements on steel quality and productivity in uphill teeming production, it is vital to attain more desirable fluid flow conditions in the filling of the mold.
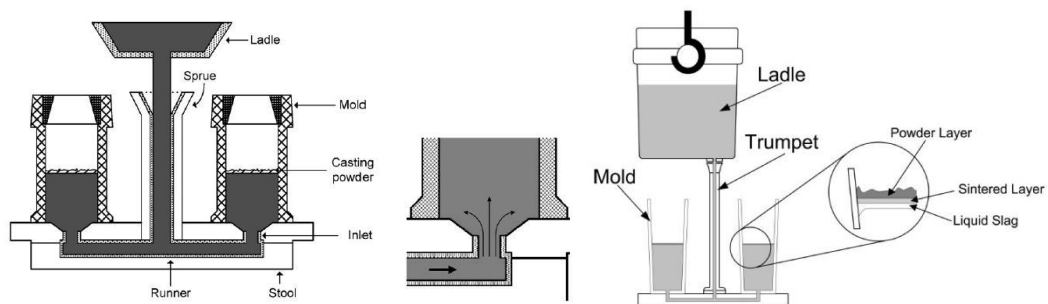
Figure 1.2 Two Schematic Descriptions of the Uphilling Teeming Process [15, 17]

Eriksson established the fundamental mathematical modeling of the filling of the ingot, predicted fluid flow characteristics and studied the effect of a modified inlet allowing a large volume flow [15]. Results indicated that a successive increase in the

opening angle of the inlet nozzle leads to a gradual decrease in the disturbance of the free surface during mold filling as shown in Figure 1.3.

(a) Straight inlet

(b) 10° inlet

(c) 20° inlet

(d) 30° inlet
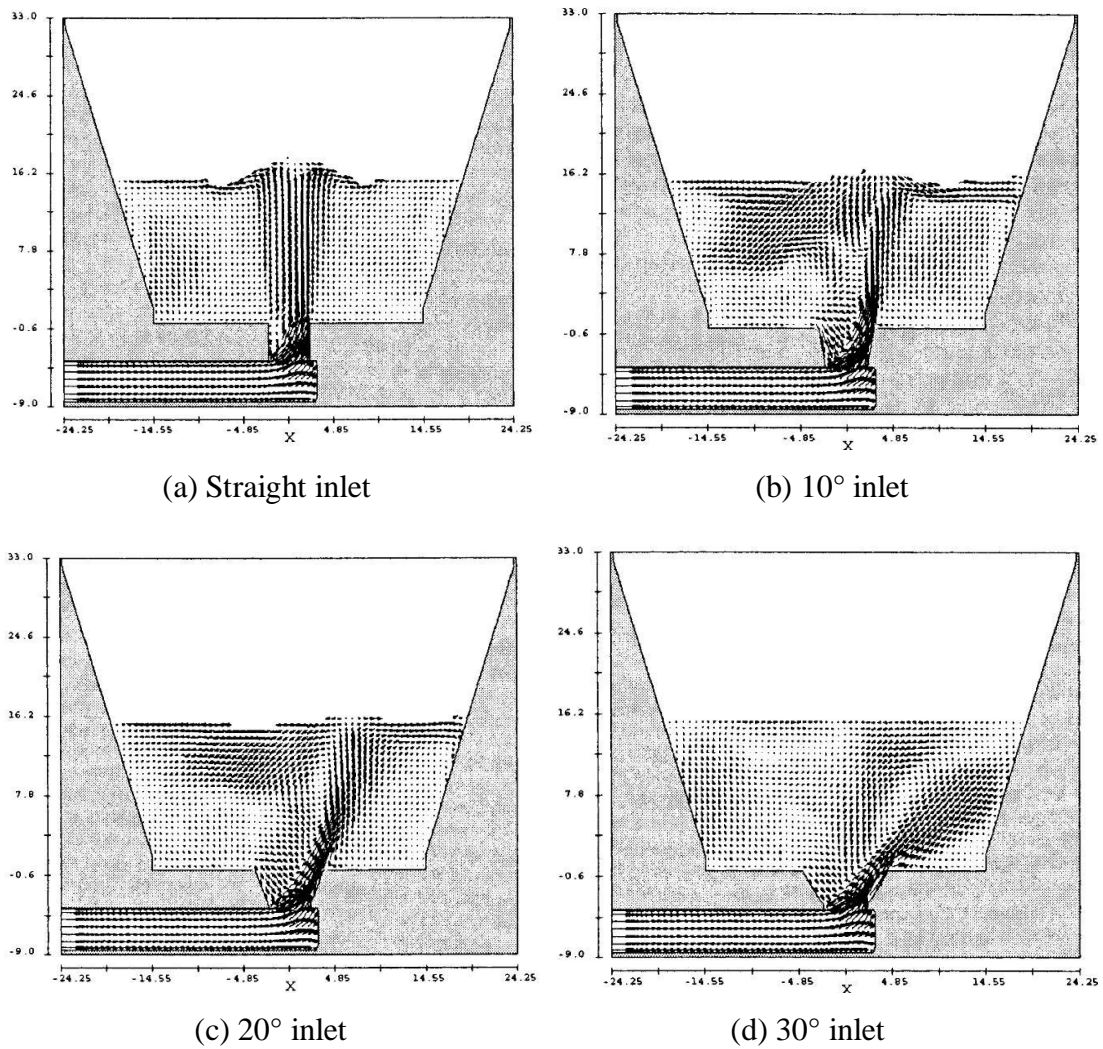
Figure 1.3 Velocity Vector after 14.75s of Filling at Cross Section Plane for Inlet Configuration: (a), straight, (b), 10°, (c), 20°, (d), 30° [15].

The horizontal velocities are lower, resulting in lower values of the Weber number which decreases the chances for mold flux entrainment into the steel. The Weber number could be calculated as follow:

$$We = \frac{u_{steel}^2 \rho_{steel}}{\sqrt{\gamma g (\rho_{steel} - \rho_{slag})}} \tag{1}$$

Where u_{steel} is the velocity of the steel in the x-direction relative to the mold flux, ρ_{steel} and ρ_{slag} are the densities of the steel and mold flux respectively, g is the gravitational constant and γ is the interfacial tension between the steel and mold flux. If the horizontal velocities in the x-direction are only up to 10cm/s, the Weber number cannot be larger than 12.3, which was found to be the critical number for mold flux to disperse into the steel phase, even if the interfacial tension between the steel and mold flux phase is as small as 0.1N/m for plant conditions in which that oxygen is transferred through the slag/steel interface by the reaction between FeO in the mold flux and Al dissolved in the steel [15].

Eriksson concluded that the best results were obtained using an inlet nozzle at a 25 degree angle. For this case, the steel rising surface was almost flat and the horizontal velocities were kept below 10cm/s. In general, the surface deformation decreases with increased inlet nozzle angle. The incoming flow is moved closer to the right side of the mold when the inlet nozzle angle is increased.

A two-dimensional non-steady state computational fluid dynamic model was employed by L. Ragnarsson to gain a basic understanding of the flow pattern in ingot casting [16]. The surface velocity was also found to be affected by the inlet angle and vary with the casting level. Experiments in a 1:3 scale water model of a bottom-poured 5.8 t industrial ingot revealed the same types of trends as the results from numerical simulation (Figure 1.4). The results showed that the existing inlet angle of 5 degrees used in industry was the best option for removal of inclusions originating from the mold flux. Two major factors that affected removal were the distance of the inclusions from the slag and the ratio of this distance to the casting level. It is desirable to find a way to form an

absorbing liquid film as early as possible in order to remove inclusions generated from mold flux in the early stage of casting.
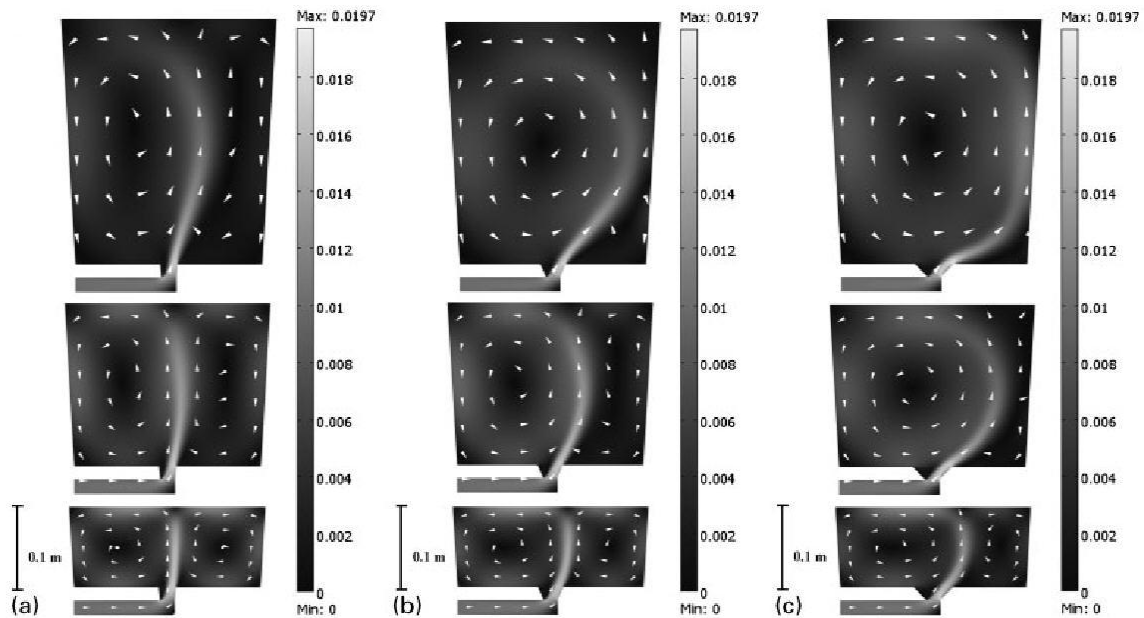
Figure 1.4 Velocity Vector of Flow in Water Mold at Different Casting level: (a) Inlet Angle 5°, (b) Inlet Angle 25°, (c) Inlet Angle 45° [16]

L. Hallgren used physical and mathematical modeling to study the effects of nozzle type and utilization of a swirl generator in the inlet nozzle on the flow pattern in the ingot mold during the initial filling period [17]. Special emphasis was placed on determining the factors that influence the resultant hump and axial velocities. Cases with a straight nozzle, a divergent nozzle, and a divergent nozzle combined with a swirl generator were simulated and compared. It was found that the combined divergent nozzle and swirl generator resulted in the smallest hump and lowest axial velocities in the bath, as well as lowest turbulence at the meniscus (Figure 1.5). In view of industrial applications, a smaller hump and lower axial velocities during the initial filling of the

mold are very positive attributes since they entail less entrainment of mold flux. Furthermore, the lowered extent of interaction with the mold powder can lead to a reduction in mold powder consumption. The maximum hump height for the case of a divergent nozzle with swirl was only about 30% of the height with straight nozzle and 40% of the height with a divergent nozzle without swirl. Comparing to the other cases, the kinetic energy of the turbulence was very low at the surface for the divergent nozzle with swirl combination. The axial velocity at the center position for the straight nozzle without swirl was nine times greater in comparison to the divergent nozzle with swirl.
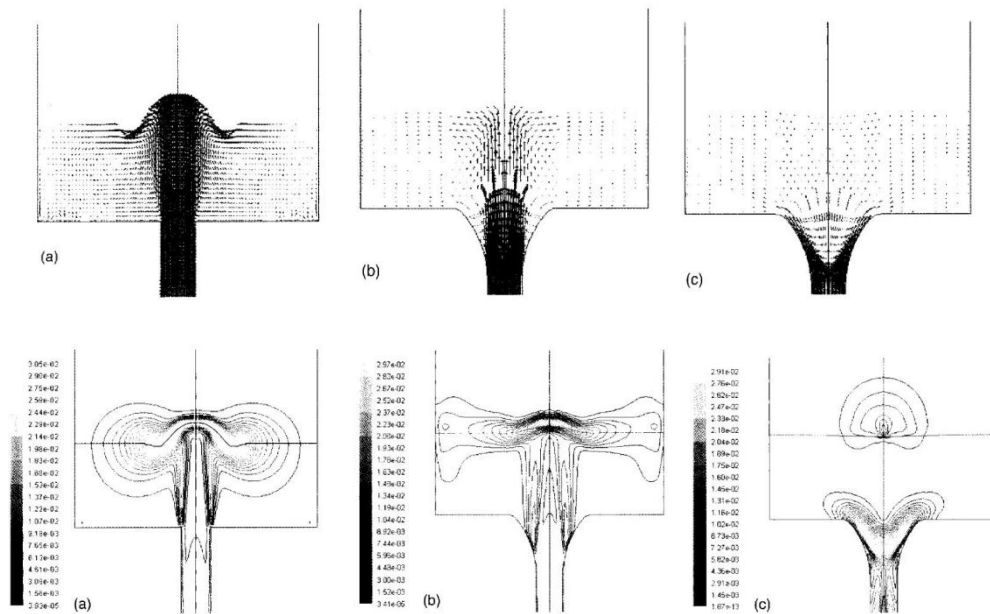
Figure 1.5 Velocity Vectors in Water Mold and Contours of Turbulent Energy for Simulation Using: (a) Straight Nozzle, (b) Divergent Nozzle, (c) Divergent Nozzle with Swirl (Swirl Velocity = 0.43m/s) [17]

Zhang and Yokoya did similar work in a numerical study of swirl blade effects during uphill teeming [18]. In their study, a twist-blade was applied in a mathematical model to create a swirl flow in the inlet of the mold. The swirl blade was set vertically

just beneath the inlet, which was made of a gradually divergent cross-sectional area. The results showed that combinations of the inlet swirl flow and molds with gradually divergent nozzles contributed to the formation of very uniform velocity distributions within only six seconds after the molten steel entered the mold with no formation of a hump on the free surface during all filling times (Figure 1.6). These phenomena will ensure that the mold flux is spread onto the surface of liquid steel evenly. Besides, the stable surface also prevents the mold flux from being dispersed into the steel.
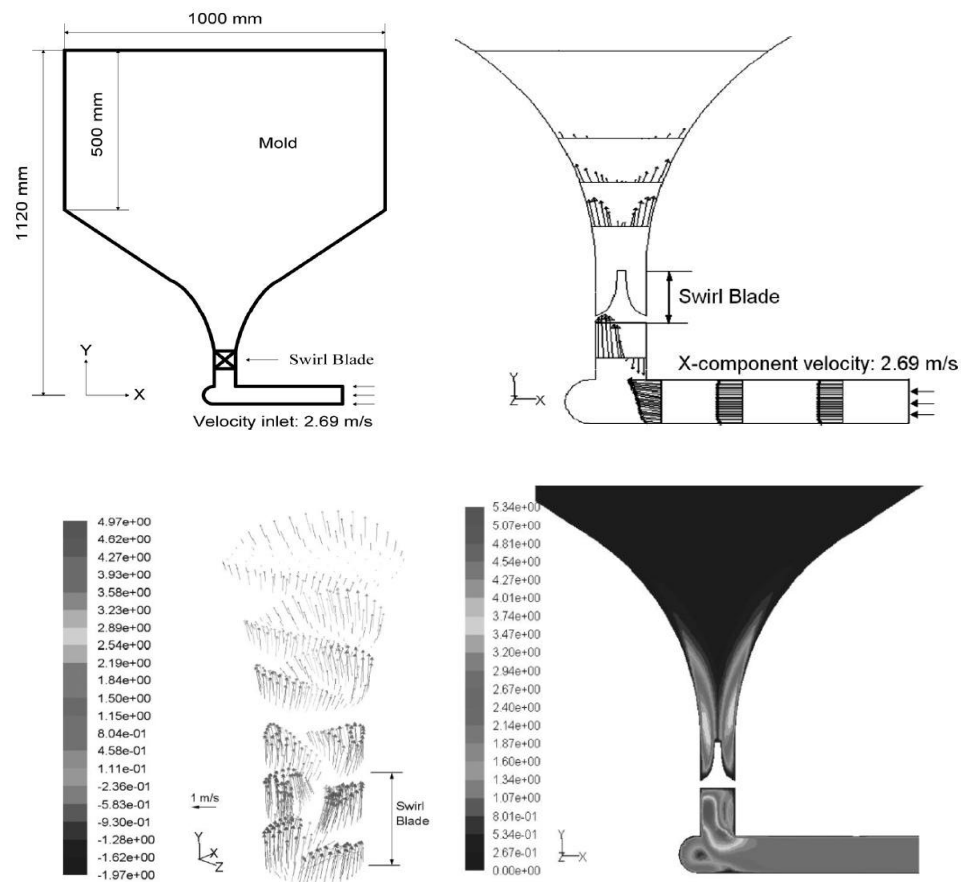
Figure 1.6 Geometry of Mold, Vector and Contours of Velocity Magnitude at Inlet with Large Angle Upgate and Swirl Blade [18]

Hallgren and his colleagues used mathematical and physical modeling to study the effects of a swirl blade in the entry nozzle of ingot casting and found that the maximum velocity of fluid flow decreased and the minimum velocity increased, in other words, the velocity unevenness was reduced due to the modified flow pattern (Figure 1.7) [19].
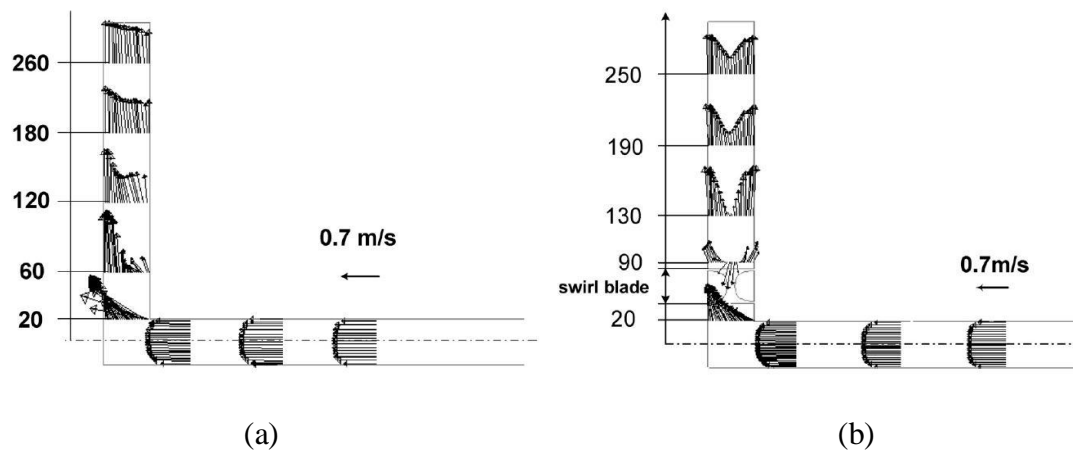
Figure 1.7 Velocity Vector of Liquid Steel in Runner and Nozzle: (a) Traditional, (b) Equipped with Swirl Blade [19]

1.4. SUMMARY

In order to satisfy the increasing demand of specialty steels with high strength and long fatigue life, researchers have devoted efforts to improving steel cleanliness. Inclusions have a strong relationship with mechanical properties of steel; therefore, inclusion control is critical to control the quality of steel production. Different steel cleanliness standards have been established for different steel grades. The teeming process of ingot casting, as the primary process of specialty steel production, has been investigated by both 2-dimensional and 3-dimensional fluid flow numerical simulations. Through modifying the upgate with an inlet angle and adding a swirl blade, the flow pattern of the molten steel is re-structured to result in a hump with smaller size, less

turbulence, and more even velocity distribution. This will benefit cleanliness by reducing mold flux entrainment, re-oxidation by air entrainment, and refractory erosion in the mold. However, due to the complexity and infeasibility of adding a swirl blade, it is better to generate the swirl flow solely by design of upgate system with a modified geometry.

Previous research has not included a systematic comparison between industrial trials and numerical simulation on the effect of swirl modified ingot casting. The purpose of this thesis is to investigate the effects of several different designed upgate systems on the resulting fluid flow of molten steel interacted with mold flux and the formation of inclusions. Moreover, the morphology, composition and distribution of inclusions were investigated by different analysis methods from industrial trials with different upgate systems.

2. EXPERIMENTAL AND MODELING PROCEDURE

2.1. INTRODUCTION AND OBJECTIVES

In order to investigate the effect of swirl-modified upgates in ingot casting, four CFD simulation cases with different upgate systems including one traditional upgate as the control experiment, one 50% open upgate system, one 75% open upgate system, and one large pan-like designed upgate system were studied in this research using the software ANSYS FLUENT. These swirl-generating designs were intended to form a swirl flow in the upgate system, by which the turbulent energy of the flow can be reduced when it entered the ingot and therefore the disturbance of free surface in the ingot generated by the upward flow of liquid steel can be smaller. Fluid flow pattern in the whole ingot, turbulent kinetic energy at the cross sections, velocity magnitudes and vectors of steel phase were examined for verification and comparisons.

Industrial experiments were conducted in a steel company in which two ingots (one control set and one with 50% open upgate) were bottom teemed. Steel samples located at different heights and radial positions were analyzed to obtain the amount, size distribution, morphology and composition of inclusions.

The main purpose of this thesis is to understand the relationship between the geometry of the new designs of upgate systems and their effects on the flow pattern, inclusion formation and distribution in ingot casting. Numerical simulation, optical microscopy, scanning electron microscopy, and ASPEX inclusion analysis are applied in this work to understand these relationships. The mechanism of inclusion formation is studied using the results from observation and calculation.

2.2. INDUSTRIAL TRIAL

In the industrial trial, 316L stainless steel was cast by the bottom-teeming ingot process. Figure 2.1 shows the runner and swirl-modified upgate system, as well as the bottom of the ingot. The runner is square shaped with a 5.08 cm (2 inches) side length. The ingot has a square shape bottom with side length of 71.12 cm (28 inches) and a cast weight of approximately 71667.6 kg (158000 lbs). The traditional upgate system is in the

shape of cylinder. The swirl-design upgate is in this same shape but with a diagonal-cut at the end of the runner (Figure 2.1). Red shape in the figure is the cut part of the runner.

Table 2.1 illustrates the initial composition of the 316L stainless steel, which is detected by an industrial spectrometer. Four molds were set in one cluster and one mold employed the modified upgate system. Table 2.2 provides the composition of the mold flux added during casting in this trial, which is described by the flux supplier. Table 2.3 lists the main casting parameters including teeming temperature, superheat, and the amount of flux.
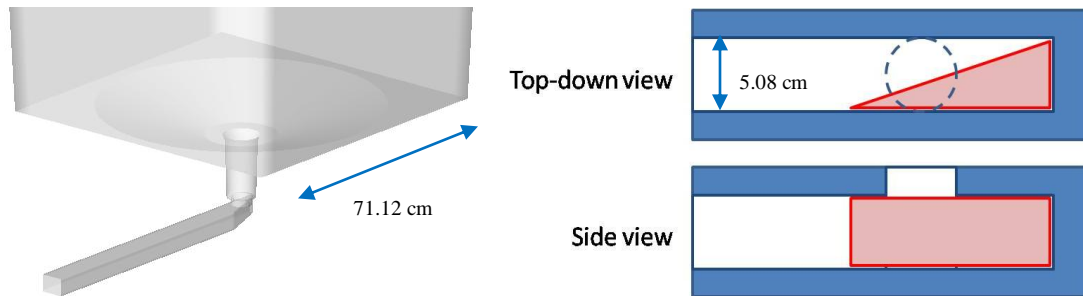
Figure 2.1 Geometry of the Swirl Upgate in Industrial Trial (Red: Cut Part)

Table 2.1 Composition of 316L Stainless Steel in Mass %

%C	%Si	%Mn	%S	%P	%Cr	%Ni	%Mo	%Al	%N
0.02	0.43	1.50	0.004	0.022	16.31	10.28	2.10	0.002	0.064

Table 2.2 Composition of Flux Used in the Mold in Mass %

Al_2O_3	SiO_2	CaO	Fe_2O_3	Na_2O	K_2O	MgO	TiO_2	MnO	F	C
6.9	40.5	31.4	1.8	4.6	1.2	0.8	0.2	0.1	5.3	3.8

Table 2.3 Main Casting Parameters in the Industrial Trial (From Industry)

Parameter	Value	Parameter	Value
Density of steel	0.29 lbs/in^3	Super heat	150°F
Liquidus temperature	2644 ^{o}F	Solidus temperature	2410 ^{o}F
Teeming temperature	2794 ^{o}F	Teeming rate	6626in^3/min
Amount of flux	5.6lbs/t	weight of ingot	15800lbs

2.3. INCLUSION ANALYSIS

In order to provide a comprehensive and quantitative analysis, different observation evaluation methods were adopted in inclusion analysis.

2.3.1. Sample Preparation. The square ingots from the industrial experiments were hot forged into a round product. Steel blocks were then cut at different locations, with both different heights and different radial distances (see Figure 2.2 and 2.3). Samples of 76C and 77C were taken from the swirl-modified ingot. Samples of 75C were taken from the traditional ingot. This is to have a systematic investigation on how inclusion formation was affected by the fluid flow.
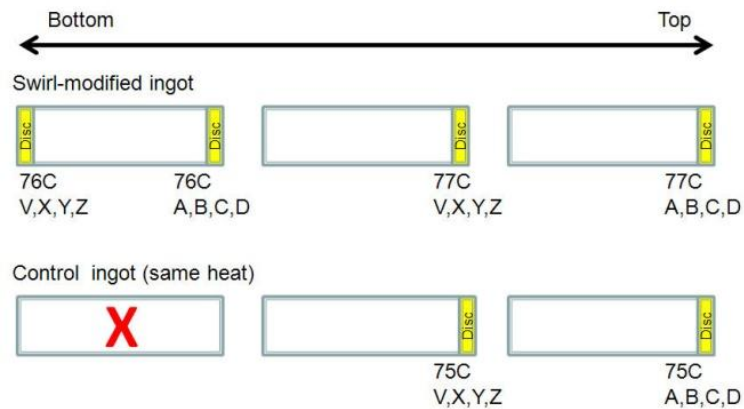
Figure 2.2   Locations of Samples on the Ingot in Horizontal View

The steel samples were cut into 20 mm × 20 mm × 20 mm cubes using a BUEHLER® Delta® manual abrasive cutter. These samples were then hot mounted with a BUEHLER® SimplyMet® 1000 Automatic Mounting Press with black phenolic powder. After mounting, the samples were first ground manually with sandpaper in the sequence of 120, 240, 400, 600, 800, 1000 grit, then polished with a BUEHLER® EcoMet® 250 grinder and polisher with SiC, diamond polishing material in the sequence of 9μm, 3μm, 0.05μm. Inclusions in the steel samples were then analyzed.
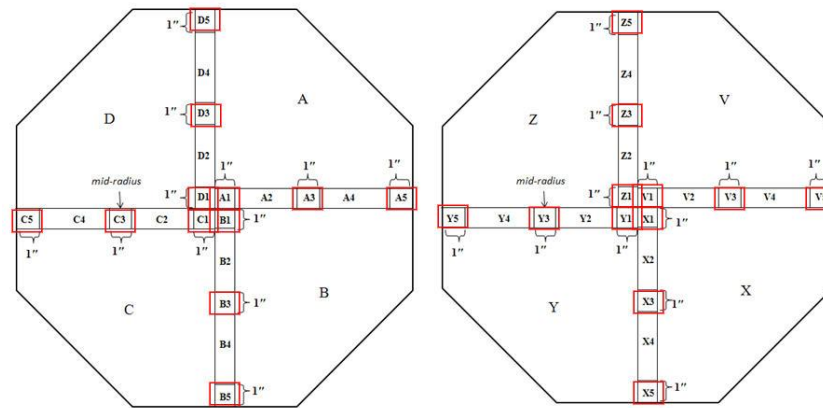
Figure 2.3   Locations of Samples on the Cross Section of the Ingot

2.3.2 Optical Microscopy. Morphology and size distribution of inclusions in the steel samples were analyzed using an optical microscope (Nikon® EPIPHOT® 200). When the samples were observed under the optical scope, an eye lens with 10 times magnification and objective lens with 50 times magnification were adopted. A total of 300 unrepeated fields of views were checked, which is 48 mm^2. The number of inclusions was counted and photos of each inclusion were captured. The data compiled was processed using Microsoft Office®, Photoshop® and Origin® software.

The area ratio of inclusions for one sample was calculated with:

$$A = \frac{\sum\left(d_i^2 \times 10^{-6}\right)}{D^2 \times N} \times 100\% \tag{1}$$

Where d_i is the inclusion diameter in μm, D is the diameter of each view (0.4 mm), N is the number of total views (300).

Parameter A indicates that the proportion of actual area of inclusions over the total area, 48 mm^2 of 300 unrepeated views from each steel sample.

Also, the average diameter of the inclusions for one sample was calculated with:

$$D_{avg} = \left[\frac{\sum\left(d_i^2 \times 10^{-6}\right)}{n}\right]^{\frac{1}{2}} \tag{2}$$

Where n is the total number of inclusion in this sample. Parameter D_{avg} indicates the average inclusion size in one single sample.

2.3.3. SEM Observation. An SEM (Hitachi® S4700®) with EDS detector was used to examine samples including 76C_B1, B3, B5, 75C_B3, X3, 77C_B3, X3, Z3. Data of atomic percentage and weight percentage of elements from EDS were processed. The weight percentage of oxide and sulfide was then calculated.

In the process of oxide and sulfide calculation, the equation below was adopted:

$$X_{wt\%\, oxide-M} = \frac{X_{at\%\, element-M} \times \dfrac{M + O \times \dfrac{y}{x}}{M}}{\sum X_{at\%\, element-M} \times \dfrac{M + O \times \dfrac{y}{x}}{M}} \times 100\% \tag{3}$$

Here M_xO_y is assumed to be the form of the oxide of element M. M and O are atomic weight of element M and oxygen. This assumption is similarly applied to sulfide inclusions.

To simply the calculation of oxide and sulfide content, it was assumed that sulfur reacts with manganese and then calcium. If there was sulfur remaining after reacting the [S] with [Mn] and [Ca], then the remaining sulfur content was assumed to be [S] alone. All the other elements were assumed to be an oxide.

2.3.4. ASPEX Inclusion Analysis. ASPEX is an industrialized automated scanning electron microscope integrated with algorithms for routine production monitoring and control. It automatically scans the surface of the steel sample detecting the amount, size distribution and composition of inclusions. Using ASPEX, a large number of inclusions on a two-dimensional surface of a steel sample can be analyzed in a short time.

All 72 samples were processed using the ASPEX inclusion analyzer. For each samples, 4 areas of 5~10mm^2 were randomly selected and searched for inclusions. Two rule files were used for inclusion classification (see Table 2.4 and 2.5). One is for the purpose of detecting sulfide, oxide and oxide-sulfide; the other one is designed for typical types of inclusion including MnS, Al$_2$O$_3$, Al-Ca, Al-Mn, Al-Si, SiO$_2$, CaO, MnO.

Table 2.4 Specifics of Rule File 2 and Vector File

Classification	Rules
Vector File	C, N, O, Al, Si, S, Ca, Ti, Cr, Mn, Fe, Ni and Mo
MnS	Mn >= 30 & S >= 20 & Ca < 20
CaS	Ca >= 30 and S >= 20 and Mn < 20
Mn-Ca-S	Mn >= 15 and Ca >= 15 & S >= 20
Other Sulfides	S>=20
High Al$_2$O$_3$	Al>=20 &Mn<20 & Ca<20 & Si<20 & Mg<10 & Ti<10
High MgO	Mg>=10 & Al<10 & Mn<20 & Ca<20 & Si<20 & Ti<10
High CaO	Ca>=20 & Al<10 & Si<20 & Mn<20 & Mg<10 & Ti<10
High SiO$_2$	Si>=20 & Mn<20 & Al<10 & Ca<20 & Mg<10 & Ti<10
High TiO$_2$	Ti>=20 & Al<10 & Ca<20 & Si<20 & Mn<20 & Mg<10
High MnO	Mn>=20 & Al<10 & Si<20 & Ca<20 & Ti<10 & Mg<10
Al-Ca-O	Ca>=20 & Al>=10 & Si<20 & Mn<20 & Mg<10 & Ti<10
Al-Mn-O	Mn>=20 & Al>=10 & Si<20 & Ca<20 & Mg<10 & Ti<10
Al-Mg-O	Mg>=10 & Al>=10 & Mn<20 & Si<20 & Ca<20 & Ti<10
Mn-Si-O	Mn>=20 & Si>=20 & Al<10 & Ca<20 & Mg<10 & Ti<10
Al-Si-O	Al>=10 & Si>=20 & Mn<20 & Ca<20 & Mg<10 & Ti<10
Al-Ti-O	Al>=10 & Ti>=10 & Mn<20 & Ca<20 & Mg<10 & Si<20
Ca-Si-O	Ca>=20 & Si>=20 & Al<10 & Mg<10 & Mn<20 & Ti<10
Ca-Mn-O	Ca>=20 & Mn>=20 & Al<10 & Mg<10 & Si<20 & Ti<10
Zero Elements	
Fe=0	If Al>=2.5 or Mn>=2.5 or Ca>=2.5 or C>=2.5 or Si>=2.5
O=0, C=0	If Al>=2.5 or Mn>=2.5 or Ca>=2.5 or Si>=2.5
Cr=0	If Cr<25

Table 2.5 Specifics of Rule File 1 and Vector File

Classification	Rules
Vector File	C, Na, Mg, Al, Si, S, K, Ca, Ti, Cr, Mn, Fe, Ni and Mo
FeO Stain Micro Defects Carbon Defects Sulfides Sulfides-Oxides Oxides	Fe>=30 (Fe + Cr + Ni + Mo)>=90 C>20 S>=30 and (Mn+Ca)>=50 and (Mg+Al+Si+Ti+Cr+Ni)<=10 S>=5 and (Mn+Ca)>=5 and (Mg+Al+Si+Ti+Cr+Ni)>=5 True
Zero Elements	
Cr=0 Ni=0 Fe=0 C=0	If Cr<20 If Ni<15 If Al>=2.5 or Mn>=2.5 or Ca>=2.5 or C>=2.5 or Si>=2.5 If Al>=2.5 or Mn>=2.5 or Ca>=2.5 or Si>=2.5

2.4. CFD MODELING

In order to simply and shorten the computational time, the geometry of the ingot mold was created similarly with the actual industrial mold but with only 25% of its height in GAMBIT version 2.4.6. The model was then then set up in FLUENT with version 6.3.26.

2.4.1. Geometry. Using results from earlier research summarized in the introduction as a basis, a series of new ingot geometries were designed with large inlet angles and a swirl generating upgate system (see Figure 2.4). The large inlet angle was designed to diminish the presence of the hump. The 50% open upgate, ¾ open upgate and whirlgate systems were designed to form a swirl flow in the ingot mold to even out the velocity distribution and decrease the turbulence in the mold.

An 863.6 mm height and 787.4 mm diameter cylinder ingot mold was used in this study which is different from the ingot shape in the industrial trial. The four cases that were modeled all have a common ingot and runner geometry but different upgate systems. Case 1 was not equipped with a special designed upgate but represents the original one used in industry and was set to be the control experiment. In Case 2, the connection between runner and upgate was cut in vertical direction to be half open at the cross section so as to generate a swirling flow. Case 3 was not cut vertically at the position of ½ diameter in horizontal direction but at location of ¾ lengths on the diameter

on the cross section. Case 4 has one large pan-like cylindrical tank at the connection in place of the cylindrical upgate and is similar to whirlgates used in the foundry industry. All these simulations have a 50 mm diameter round pipe runner as inlet with a length of 420 mm.
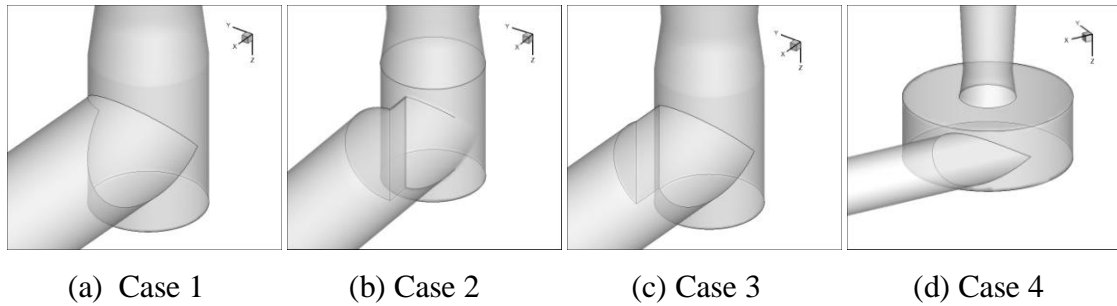

| (a) Case 1 | (b) Case 2 | (c) Case 3 | (d) Case 4 |

Figure 2.4 Geometry of (a) Traditional Upgate, (b) 50% Open Upgate, (c) 75% Open upgate, (d) Whirlgate

2.4.2. Mathematical Model. In this study, typical three dimensional fluid flow models were established to solve the continuity equation and Reynolds-averaged Navier-Stokes equations for the incompressible Newtonian fluid. Volume of Fraction (VOF) model is typically used to simulate the process of ingot filling. When two or more immiscible fluids (in this study were air and liquid steel) are used by solving a single set of momentum equations and tracking the volume fraction of each of the fluids throughout the domain, the VOF model can be applied.

Furthermore, all the calculations carried out in this study were based on the assumptions made as follow:

All immiscible fluid phases (air, liquid steel and slag) present in a control volume share the same velocity, pressure and temperature fields;

The molten steel is incompressible Newtonian fluids for simplicity;

Heat transfer during filling is ignored;

It is assumed that no chemical reactions take place;

The flow rate of molten steel at the inlet is constant.

The governing equations representing the mathematical model are as follows.

Equation of continuity

$$\frac{\partial \rho}{\partial t} + \frac{\partial (\rho u_i)}{\partial x_i} = 0 \qquad [1]$$

Navier-Stokes equations

$$\frac{\partial (\rho u_i)}{\partial t} + \frac{\partial (\rho u_i u_j)}{\partial x_j} = -\frac{\partial P}{\partial x_i} + \frac{\partial}{\partial x_j}\left[\mu_{eff}\left(\frac{\partial u_i}{\partial x_j} + \frac{\partial u_j}{\partial x_i}\right)\right] + \rho_i g + F_j \qquad [2]$$

Turbulent kinetic energy and its dissipation rate (k-ε equations)

$$\frac{\partial (\rho k)}{\partial t} + \frac{\partial}{\partial x_i}\left(\rho u_i k - \frac{\mu_{eff}}{\sigma_k}\frac{\partial k}{\partial x_i}\right) = \mu_t \frac{\partial u_j}{\partial x_i}\left(\frac{\partial u_i}{\partial x_j} + \frac{\partial u_j}{\partial x_i}\right) - \rho\varepsilon \qquad [3]$$

$$\frac{\partial (\rho\varepsilon)}{\partial t} + \frac{\partial}{\partial x_i}\left(\rho u_i \varepsilon - \frac{\mu_{eff}}{\sigma_\varepsilon}\frac{\partial\varepsilon}{\partial x_i}\right) = C_1 \mu_t \frac{\varepsilon}{k}\frac{\partial u_j}{\partial x_i}\left(\frac{\partial u_i}{\partial x_j} + \frac{\partial u_j}{\partial x_i}\right) - C_2 \frac{\varepsilon}{k}\rho\varepsilon \qquad [4]$$

With the k-ε equations, the turbulent viscosity is given by [5]

$$\mu_t = \rho C_\mu \frac{k^2}{\varepsilon} \qquad [5]$$

Thermal energy conservation,

$$\frac{\partial (\rho T)}{\partial t} + \frac{\partial (\rho u_i T)}{\partial x_i} = \frac{\partial}{\partial x_i}\left(\rho k_{eff}\frac{\partial T}{\partial x_i}\right) \qquad [6]$$

For the ith phase,

$$\frac{1}{\rho_i}\left[\frac{\partial}{\partial t}(\alpha_i \rho_i) + \nabla \cdot (\alpha_i \rho_i u_i) = S_{\alpha_i} + \sum_{j=1}^{n}(x_{ji} - x_{ij})\right] \qquad [7]$$

$$\sum_{i=1}^{n}\alpha_i = 1 \qquad [8]$$

Where S_{α_i} is the source or sink of the ith phase, x_{ji} is the mass transfer from phase j to phase i.

For solution control, PISO (Pressure-Implicit with Splitting of Operators) method was applied for pressure-velocity coupling. The body force weighted method was used to solve for the pressure. First order upwind discretization schemes were adopted for calculation of momentum, turbulent kinetic energy and dissipation rate. Moreover, a geo-

reconstruct spatial discretization method was chosen for the volume fraction. All the relaxation factors were set to be 0.4.

2.4.3. **Parameters and Dimensions.** Dimensions and parameters of the ingot mold are listed in Table 2.6 and all the boundary conditions are shown in Table 2.7. During an iteration, convergence is assumed to be reached if all the normalized un-scaled residuals are smaller than 0.001. It is assumed that the top of the ingot mold is the pressure outlet with zero shear stress.

Table 2.6 Main Dimensions and Parameters in Simulation

Parameter	Value	Parameter	Value
Mold height	863.6 mm	Diameter of Mold	787.4 mm
Upgate height of Mold	225.425 mm	Diameter of Mold Bottom	558.8 mm
Diameter of Runner	50 mm	Ingot teeming rate	0.3905 ton/min
Density of liquid steel	7020 kg/m^3	Viscosity of liquid steel	0.0067 kg/m·s
Surface tension	1.89 N/m	Courant number (initial)	0.25

Table 2.7 Boundary Conditions in Simulation

Parameter	Value	Parameter	Value
Inlet speed at runner	0.457676 m/s	Inlet turbulent energy	0.0012824 m^2/s^2
The top of ingot	Pressure outlet	Turbulent dissipation rate	0.008907 m^2/s^3
Stationary walls	No slip		

2.4.4. **Mesh.** All the geometries and meshes were built in GAMBIT, which were then imported into FLUENT. Figure 2.5 illustrates the mesh design for the runner and ingot system in these four cases. In Figure 2.6, the meshing of the different upgate systems equipped in these four cases are shown. Table 2.8 gives a summary of the mesh quality of these four cases. The mesh designs of the upgate for the four cases used

different mesh methods to generate constructional and non-constructional elements (see Figure 2.6).
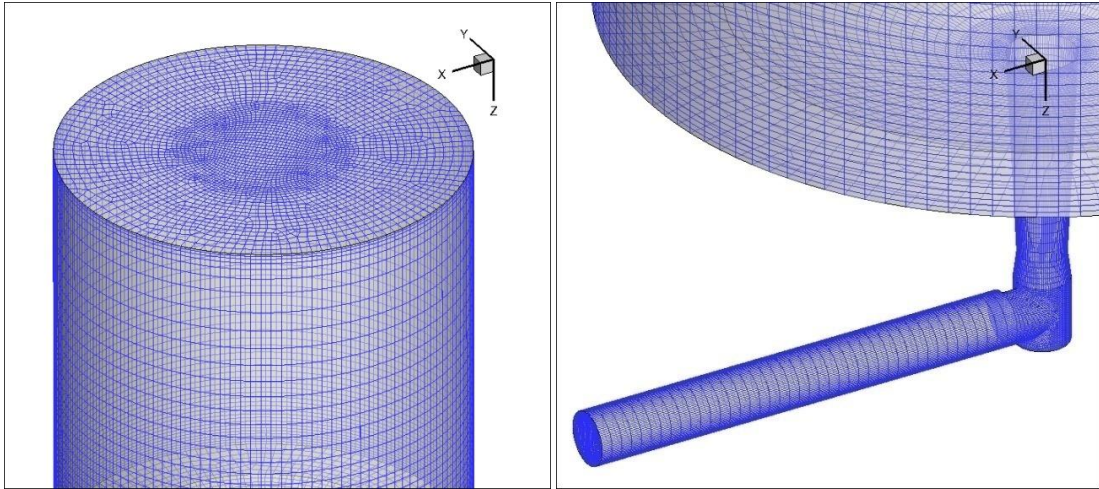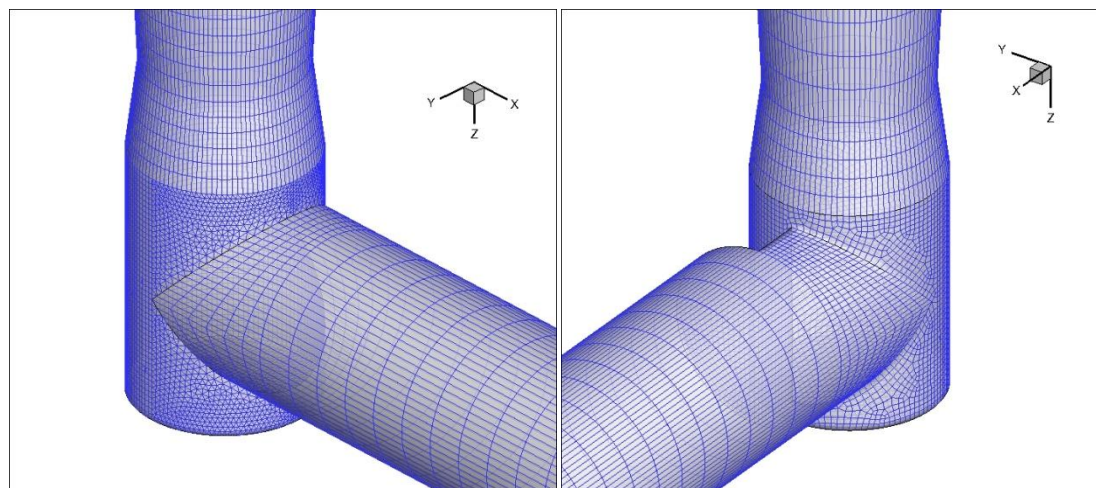

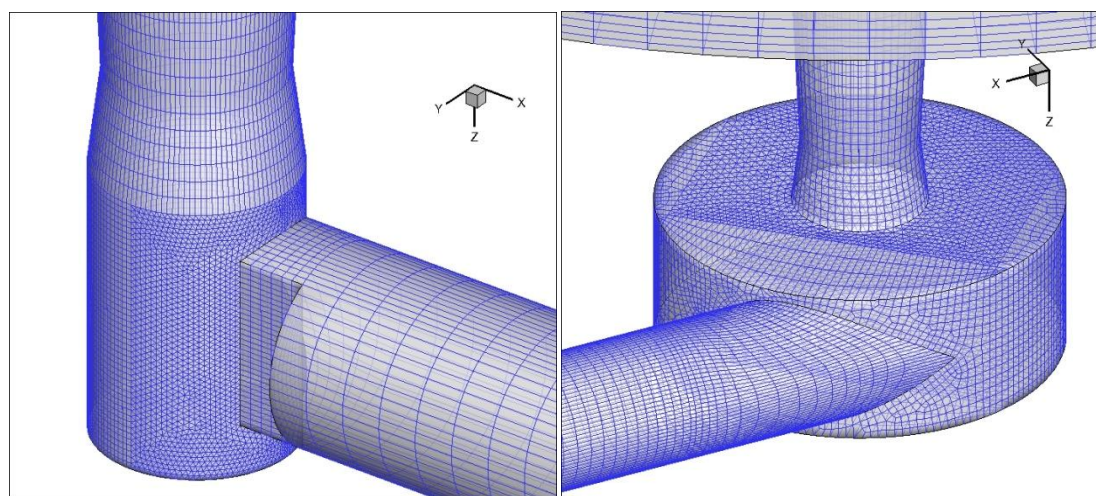Figure 2.5 General Mesh Design of the Ingot and Runner System in the Four Cases

Table 2.8 Overview of Mesh Quality for the Four Cases

	Total cells	Maximum cell skewness	Maximum aspect ratio
Case 1	475595	0.9936	41.82
Case 2	317808	0.8233	19.15
Case 3	475304	0.9936	41.82
Case 4	208116	0.8807	26.58

(a) Traditional   (b) 50% Open

(c) 1/4 Diameter Cut   (b) Large Pan-like

Figure 2.6 Mesh Design of Upgate System for the Four Cases: (a) Traditional Upgate, (b) 50% Open Upgate, (c) ¾ Open upgate, (d) Large Pan-like Upgate

3. RESULTS AND DISCUSSIONS

3.1 RESULTS OF OPTICAL MICROSCOPY

Using an optical microscope, all 72 samples were observed with 500 times magnification. The number of inclusions was counted for each sample. High resolution photos were taken for each inclusion. Generally, sulfides and oxides were the most frequently observed inclusions with sulfide inclusions being recorded more frequently than oxide inclusions.

In steel samples from the 50% open ingot (77C and 76C), large inclusions (15-30µm) were observed in significant amounts and analyzed by SEM-EDS to be carbon-based and silica-based. A hard to remove oxidized layer with large cavities filled with carbon and silica was found at the surface of several samples from 76C and 77C. Large particles in these regions were not counted in the optical analysis; however, some of the silica-based particles were treated as inclusions in ASPEX analysis.

3.1.1 Inclusion Amount Analysis. The total number of inclusions is shown in Figure 3.1(a), 3.1(b), and 3.1(c) for the upper half of the original case, the lower half of 50% open case, and the upper half of 50% open case, respectively. Figure 3.3(d) illustrates the comparison between the upper half of original and 50% open in average inclusion number with their relative position in ingots.

The result shows that more inclusions were found on steel samples taken from the ingot with traditional designed upgate system than that from the ingot with swirl-modified upgate. For the traditional one, the average number of inclusions in the center, mid-radius, and boundary were 248, 265, and 213 respectively at the top of the ingot; however, for swirl-modified system, the number were 193, 107, and 89. At the location of 2/3 height, the average inclusion number of traditional ingot at the center, mid-radius, and boundary were 325, 206, and 196 respectively, comparing to 191, 160, and 94 for the swirl-modified ingot.

(a) The Upper Half of Original

(b) The Lower Half of 50% Open

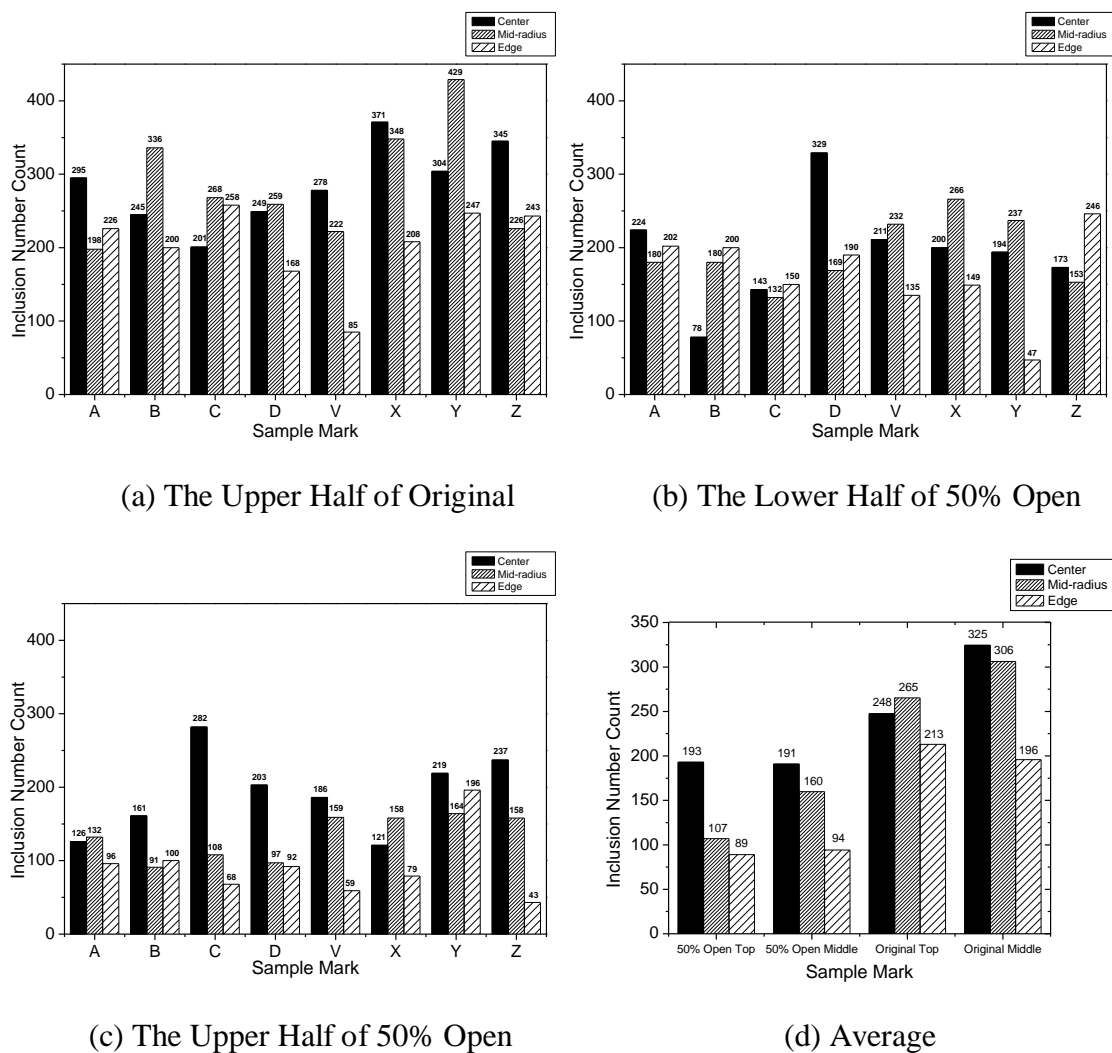(c) The Upper Half of 50% Open

(d) Average

Figure 3.1 Number of Inclusions from Original and 50% Open, and Comparison of Average Between of the Upper Part of Original and 50% Open

To summarize, when only considering the number of inclusions, ingots produced using a swirl-modified upgate system had almost 50% less inclusions at the mid-radius and ingot walls, and 30% less at the center than traditional types of upgate system. Therefore, the change in the swirling flow pattern did reduce the turbulent phenomena throughout the entire ingot. Moreover, a basic conclusion could be inferred that in the bottom-poured ingot casting, inclusions were mainly formed at the center of the ingot and

the top. The swirling flow is more effective on preventing inclusions being entrapped at walls and mid-radius of the ingot

3.1.2. Area Ratio Analysis. When considering the volume and area fraction of inclusions, the area ratio was calculated for each sample to examine the actual area occupied by inclusions in the steel samples (Figure 3.2).
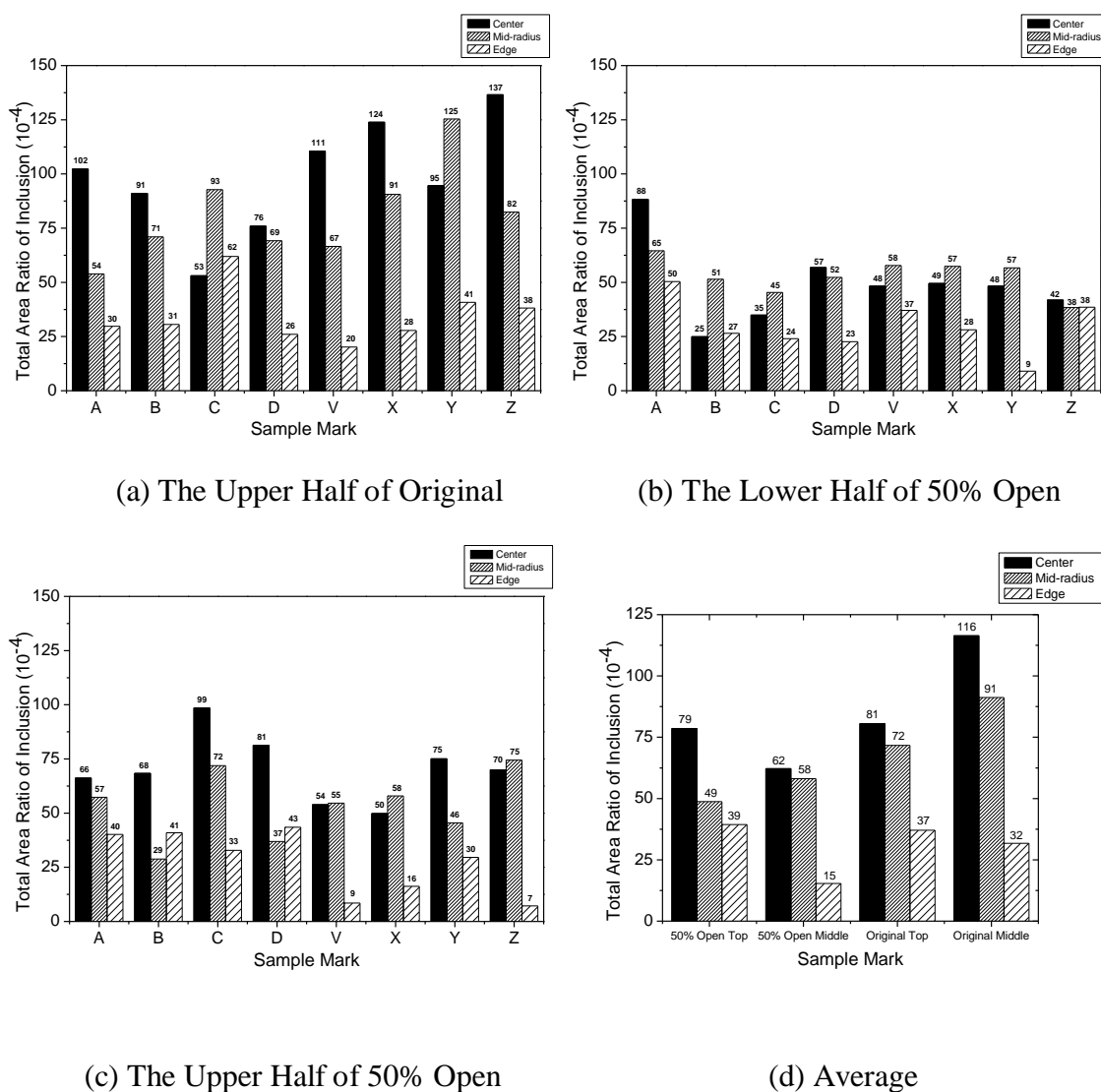

(a) The Upper Half of Original

(b) The Lower Half of 50% Open

(c) The Upper Half of 50% Open

(d) Average

Figure 3.2 Inclusion Area Ratios of Samples from Original and 50% Open, and Average Area Ratio Comparison Between of the Upper Part of Original and 50% Open

The results are shown in Figure 3.2(a), 3.2(b), and 3.2(c) for the upper half of original, the lower half of 50% open, and the upper half of 50% open, respectively. Figure 3.2(d) illustrates the average total area ratio of the upper half of original and 50% open. The results from area ratio calculations of the samples from the 2/3 height of the ingot indicates that the original case has more inclusions detected than that of 50% open. For the traditional upgating, the average area ratio of inclusions in the center, mid-radius, and boundary of ingot were 116×10^{-4}, 91×10^{-4}, and 32×10^{-4} respectively at the middle height. For swirl-modified ingot, these values were 62×10^{-4}, 58×10^{-4}, and 15×10^{-4} respectively. However, no significant difference was found between 75C_ABCD and 77C_ABCD, which is in contrast to the reduction in inclusions shown in the number of inclusions. For the traditional upgating, the average area ratio of inclusions in the center, mid-radius, and boundary of ingot were 81×10^{-4}, 72×10^{-4}, and 37×10^{-4} respectively at the top of the ingot. For swirl-modified ingot, these values were 79×10^{-4}, 49×10^{-4}, and 39×10^{-4} respectively. It is reasonable to conclude that larger inclusions were entrapped at the top of the swirl-modified ingot. Furthermore, this might be caused by the entrainment of mold flux at the top of the swirl-modified ingot.

3.1.3. Size Distribution. The comparison of average area ratio of inclusions in size distribution between original and 50% open is shown in Figure 3.3. Compared to the samples from the top of the ingot (ABCD), the original ingot has a much larger inclusion population in the range of 0~5 μm; however, there is only a slight difference in the inclusion area ratio between the original and 50% open with the inclusion size of 5~10 μm. Furthermore, the sample from the top of 50% open had an even higher inclusion area ratio when considering the large inclusions greater than 10μm equivalent diameter. This indicates that the swirl-modified ingot resulted in a much greater amount of large inclusions at the top of the ingot compared to original gating. There was other evidence of large particles that formed from holes on the surface jammed with polishing material and other silicon containing contamination when observed under optical microscope. Nevertheless, from the comparison of the 2/3 height, the difference between 75C and 77C is apparent (>30%), especially in the range of 2~8μm.
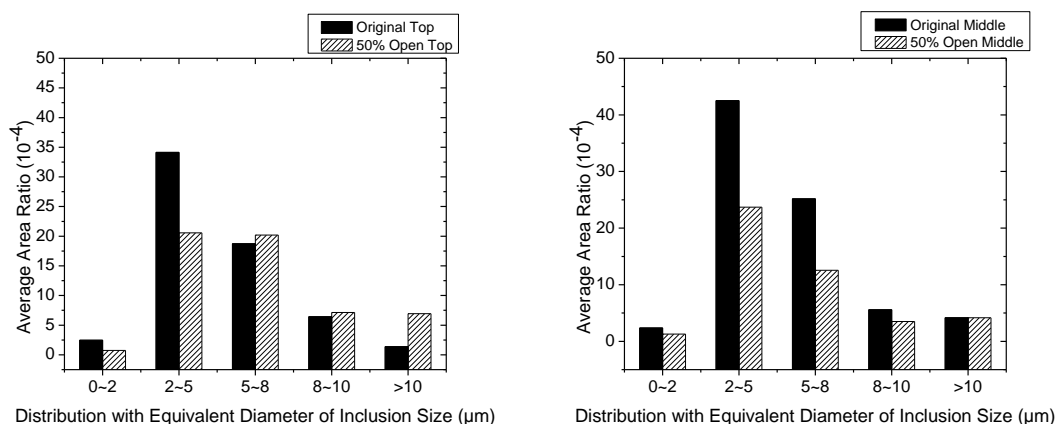
Figure 3.3 Size Distributions of Original and 50% Open with Inclusion Area Ratio (Top and 2/3 Height)

Average total area ratio distributions of inclusion along radial and vertical directions are shown in Figures 3.4 and 3.5. In the radial direction, considering the average area ratio, the traditional upgating ingot had 34.4×10^{-4}, 81.5×10^{-4}, and 98.5×10^{-4} at wall, mid-radius, and center respectively; meanwhile, swirl-modified ingot had 28.5×10^{-4}, 53.2×10^{-4}, and 59.8×10^{-4} at the edge, mid-radius, and center respectively. At the center of the ingot, more inclusions were observed than at the other two positions in the radial direction. 50% less inclusions were distributed at the walls of the ingot than that at the center. The distributions of swirl-modified and traditional ingot were similar to each other. The values of total area ratio at the walls from these two ingots were close to each other, 34.4×10^{-4} for original and 28.5×10^{-4} for 50% open; however, significant differences at mid-radius and the center indicates the effect of swirl flow generated by the upgate system, which were 35% less at mid-radius and 39% less at the center.

As shown in Figure 3.5, the total area ratios of inclusions at different heights of swirl-modified ingot are 42.6×10^{-4}, 45.2×10^{-4}, 45.2×10^{-4}, and 55.6×10^{-4} at bottom, 1/3 height, 2/3 height, and top respectively. The lower three positions have almost the same ratio in value, but approximately 25% more inclusions are observed at the top of the ingot

than other places. However, for the traditional ingot, the total area ratios at 2/3 height and top are 79.8×10^{-4} and 63.1×10^{-4} respectively, which are both far more than that of the swirl-modified case. Based on the difference in inclusion population at the top and 2/3 height, two different flow patterns could be inferred.
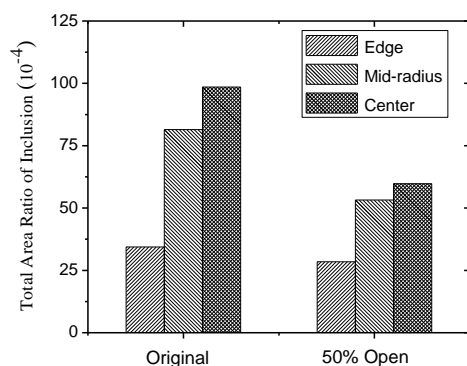

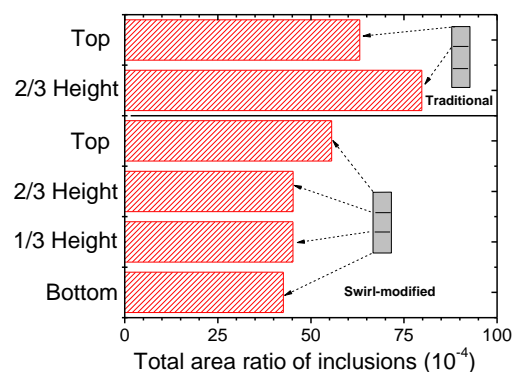Figure 3.4 Total Area Ratio Distribution of Inclusion along the Radial Axis of Ingot

Figure 3.5 Total Area Ratio Distribution of Inclusion at Different Heights of the Ingots

Figure 3.6 illustrates the two side views of the swirl-modified ingot. In Figure 3.6(a), samples of 77C_ACVY and 76C_ACVY were located on this cross section; similarly, 77C_BDXZ and 76C_BDXZ were located on Figure 3.6(b). Average equivalent diameters were calculated in Figure 3.6(a), from which smaller inclusions were found at the bottom of the ingot. Most of the large inclusions were detected at the top. At the middle heights, inclusions tend to have moderate sizes. However, when comparing the results in Figure 3.6(b) where the total area ratio of inclusions were listed, the difference between the bottom, 1/3 height, 2/3 height and the top position were not so apparent. This indicates that although the top layer had larger inclusions distributed there, the amount of these inclusions was not as high as those of the other three layers. Small and regular inclusions like spherical MnS and alumina dendrites should be dominant at the bottom and middle height position in the ingot; however, large inclusions like

alumina cluster and aggregates, multi-phases inclusions should be frequently observed at the top due to floatation.
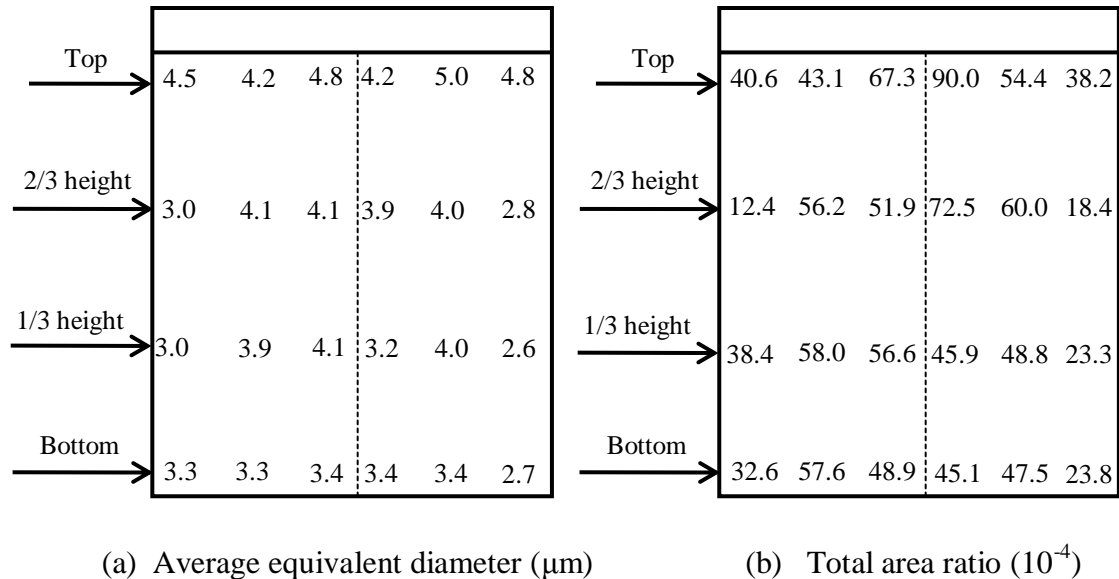
Top →	4.5	4.2	4.8	4.2	5.0	4.8
2/3 height →	3.0	4.1	4.1	3.9	4.0	2.8
1/3 height →	3.0	3.9	4.1	3.2	4.0	2.6
Bottom →	3.3	3.3	3.4	3.4	3.4	2.7

Top →	40.6	43.1	67.3	90.0	54.4	38.2
2/3 height →	12.4	56.2	51.9	72.5	60.0	18.4
1/3 height →	38.4	58.0	56.6	45.9	48.8	23.3
Bottom →	32.6	57.6	48.9	45.1	47.5	23.8

(a) Average equivalent diameter (μm)   (b) Total area ratio (10^{-4})

Figure 3.6 Distributions of Inclusions at the Center Slice of the Ingot with Swirl-Modified Upgate System

Consequently, the swirl-modified upgate had a positive effect on reducing the formation of inclusions and decreasing the size, especially on decreasing the number of small inclusions with a size of 0-8 μm. At the top of the ingot, improved flow patterns with the swirl upgate had no effect on decreasing the large inclusions in size and amount. In fact, it appeared that there might have been an increase in inclusions at the top from either mold flux entrainment or refractory erosion taking place due to the high radial velocity and turbulent energy.

3.2. ASPEX NCLUSION ANALYSIS

Inclusion compositions were superimposed in the ternary phase diagrams of SiO_2-Al_2O_3-CaO and Al_2O_3-MgO-CaO at 1600°C.

If only the four components, SiO_2, Al_2O_3, CaO and MgO are considered, the inclusion composition could be normalized. The results are shown in Figure 3.7.
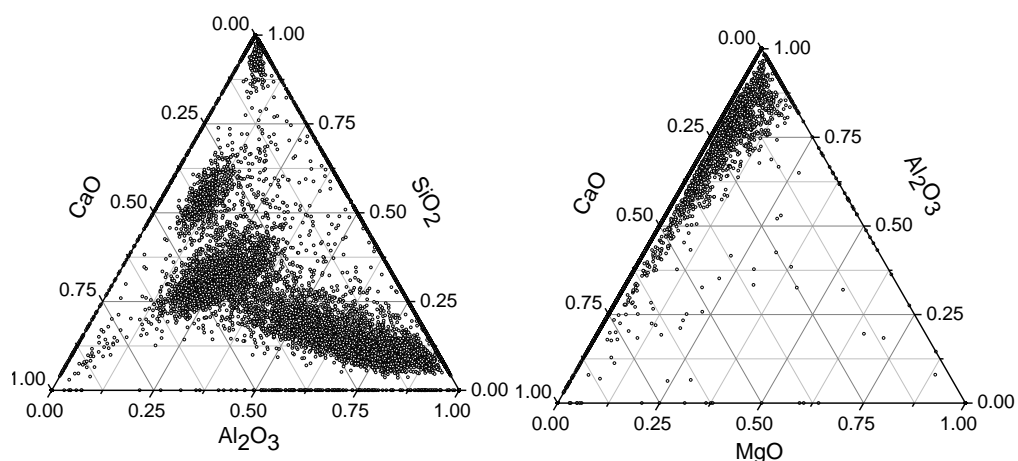
(a) Original Ingot Samples
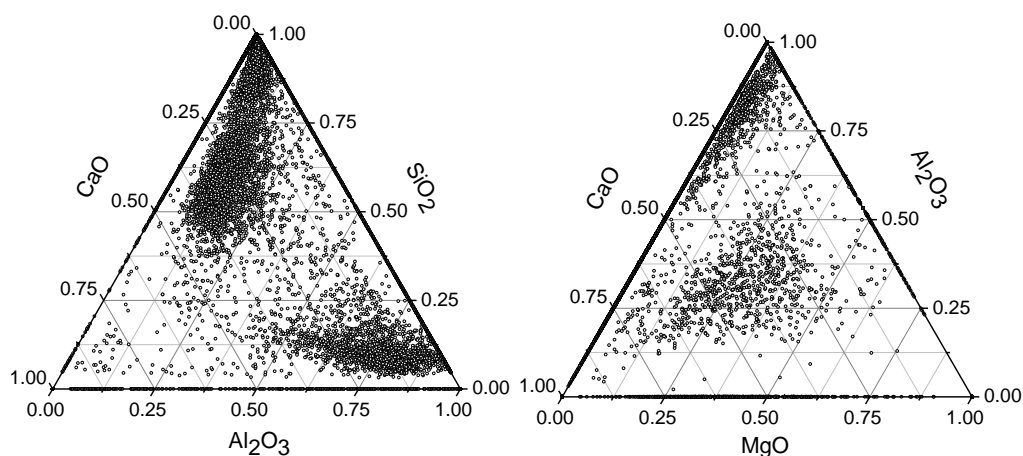
(b) 50% Open Ingot Samples

Figure 3.7 Inclusion Compositions of Steel Samples from Ingots

For traditional ingot samples, inclusions were mainly SiO_2-Al_2O_3-CaO with high silicate and high alumina. For the swirl-modified ingot samples, inclusions were mainly

SiO_2-Al_2O_3-CaO with high silicate and Al_2O_3-MgO-CaO with high alumina. There were far more high SiO_2 content inclusions in the swirl-modified ingot than that of ingot with a traditional upgate.

Figure 3.8 illustrates the comparison of inclusions at different heights of steel samples from the swirl-modified ingot.

(a) Top   (b) 2/3 height

(c) 1/3 height   (d) ingot bottom
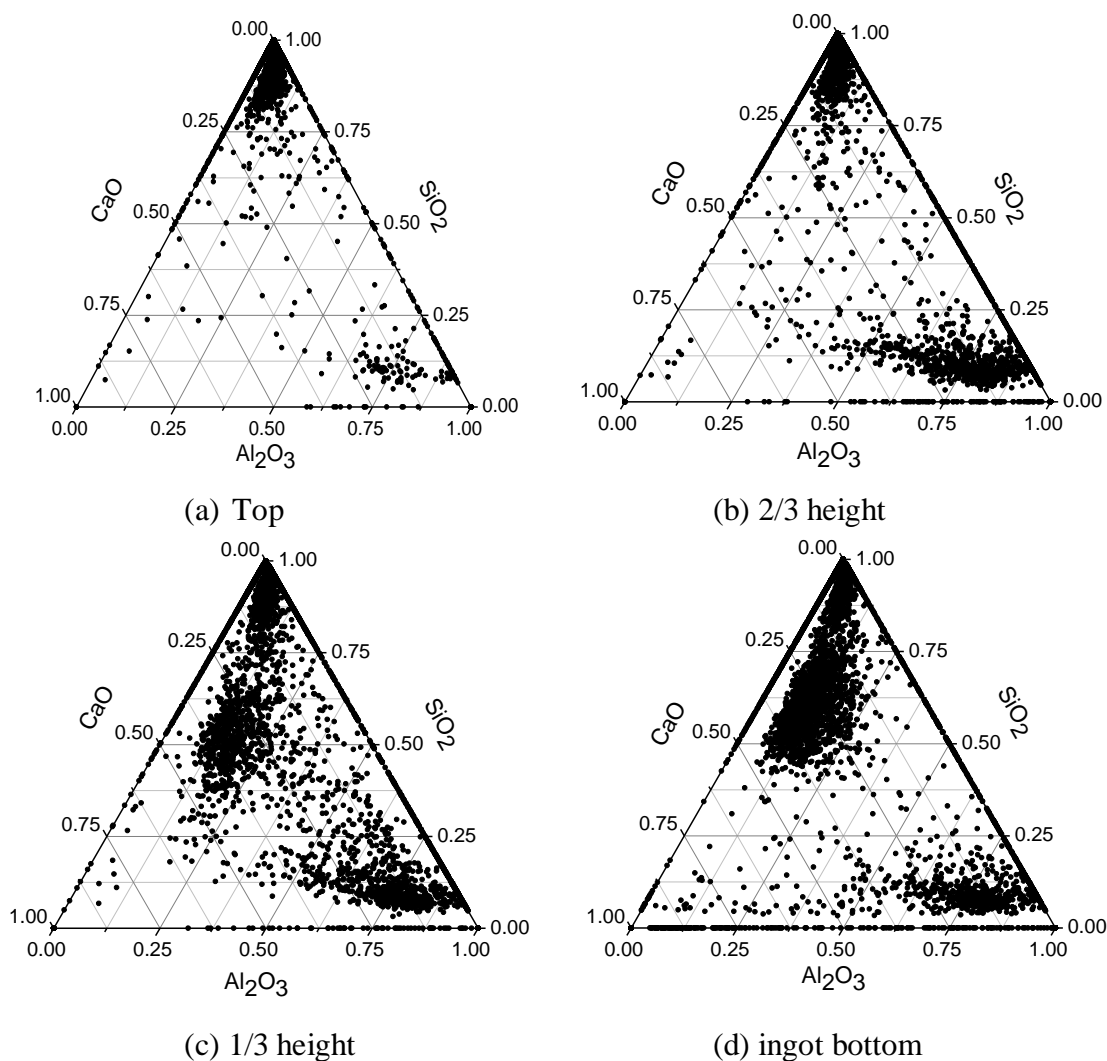
Figure 3.8 Inclusion Compositions at Different Height of the Swirl-Modified Ingot

At the ingot top, inclusions were mainly large sized SiO_2-based inclusions. These inclusions represent particles that should have floated to the top of the ingot. However,

apparently these inclusions or hot-top powders were re-entrained. At 2/3 height of the ingot, inclusions were mainly SiO_2-based and Al_2O_3-based. At 1/3 height of the ingot, calcium silicate appeared with the existence of SiO_2-based and Al_2O_3-based inclusions. At the ingot bottom, more calcium silicate showed compared to that at 1/3 height ingot.

Figure 3.9 compares the compositions of inclusions in samples at different radial positions in the ingot. Close to the outside surface and mid-radius of the ingot, inclusions were mainly high SiO_2-based and high Al_2O_3-based. At the center of the ingot, calcium silicates were predominant.

Moreover, from Figure 3.8 and 3.9 the calcium silicate were found to be located at the bottom of the ingot where r=0. This indicates the strong swirling flow generated by redesigned upgate system which located at the center of the ingot bottom caused the entrapment of slag inclusion. It could be that large complex inclusions have more possibilities of being entrapped due to the strong swirling flow during ingot casting.

(a) r=R   (b) r=1/2R   (c) r=0
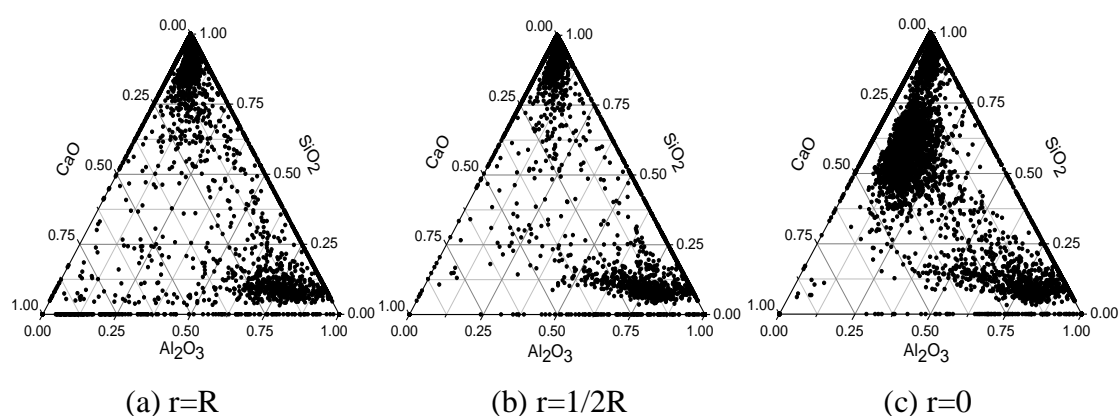
Figure 3.9 Inclusion Compositions at Different Radial Positions of the Swirl-Modified Ingot

3.3. SEM ANALYSIS

Inclusions were detected by scanning electron microscope and their compositions were analyzed by EDS.

3.3.1. Classification of Inclusions. Table 3.1 illustrates the morphology and composition of inclusions in the stainless steel samples, including the following types: **a**. Oxide inclusion; **b**. Sulfide inclusion; **c**. Al_2O_3 dendrite with sulfide shell; **d**.Oxide-sulfide inclusion in strip shape; **e**. Al_2O_3-based multiphase inclusion; **f**. Al_2O_3 chunk cluster. The presence of silicates and spinels were not noticeable in these stainless steel samples. Chromium was detected in the matrix composition. Moreover, secondary precipitation phases were observed under the SEM with molybdenum and vanadium detected in those phases.

As a typical oxide inclusion, Table 3.1(a) contains almost all oxide compositions. Alumina dominates with 42% wt with 27% wt manganese oxide and 16% wt silicate accompanied. Titanium oxide, calcium oxide, and magnesium oxide are all detected with low content of 3~6% wt.
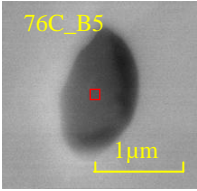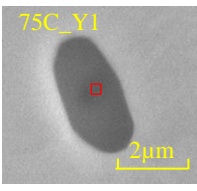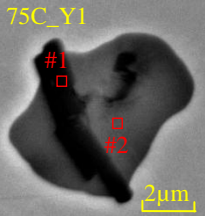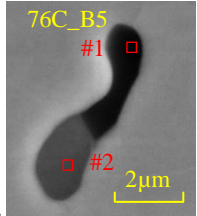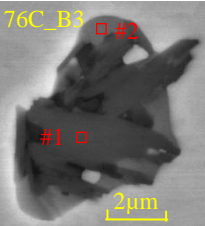
Table 3.1(b) is a typical sulfide inclusion. Redundant sulfur is remaining after binding with manganese, which could be in the form of (Mn, Fe)S. Except for the high content of Mn and S, 27% wt alumina and other oxides like SiO_2 and MgO are detected. This could be owing to the formation mechanism that sulfide precipitated onto the oxide.

Table 3.1(c) and 3.1(d) are both sulfide-oxide inclusions, but in different shapes. Sulfide has two directions to precipitate on the alumina dendrite. One is along the longitudinal path which is consistent with the direction of alumina growth. The other is in the transverse direction where the sulfide phase grows around the dendrite. The dark phase in the two inclusions is dominated with high contents of oxide like alumina, calcium oxide, or silicate. The gray phase has high sulfur compounds mainly in MnS. However, Al_2O_3 and other oxide rich areas are still found in these gray parts, which also could be explained by the precipitation of MnS on alumina.

Table 3.1(e) is a multiphase inclusion. With the phase color turns darker, oxides content increases like silica, calcium and magnesium oxide.

Table 3.1(f) is a typical alumina cluster. It is formed by collision and coalescence of alumina dendrites during filling and solidification process.

Table 3.1 Morphology and Composition of Inclusions with Different Types
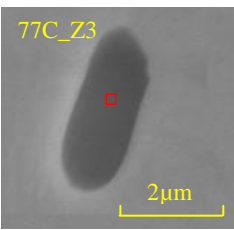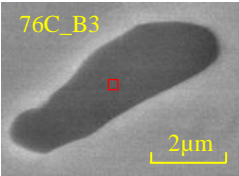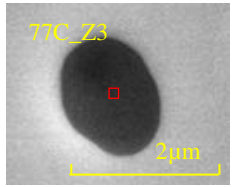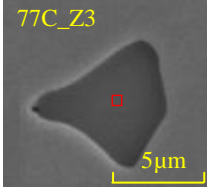
a.	Al$_2$O$_3$: 42.8%	b.	MnS: 52.8%
	MnO: 27.5%		Oxide: 33.7%
	Other Oxide: 29.9%		[S]: 13.6%
c.	#1) Oxide: 86.4%, Sulfide: 11.5%	d.	#1) Oxide: 98.8%, Sulfide: 1.1%
	#2) Oxide: 44.4%, Sulfide: 37.3%		#2) Oxide: 5.2%, Sulfide: 75.6%
e.	#1) Oxide: 96.3%, Sulfide: 2.8%	f.	Al$_2$O$_3$: 80.5%
	#2) Oxide: 44.1%, Sulfide: 42.0%		MnS: 2.0%, Other Oxide: 17.4%

3.3.2. Sulfide and Oxide. Both Table 3.2 and Table 3.3 show the two basic types of inclusions mainly observed under SEM. Sulfide inclusions appear in sphere, rod, and polygon shape. For the former two types, the inclusions observed are small in size (equivalent diameter = 2-5µm); however, inclusions in the polygon shape always grow to more than 5µm in diameter. As shown in the table, the sulfide inclusions have an identical composition with almost 70% wt of MnS, excessive sulfur, and low amounts of oxide like alumina, silica, and titanium oxide. When excessive sulfur exists, calcium has the possibility to form CaS. Also, excessive sulfur is in the state of (Fe, Mn)S mentioned

above. Different contents of oxides are detected in low amounts which are on account of oxide dendrites with different sizes containing the sulfides.

Oxide inclusions vary quite significantlyin morphology and composition. Alumina, silica, spinel, and mixed content are all observed. Alumina inclusions always have high content of Al_2O_3 (>80 %wt). MnO is accompanied with SiO_2 in silica inclusions. In the mixed content inclusions, Na_2O and CaO are also detected.
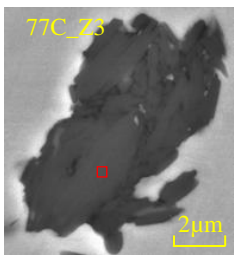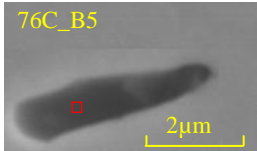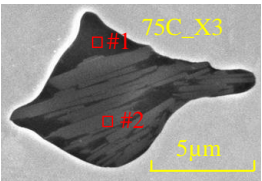
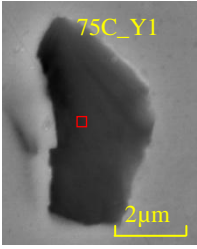Table 3.2 Morphology and Composition of Sulfide Inclusions

a. 77C_Z3 2μm	MnS: 67.6%, CaS: 0.6%,	b. 76C_B3 2μm	MnS: 72.1%, CaS: 0.2%,
	Oxide: 5.4%, [S]: 25.6%		Oxide: 2.8%, [S]: 23.5%
c. 77C_Z3 2μm	MnS: 64.7%, CaS: 0.9%,	d. 77C_Z3 5μm	MnS: 67.7%, CaS: 2.3%,
	Oxide: 13.3%, [S]: 21.0%		Oxide: 3.4%, [S]: 25.8%

In Table 3.4 and Table 3.5, the two forms of inclusions with two phases of alumina and manganese sulfide are shown in detail. Al_2O_3 dendrites with a sulfide shell are the frequently observed inclusions in these steel samples. The formation mechanism should be the precipitation of different phases during liquid steel cooling. Al_2O_3 dendrites exist after they form in the temperature range of 1500°C to 1600°C [11]. With the temperature of the steel matrix dropping, MnS begins to precipitate on the particles of Al_2O_3 dendrites, which is easier than homogeneous nucleation when dendrites are in a region with high sulfide content [12]. The images in Table 3.4 show the sulfide shell (gray part) and the alumina dendrite (dark part). The composition of the gray part

indicates that a sulfide shell only covers the surface of the dendrites as a result of relative high content of alumina that is detected in the gray part. These sulfide shells (20%~30%) are not in the same composition level of MnS comparing to pure MnS inclusions (60%~70%) in Table 1.

Table 3.3 Morphology and Composition of Oxide Inclusions

a.	Al_2O_3: 88.6%,	b.	SiO_2: 58.3%, Al_2O_3: 9.8%,
	Other Oxide: 10.7%, Sulfide: 0.6%,		Other Oxide: 30.7%, Sulfide: 1.1%
c.	#1) Al_2O_3: 44.0%, CaO: 27.1%, SiO_2: 24.0%,	d.	Al_2O_3: 85.7%
	#2) Al_2O_3: 93.2%, CaO: 0%, SiO_2: 4.5%		Other Oxide: 12.6%, Sulfide: 1.0%

The rod-like inclusions are expected when considering the mechanism of MnS precipitation on Al_2O_3 dendrites. The gray part in the images in Table 3.5 representa areas of high alumina indicating the possibility of MnS precipitating on one end of an alumina dendrite and growing to form another phase. This is in agreement with the observations with the optical microscope in which rod-like inclusions with two phases were found to be common. Moreover, this could be the basic particles forming the large inclusions in the matrix especially for the inclusions in Table 3.4, which look like some of the dendrites are bounded together by MnS precipitation.

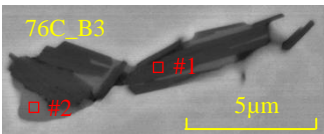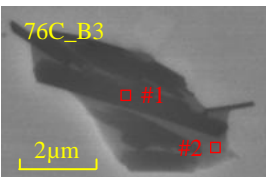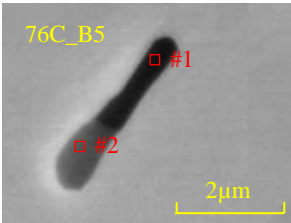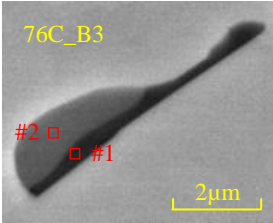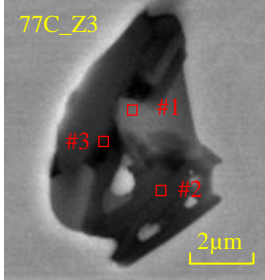Table 3.4 Morphology and Composition of Al_2O_3 Dendrite with Sulfide Shell
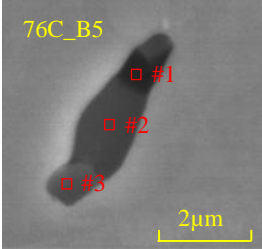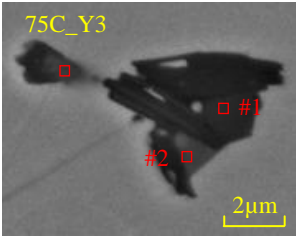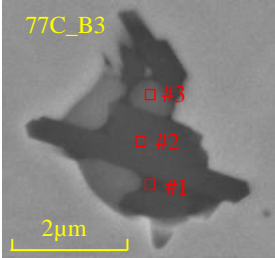
	#1) Oxide: 88.3%, Sulfide: 11.4%		#1) Oxide: 86.3%, Sulfide: 13.3%
	#2) Oxide: 46.6%, Sulfide: 39.3%, [S]: 13.7%		#2) Oxide: 41.2%, Sulfide: 28.7%, [S]: 9.5%

Table 3.5 Morphology and Composition of Oxide-Sulfide Inclusion in Strip Shape

	#1) Oxide: 86.4%, Sulfide: 11.5%, [S]: 2.0%		#1) Oxide: 33.5%, Sulfide: 48.0%, [S]: 17.6%
	#2) Oxide: 44.4%, Sulfide: 27.3%, [S]: 18.2%		#2) Oxide: 20.5%, Sulfide: 58.9%, [S]: 20.4%

3.3.3 Large Inclusions. Multiphase inclusions are normally irregular in shape as shown in Table 3.6. With the color getting darker, the content of Al_2O_3 increases and MnS decreases. SiO_2, MgO, CaO, CaS, and TiO_2 are all detected in these inclusions. The formation mechanism of multiphase inclusion should be the effect of the temperature gradient and flow pattern in the matrix during solidification.
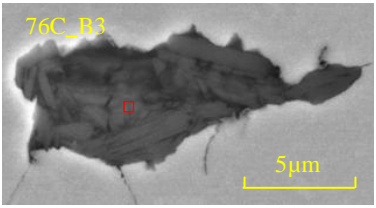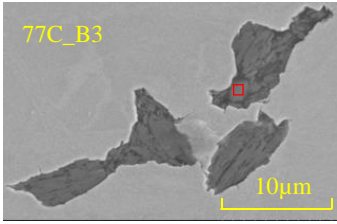
Table 3.6 Morphology and Composition of Al_2O_3-Based Multiphase Inclusion

	#1) Oxide: 64.8%, Sulfide: 24.9%		#1) Oxide: 72.0%, Sulfide: 28.0%
	#2) Oxide: 85.7%, Sulfide: 13.9%		#2) Oxide: 4.7%, Sulfide: 75.6%
	#3) Oxide: 93.8, Sulfide: 5.9%		#3) Oxide: 25%, Sulfide: 69.6%
	#1) Oxide: 96.4%, Sulfide: 3.6%		#1) Oxide: 97.3%, Sulfide: 2.6%
	#2) Oxide: 69.7%, Sulfide: 22.4%		#2) Oxide: 96.5%, Sulfide: 3.4%
	#3) Oxide: 29.7%, Sulfide: 55.8%		#3) Oxide: 77.5%, Sulfide: 22.4%

Alumina chunk clusters are inclusions that are gathered together, so they appear to be large in size (>5µm) and would be very detrimental to steel quality as shown in Table 3.7. Collision and aggregation are the formation mechanism for these alumina cluster due to the high interfacial energy of Al_2O_3 particles [5]. Clusters contain most of the bonded oxygen and together with the large multiphase oxides are very detrimental to the steel quality.

Coalescence could play an important role in the formation of alumina clusters would be the way of inclusion growth. Therefore, when considering the total oxygen content (O_{tot}), steel with extreme low oxygen content could be achieved by removing these inclusions.

Table 3.7 Morphology and Composition of Al_2O_3 Chunk Cluster

76C_B3 5µm	Al_2O_3: 81.8% Other Oxide: 7.5%, Sulfide: 0.2%	77C_B3 10µm	Al_2O_3: 60.2%, Other Oxide: 39.3%, Sulfide: 0.5%

3.3.4. Inclusion Comparison. SEM observation and EDS detection have been completed on the samples. Table 3.8 summaries the inclusions observed in samples from original and 50% open. These four samples have 4 classes of types: sulfide, oxide, oxy-sulfide, and others for simplicity. The other types include Al_2O_3 clusters, complex silicates or other oxide based multiphase inclusions.

Table 3.8 Summary of Inclusions with 4 Types Classified

	Total inclusions observed	Sulfide	Oxide	Sulfide-Oxide	Other Type
Original	14	3	6	5	0
50% Open	13	3	4	5	1
Original	15	5	5	4	0
50% Open	9	1	4	2	2

As shown in Table 3.8, eight sulfide inclusions were detected in 75C; however, only four were found in 77C. Other types of inclusions were only observed in 77C. There were not significant differences between the samples in oxide and sulfide-oxide

inclusions. The differences in the flow pattern when the upgate system changed to swirling flow appears to have decreased the formation of sulfide inclusion, but also caused the emergence of more inclusions with rare types.

3.3.5. Inclusion Formation Mechanism. From the results of the SEM observations, the formation mechanisms of inclusions in ingot steel casting are discussed below.

As illustrated in this chapter, sulfide and oxide inclusions are the main types of inclusions in ingot-cast stainless steel. In special steels, sulfide, alumina, and their combination are the three main types of inclusions [15].

Sulfide inclusions are mainly manganese sulfide with a small quantity of calcium sulfide. The content of CaS can differ from 0-3 wt%, mostly within the range of 0-1 wt%.

$$[Mn] + [S] = MnS_{(s)} \tag{1}$$

$$CaO_{(s)} + [S] = CaS_{(s)} + [O] \tag{2}$$

Reaction (1) represents manganese sulfide inclusion formation by the dissolved Mn and S reacting in liquid steel. The standard Gibbs free energy for reaction (1) is:

$$\Delta G^0 = -168822 + 98.87T \left(J \cdot mol^{-1} \right) \tag{3}$$

At 1873K, ΔG^0 is 16361 J·mol^{-1} calculated by equation (3); however, when the temperature drops to 1700K, ΔG^0 is reduced to -743 J·mol^{-1}. Therefore, the driving force of formation of MnS is not sufficient at steelmaking temperature, but as cooling and solidification proceed to around 1500K, ΔG^0 is down to -20517 J·mol^{-1} which generating enough driving force to precipitate MnS inclusions. The sulfur solubility sharply increases with increasing relative content of MnO in the system; however, it also dramatically decreases with decreasing temperature at certain ranges of MnO [12].
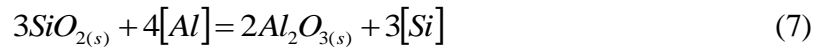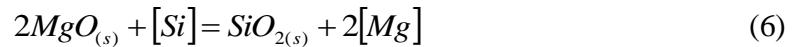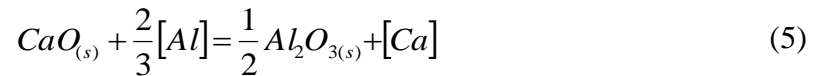
Furthermore, the formation of MgS and Al$_2$S$_3$ need such a high activity of sulfur that it is less possible for them to emerge than MnS and CaS during solidification. Inclusions with sulfur content are only detected in the ingot and the final product but not during casting and mold filling [7]. The dissolved sulfur that comes from mold powder has the possibility to react with inclusions formed in ladle treatment.

Oxide inclusions consist of Al_2O_3-based and SiO_2-based classes. They all contain small amounts of CaO and MgO. Moreover, an oxide shell with higher content of CaO and SiO_2 has been found on some of the Al_2O_3-based inclusions. Al_2O_3 particles are always considered as spinel-type inclusions in stainless steel [2].

Sulfide-oxide inclusions are detected quite often in SEM observations with two or more phases. The sulfide part always appears as a shell around the oxide crystal, which can be explained by precipitation at different temperatures during cooling.

Earlier studies indicate the different precipitation temperature of sulfide and oxide inclusions. According to the Al_2O_3-CaO phase diagram, pure CaO would also precipitate from the casting temperature [7]. When the temperature drops from 1830K, the decreased oxygen solubility of the steel causes precipitation of aluminum oxide.

The formation of Al_2O_3-based inclusions has the following equilibrium equations [13]:

$$2[Al] + 3[O] = Al_2O_{3(s)} \tag{4}$$

$$CaO_{(s)} + \frac{2}{3}[Al] = \frac{1}{2}Al_2O_{3(s)} + [Ca] \tag{5}$$

$$2MgO_{(s)} + [Si] = SiO_{2(s)} + 2[Mg] \tag{6}$$

$$3SiO_{2(s)} + 4[Al] = 2Al_2O_{3(s)} + 3[Si] \tag{7}$$

$$(MgO) + (Al_2O_3) = MgAl_2O_{4(s)} \tag{8}$$

The standard Gibbs free energy for reaction (4) is:

$$\Delta G^0 = -1202000 + 386.3T \left(J \cdot mol^{-1} \right) \tag{9}$$

Referring to the oxide dendrites surrounded with a sulfide shell, it can be inferred that one important formation mechanism of sulfide-oxide inclusions is sulfide precipitation on the nuclei of oxide crystal during cooling during solidification from 1800K to 1500K. Therefore, depending on the size and initial composition of the oxide dendrite, several types of inclusions can form.

First, if the oxide dendrite is small enough and the contents of [Mn] ([Ca]) and [S] are much higher than [Al], [Si], and [O], then almost pure sulfide precipitates on the oxide nuclei and grows to form a sulfide inclusion with low or even no content of oxide detected.

Secondly, if the oxide dendrite is large enough but the contents of sulfide in the surrounding environment are still high, oxide inclusions with a sulfide shell form as the temperature drops down. Part of the sulfur content is dissolved into the oxide dendrite.

Third, if the oxide dendrite is large; moreover, the contents of sulfide and oxide are both high enough to precipitate simultaneously, then multiphase inclusions form.

At last, if the contents of sulfide are so low that only oxide precipitates onto the oxide crystal, then one oxide shell with higher amount of CaO and SiO_2 will form.

Therefore, large inclusions include oxy-sulfide types, multiphase types, and alumina cluster types form above the liquidus temperature. However, the majority of sulfide inclusions are small in size. MnS precipitates mostly on existing inclusions, which enlarge the size of them and takes place at temperatures below 1500K.

3.4 FLUID FLOW RELATED TRANSPORT PHENOMENA DURING INGOT CASTING

Case 1 (Original Upgate) and Case 3 (75% Open) proceeded to 10 seconds after the molten steel entered the ingot bottom. Case 2 (Half Open) and Case 4 (Whirlgate) ran for more than 400 seconds until their completion. This is because after comparing the four cases at 5 seconds, Case 2 and Case 4 have more typical fluid flow motion affected by the redesigned upgate systems. Case 1 is the control set for comparison. As an example, the filling process of molten steel in Case 2 is illustrated in Figure 3.10.

At 0.5 seconds, the steel phase flowed into upgate system through the inlet and runner. Due to high inlet speed and the half-open shape of the connection between inlet and upgate system, reverse flow occurred and the fluid flow was accelerated to enter the upgate bottom. After 1.5 seconds, the molten steel entered the bottom of the ingot but the air phase was still present in the runner. At around 8 seconds, molten steel reached the ingot mold at the location near the inlet direction. Then the steel phase continued to cover the bottom of ingot at 11.25 seconds. Once the liquid phase flowed into the ingot mold, the free surface of molten steel rose as time went on. The whole procedure of filling process took almost 450 second for liquid steel to fill the top of ingot in the simulation domain that was the quarter height of the real ingot system.
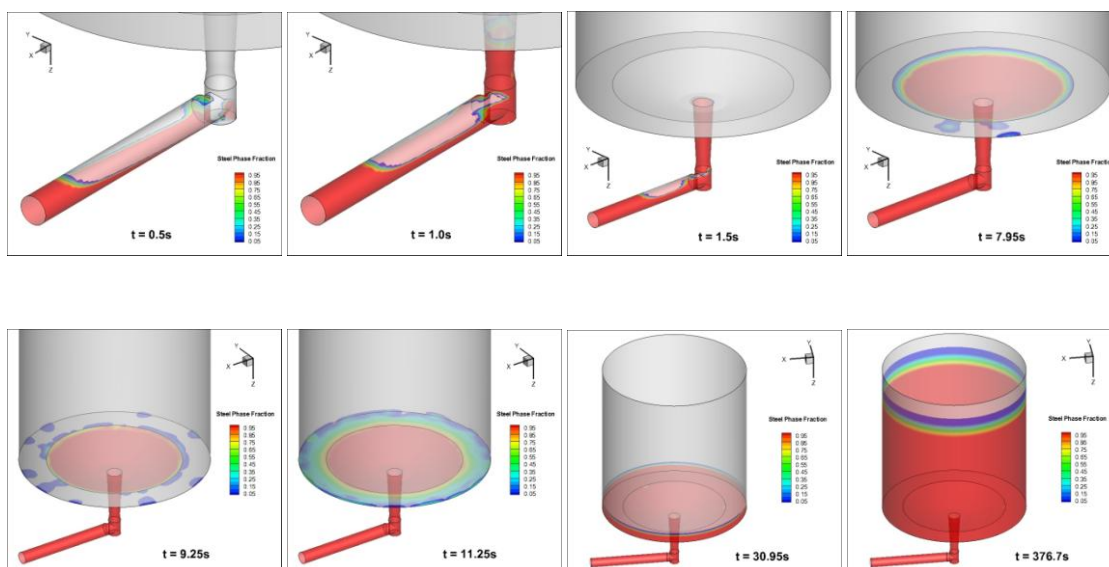
Figure 3.10 Instantaneous Phase Fraction of Liquid Steel in Ingot

Due to the shape and volume factors of the different designed upgates, the flow rate of steel phase and the speed of the filling differed among the four cases.

3.4.1. The Effectiveness of Different Upgate Systems of Four Cases. After running for almost 5.0 seconds, the molten steel had already entered the ingot bottom through the runner and upgate system. Thus, velocity vectors and distributions of turbulent kinetic energy were plotted at the cross section of the four cases in Figure 3.11 and 3.12 to examine the effectiveness of different upgate systems on fluid flow in the filling process.

In Figure 3.11, the areas with high turbulent kinetic energy were located at different places in the four cases. Red areas which could be seen at the top of the ingots free surface in original and 75% open represent the air phase. But when comparing the four cases, less turbulence appeared at the area near the surface in the steel phase in 50% open and whirlgate; instead, the area with high turbulent energy could be seen at the connection of the runner and upgate system, which has little influence on the fluid flow in the ingot.

(a) Original, t=5.0s   (b) 50% Open, t=5.0s

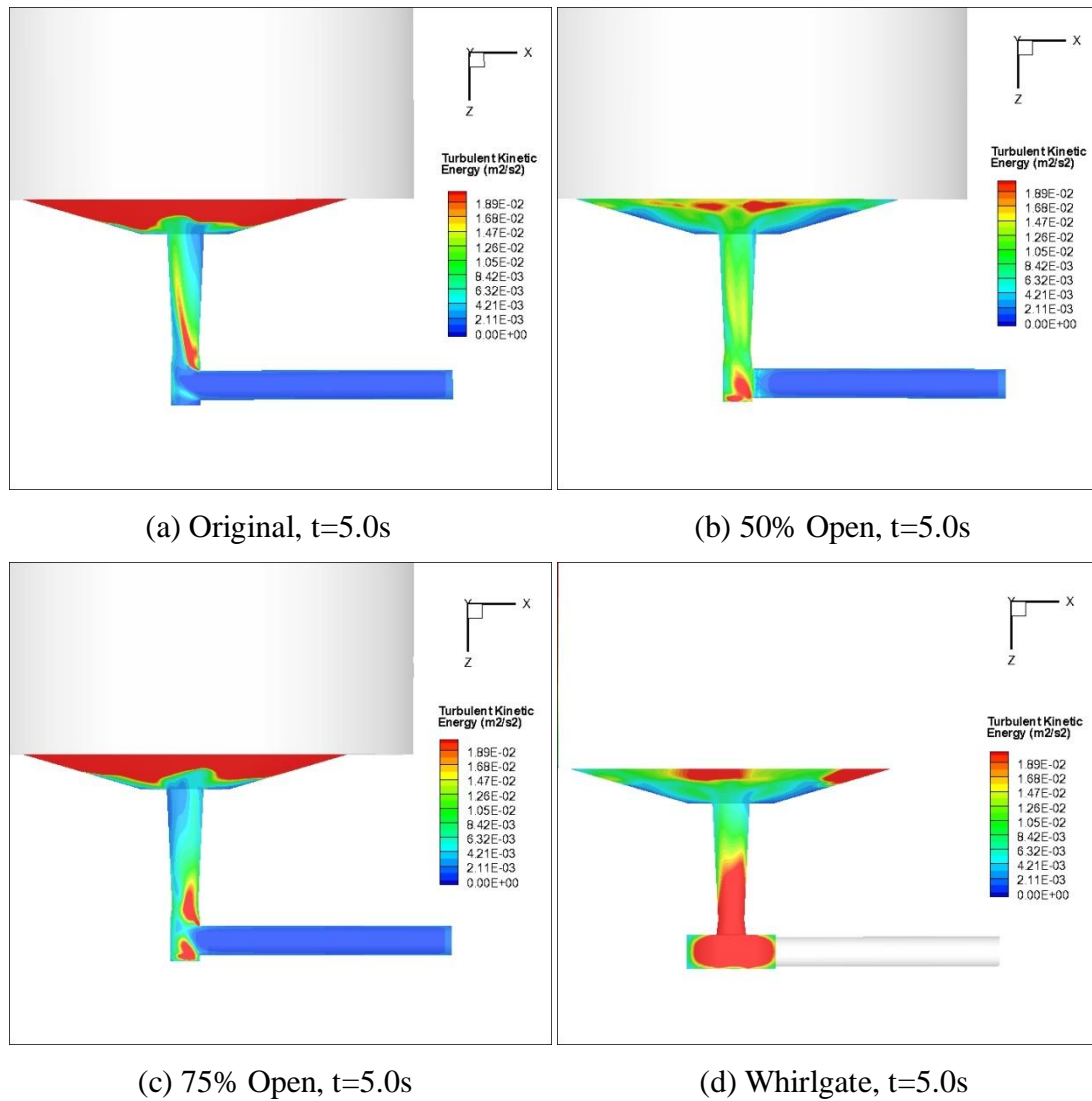(c) 75% Open, t=5.0s   (d) Whirlgate, t=5.0s

Figure 3.11 Contours of Turbulent Energy Distributions at Upgate and Ingot Bottom on XZ Plane

As shown in Figure 3.12, the velocity vectors at the top surface of steel phase of original and 75% open are in the range of 2.11×10^{-1}m/s to 3.16×10^{-1}m/s; however, the velocity vectors of 50% open and whirlgate are in the range of 1.05×10^{-1}m/s to 2.11×10^{-1}m/s. This, again, indicates that 50% open and whirlgate have better controls on radial velocity of the steel phase and its evenness. Moreover, distribution of velocity vectors with more symmetry could be seen in these two cases.

(a) Original, t=5.0s   (b) 50% Open, t=5.0s

(c) 75% Open, t=5.0s   (d) Whirlgate, t=5.0s
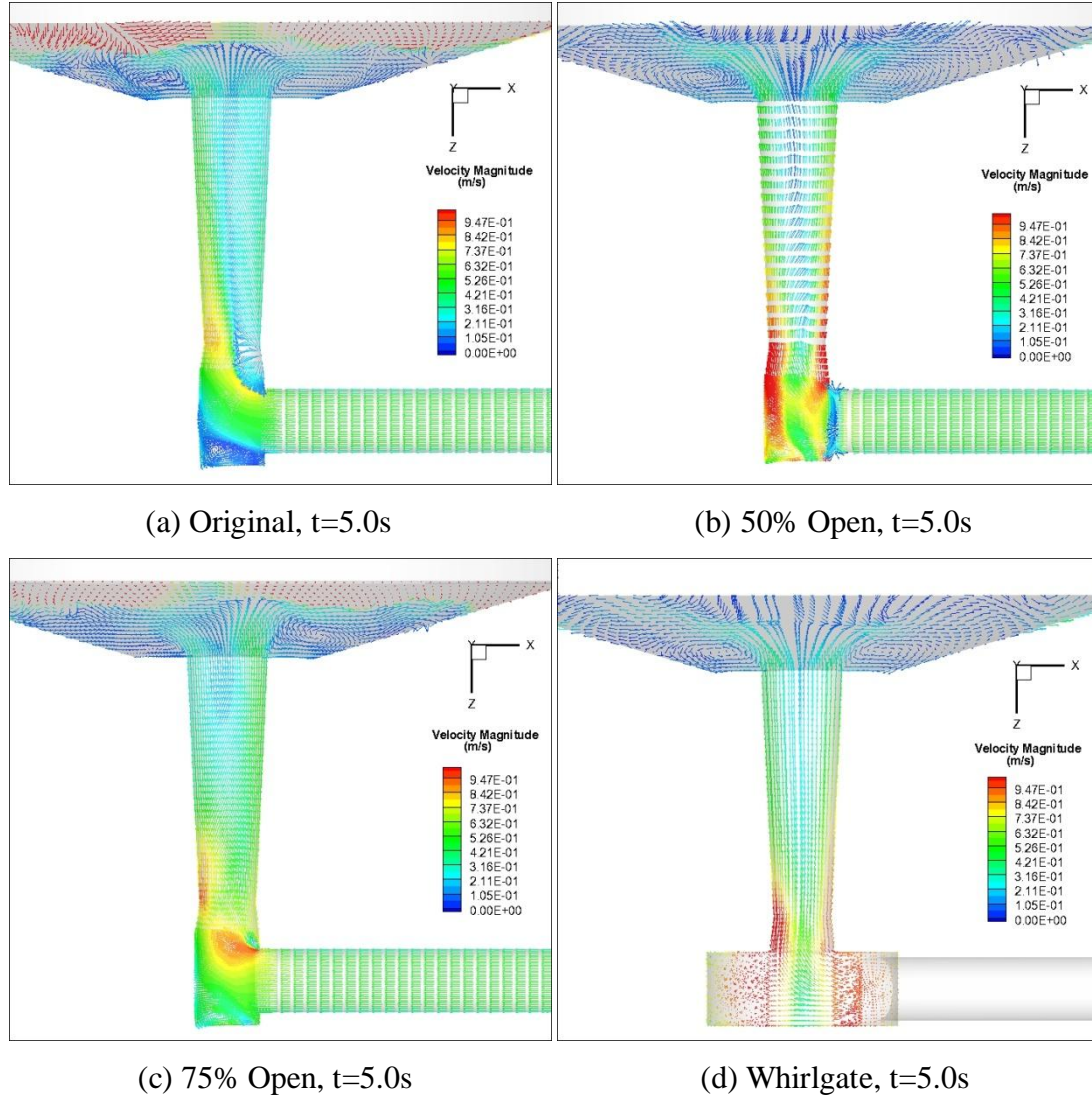
Figure 3.12 Velocity Vector Distributions at Upgate and Ingot Bottom on XZ Plane

3.4.2. Transient Phenomena of Fluid Flow of Steel Phase in 50% Open.
Because the industrial trial was carried out with the 50% open upgate, Case 2 was examined in detail. When the molten steel approached the top of the ingot (1/4 height in industrial model), the state of the fluid flow pattern in the liquid steel was examined. Figure 3.13 shows the velocity contour and vectors at t=443.5s in the XY and YZ plane.

(a) 50% Open, Plane XZ   (b) 50% Open, Plane YZ

(c) 50% Open, Plane XZ   (d) 50% Open, Plane YZ
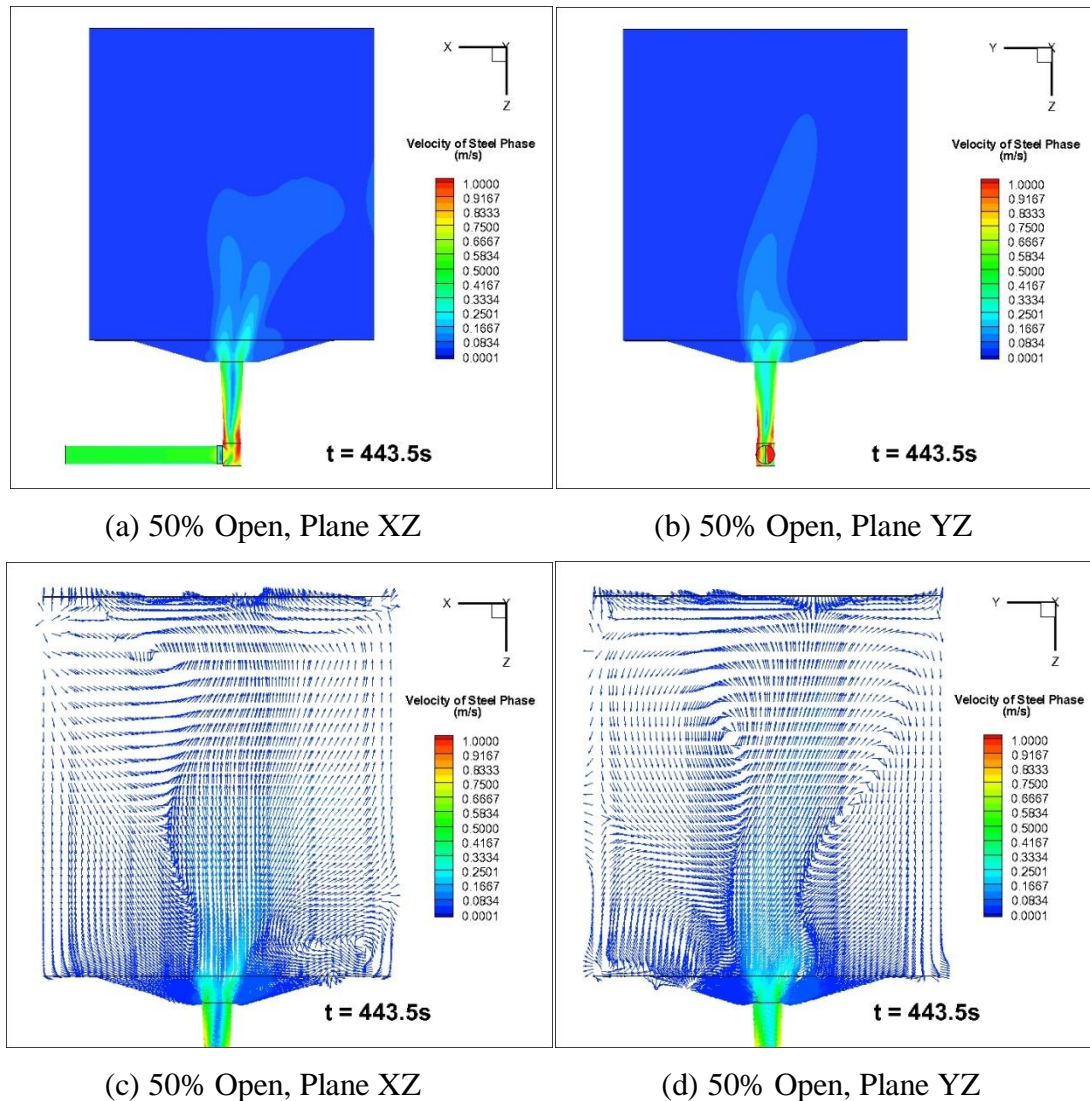
Figure 3.13 Contours and Vectors of Steel Phase Velocity at t=443.5s on XZ and YZ Planes

Vertical recirculation flow patterns were seen in the figures of velocity contours with different colors distributed by values of velocity magnitudes. Also, the deviation of the recirculation shown in the YZ plane is the result of the design of the upgate system with the inlet half blocked at the connection of the runner and upgate. The different velocities of the steel phase which show areas with lighter colors at the two sides but darker area in the middle of the ingot illustrate the existence of recirculation flow.

The vectors in the XZ plane demonstrate the main flow that comes from the upgate system with a bent shape that reaches the top of the ingot. These vectors form a

recirculation with the backflows at the left top. Meanwhile, another recirculation region forms at the right bottom of XZ plane. From the figure of the YZ plane, two vortexes also could be seen near the area of recirculation flow and backflows dominate at both sides. Thus, boundaries between upwind flow and backflow form at the center part of the ingot. Moreover, non-uniform vectors appear at the top of ingot, which implies the possibility of mold flux entrainment.

In Figure 3.14, the velocity vectors are checked at the region of the ingot bottom in XZ and YZ plane.
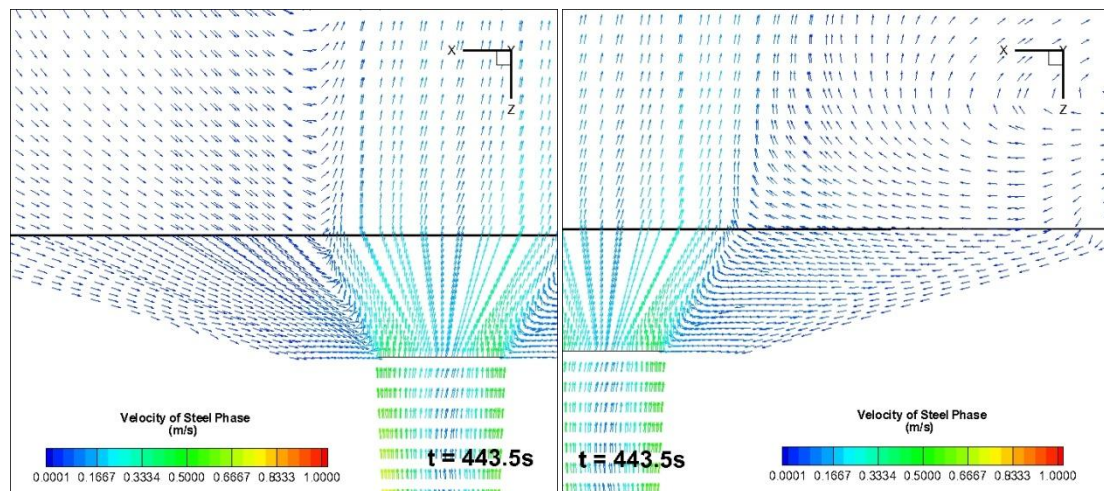
(a) 50% Open, Plane XZ
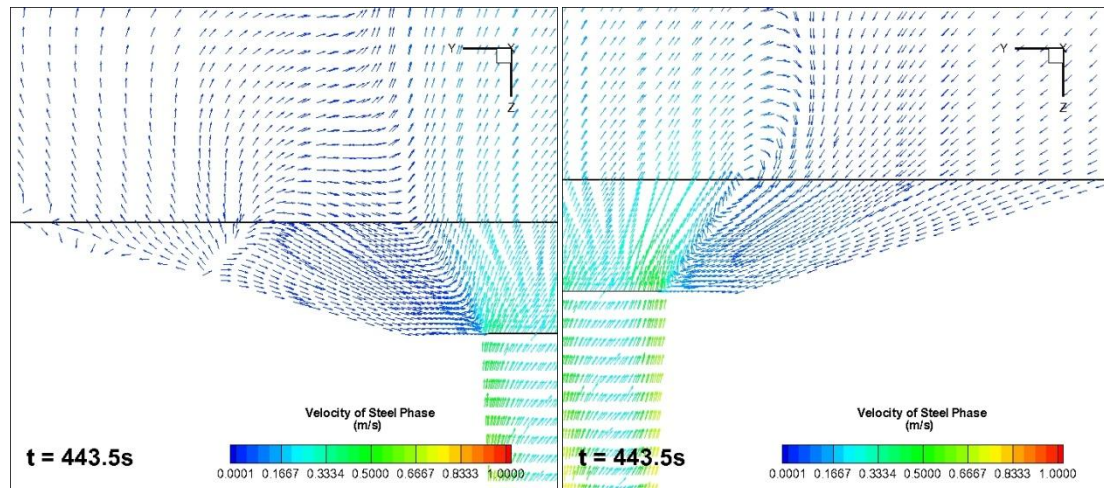
(b) 50% Open, Plane YZ

Figure 3.14 Vector of Steel Phase Velocity for Ingot Bottom and Upgate at t=443.5s on XZ and YZ Planes
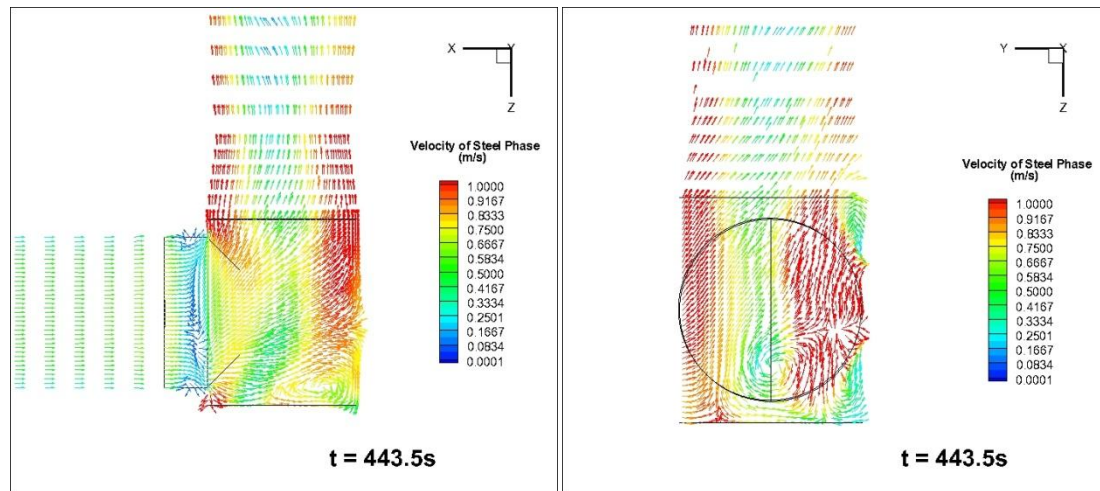
(c) 50% Open, Plane XZ   (d) 50% Open, Plane YZ

Figure 3.14 Vector of Steel Phase Velocity for Ingot Bottom and Upgate at t=443.5s on XZ and YZ Planes (Cont.)

The details of the main flow of molten steel with upward velocity, the backflows, and their interaction layer are described. Through the figures of velocity vectors of the upgate system in XZ and YZ plane, a complex and strong recirculation flow is shown (Figure 3.14). Two small eddies with different directions can be seen at the bottom of this upgate.

To examine the steel phase motion on the full scale of ingot, path lines of the molten steel are shown in Figure 3.15.

From these path lines, whirling upward trajectories are observed, which again indicates the existence of swirling flow with higher speed at the location from the connection between the end of runner and upgate to the top of upgate system. However, the path lines show less swirling shape at the upper positions in the ingot and the swirl expanded to a larger size with slower speed above the upgate top in the ingot. As shown in Figure 3.15, the molten steel was transferred through complex trajectories.
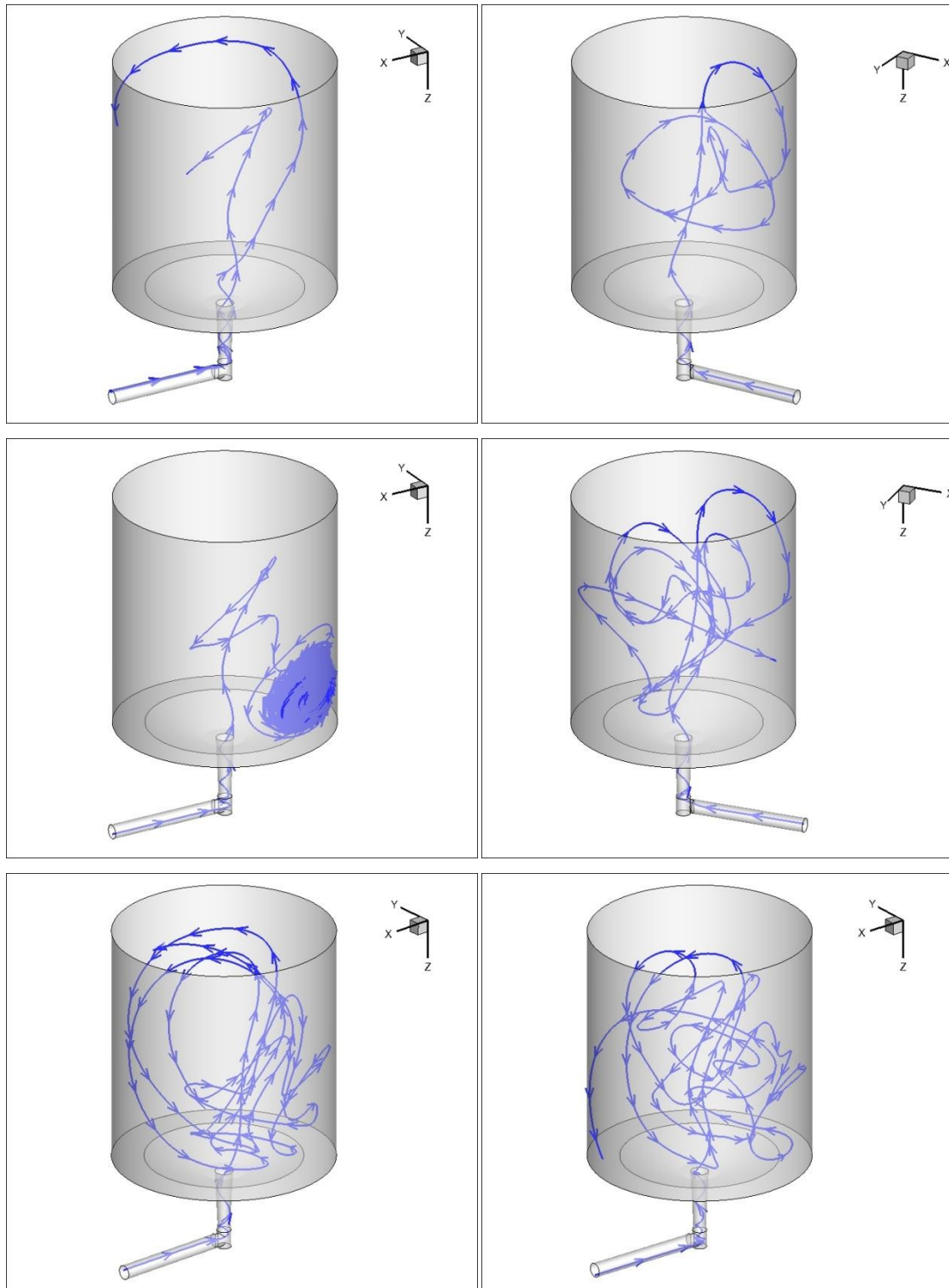
Figure 3.15 Different Path Lines of the Molten Steel during Filling Process (50% Open)

At last, the turbulent energy in the XZ and YZ plane at t=443.5s was examined in Figure 3.16. The top of the ingot and the center region at the ingot bottom are shown to have higher turbulent energy at this transient moment. The higher turbulent energy at the top surface was due to the gas phase there and the mixing between the molten steel and the gas phase was very strong, and furthermore, the pressure outlet boundary condition at the top might generate a certain back flow that had big turbulent energy and its dissipation rate. The vigorous stirring at the top would entrain mold flux to generate large slag inclusions in the final ingot.
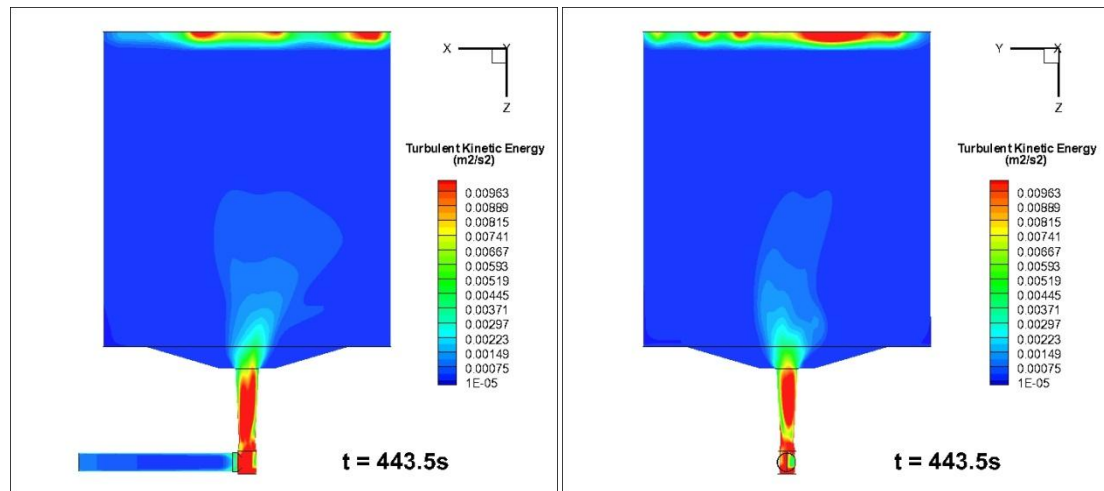
(a) 50% Open, Plane XZ   (b) 50% Open, Plane YZ

Figure 3.16 Turbulent Energy of Steel Phase at t=443.5 on **XZ** and **YZ** Planes (50% Open)

Because the previous researchers have found that the radial velocity greatly affected the flow pattern of the steel phase in the ingot causing entrainment of mold flux and air, the radial velocity distribution for 50% open at the different heights of the ingot mold was plotted using data from different vertical positions on the diameters of the round ingot cross sections (Figure 3.17). The three heights were set at 0.05m, 0.25m, and 0.75m, which represent the bottom, middle (through the region of swirling flow), and top cross section of the ingot. The diameter of x=0 and y=0 represent the centerline of the

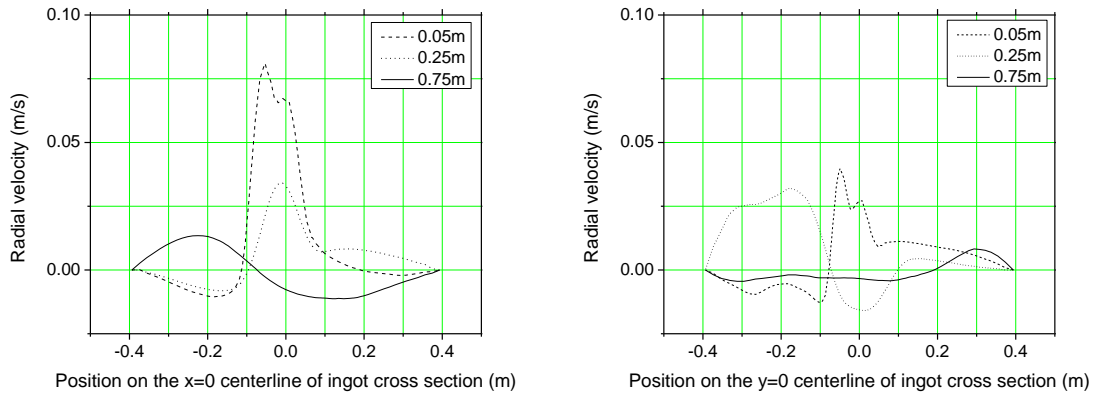cross section which was perpendicular to the inlet and parallel to the direction of flow from the inlet.
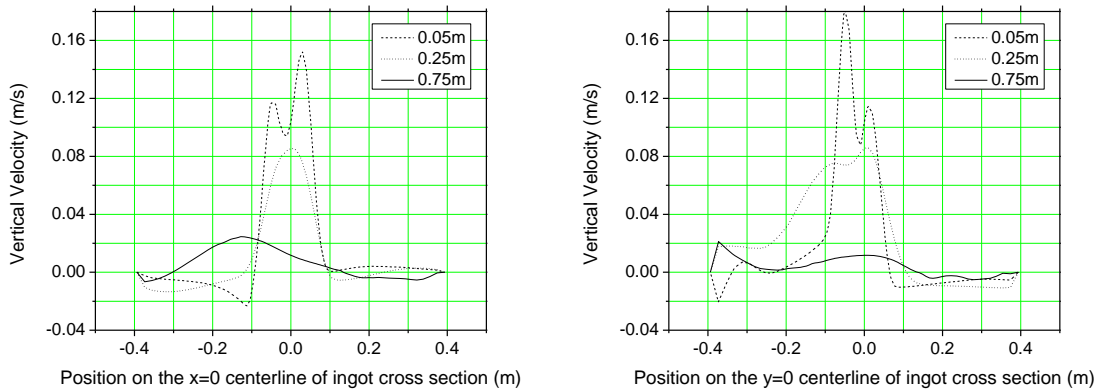

Figure 3.17 Radial Velocity Distributions at Different Heights on the Centerline (x=0, y=0) of the Ingot Cross Section (50% Open)

As shown in the Figure 3.17, the radial velocities are much higher near the center of the X axis with 0.05m height, and the distributions on centerline x=0 and y=0 are similar in the curve shape. This indicates a rough symmetrical flow pattern along the cross section of the ingot bottom. In the middle of the ingot, the peak of the curve still appears near the center area in Figure 3.17(a) at x=0 centerline, but due to the half open shape of the runner, the value of velocities were higher in the negative region of the X axis than in of the positive region. However, in Figure 3.17(b), the center range on the X axis has negative values of velocities with two positive peaks near the side. The much higher positive velocities on the negative X axis were caused by the inlet velocity which was in the same direction of this radial velocity. The velocity distribution on the cross section at a height 0.75m is more even than that of bottom and middle cross sections. This is expected because the velocity of the steel phase was reduced as the molten steel traveled from the bottom to the top.

As shown in Figure 3.18, the vertical velocity distributions at the height of 0.05m are similar to that of radial velocity distributions, and two peaks appears at the center

range of the X axis caused by the swirling flow. However, on the cross section at height 0.25m and 0.75m, peaks are found on the curve of y=0 centerline at the wall of the ingot (negative end of the X axis), which means that the liquid steel flows at a high flow rate near the ingot wall. In Figure 3.19, turbulent energy was much higher at the center range of the X axis at the cross section of height 0.05. With the height increasing, the curve of turbulent energy evens out. At the height of 0.75m, near the top surface, the turbulent energy was quite low compared to that of 0.25m and 0.05m heights. Nevertheless, the high turbulent kinetic energy illustrated in Figure 3.19 could be explained by the strong motion of molten steel at the top surface.

Figure 3.18 Vertical Velocity Distributions at Different Heights on the Centerline (x=0, y=0) of the Ingot Cross Section (50% Open)
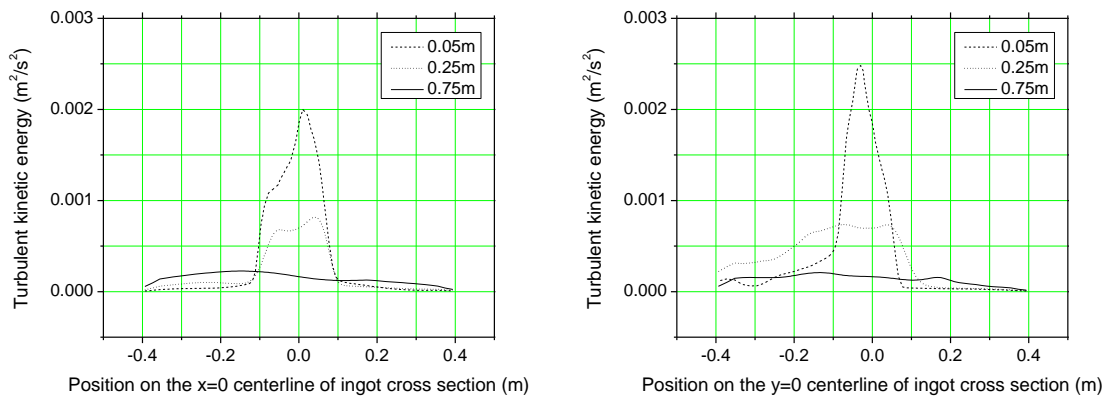
Figure 3.19 Turbulent Kinetic Energy Distributions at Different Heights on the Centerline (x=0, y=0) of the Ingot Cross Section (50% Open)

3.4.3. Comparison of Transient Phenomena of Flow Pattern between 50% Open and Whirlgate. Considering the fact that 50% open and whirlgate has better result at 5.0 seconds, these two cases were examined at 414 seconds in this part. As shown in Figure 3.20, at t=414s 50% open has a strong swirling flow at the center of ingot bottom with more asymmetric distribution comparing to whirlgate; however, whirlgate system does not have positive effect on reducing the size of turbulence flow.
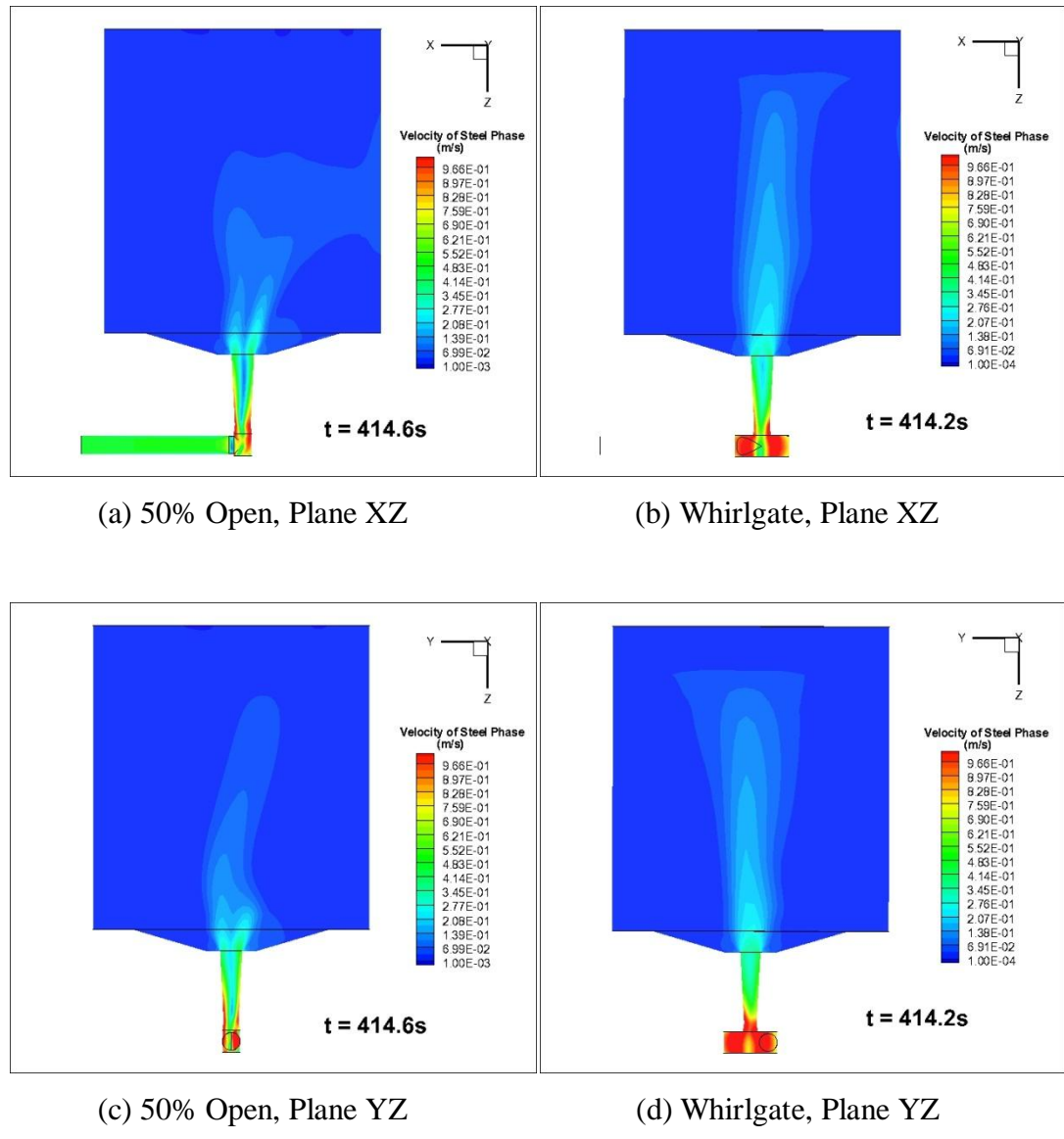
(a) 50% Open, Plane XZ   (b) Whirlgate, Plane XZ

(c) 50% Open, Plane YZ   (d) Whirlgate, Plane YZ

Figure 3.20 Velocity Contours of Steel Phase at t=414s on XZ and YZ Planes

Moreover, the turbulence area with higher velocity in the whirlgate case has no symmetrical distribution as did the 50% open case to indicate a swirling flow. Therefore, 50% open shows a smaller turbulence flow with swirling at the center of ingot bottom at the end point of filling process. The turbulent kinetic energy was examined at 414s on XY and YZ plane in Figure 3.21.

(a) 50% Open, Plane XZ   (b) Whirlgate, Plane XZ

(c) 50% Open, Plane YZ   (d) Whirlgate, Plane YZ
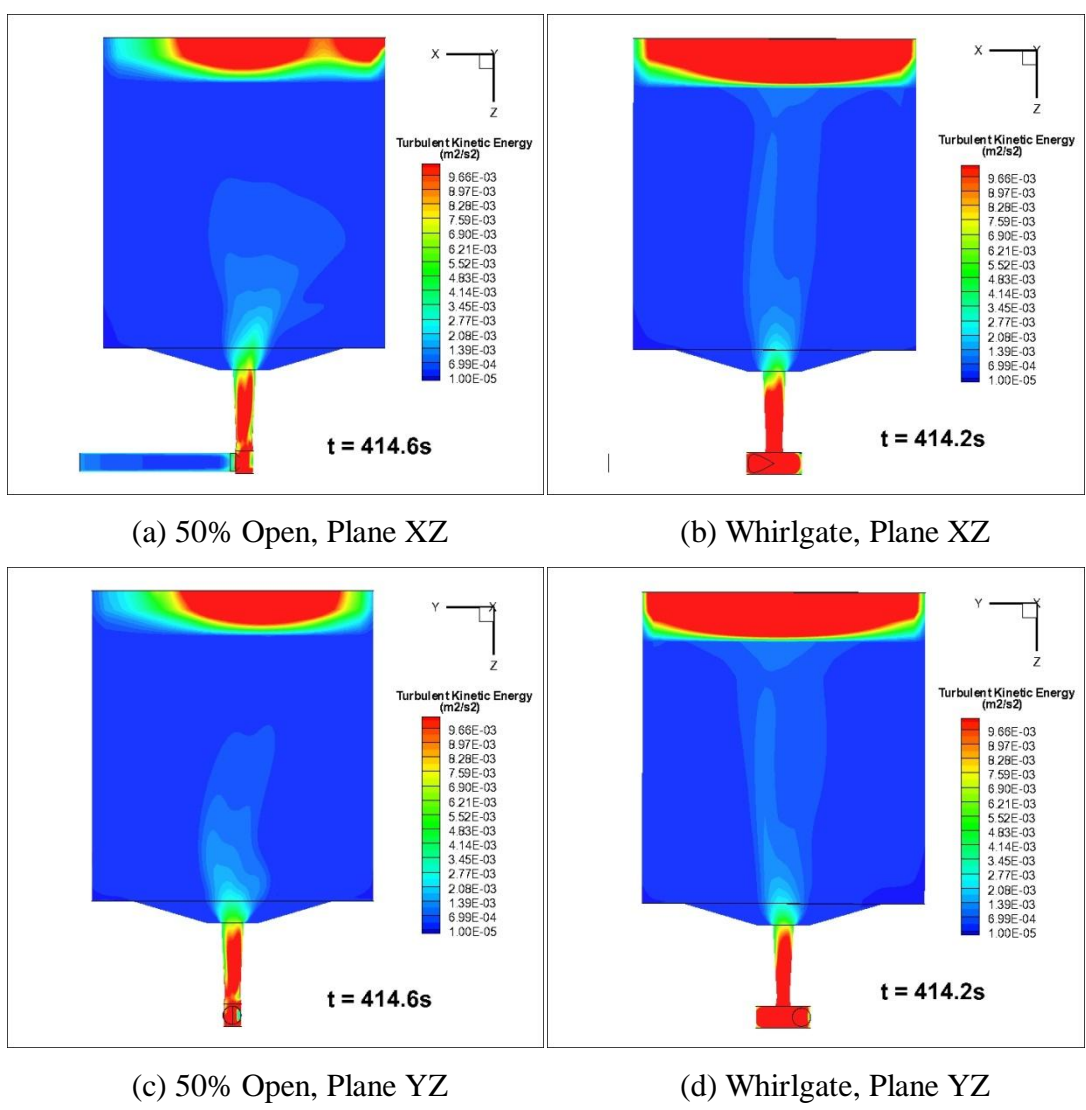
Figure 3.21 Turbulent Energy Contours of Steel Phase at t=414s on XZ and YZ Planes

In Figure 3.21, higher turbulent energy was distributed mainly at the top of the ingot and the upgate system both in 50% open and whirlgate. Also, high turbulent energy was illustrated along the area where swirling flow with high velocity was distributed compared to other areas in the ingot. Furthermore, the areas with high turbulent energy in the whirlgate ingot were larger than that in 50% open at the top of the ingot and the center of ingot bottom. Turbulent energy at cross sections was shown in Figure 3.22.
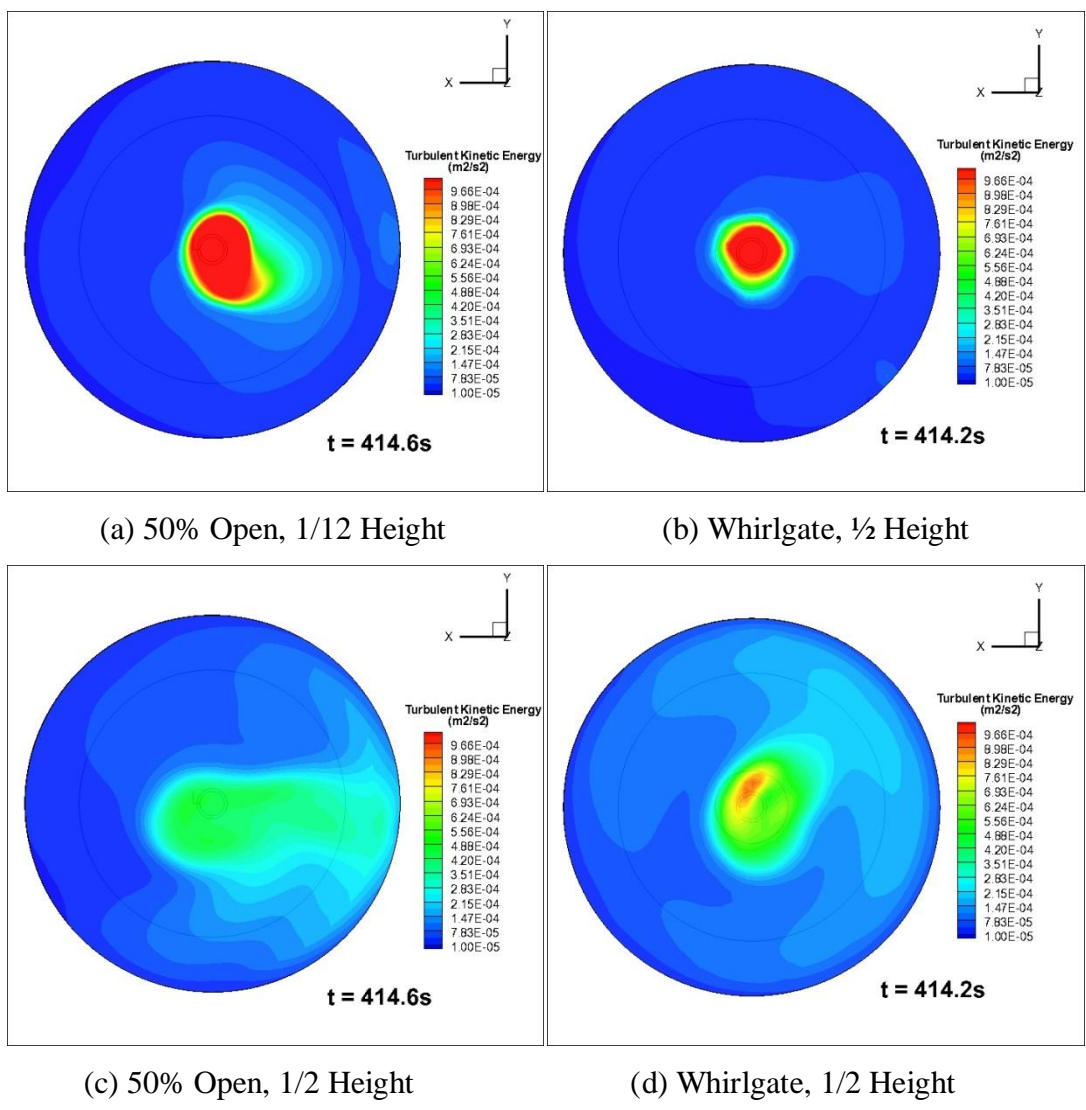
(a) 50% Open, 1/12 Height   (b) Whirlgate, ½ Height

(c) 50% Open, 1/2 Height   (d) Whirlgate, 1/2 Height

Figure 3.22 Turbulent Energy Contours of Steel Phase at t=414s on XY Planes with Different Height
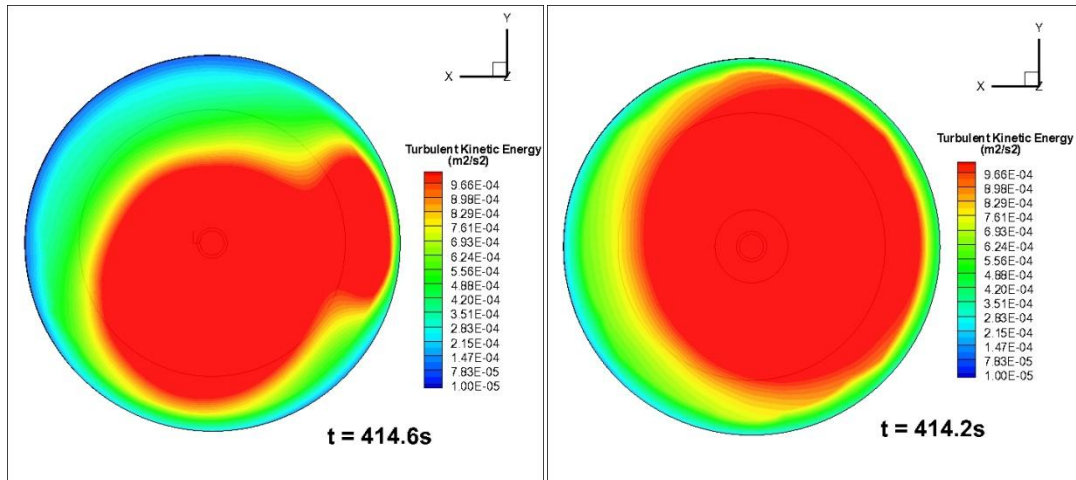
(e) 50% Open, 15/16 Height   (f) Whirlgate, 15/16 Height

Figure 3.22 Turbulent Energy Contours of Steel Phase at t=414s on XY Planes with Different Height (Cont.)

Turbulent energy distributions were demonstrated at 1/12, 1/2 and 15/16 of the total height of the ingot mold. There were no distinct difference in the comparison between 50% open and whirlgate, especially at the bottom and the middle height. However, it is apparent that at the top 50% open has a smaller turbulence area comparing to whirlgate but a more asymmetric turbulent energy distribution at the middle height.

Therefore, in order to check the effects of 50% open and whirlgate in the process of filling, velocity vectors and contours of turbulent energy of the steel phase at around 58 seconds were illustrated in Figure 3.23 and 3.24 also with three different heights in the ingot.

On the XY plane, the liquid steel in whirlgate tends to have a more even distribution of velocity than that of 50% open. From Figure 3.23, a stronger upward swirl can be seen on the XY plane of 50% open, which causes an area with higher velocity of vectors distributed at the center of the XY plane compared to whirlgate. In this area of high speed and swirling flow pattern, asymmetrical velocity distribution is observed due to the half-open design for the upgate bottom. Whirlgate has better symmetry of velocity distribution with little variation in most of the areas on the XY plane except at the boundary which is higher when compared to 50% open; moreover, 50% open has less non-continuous flow and less turbulence along the side wall.
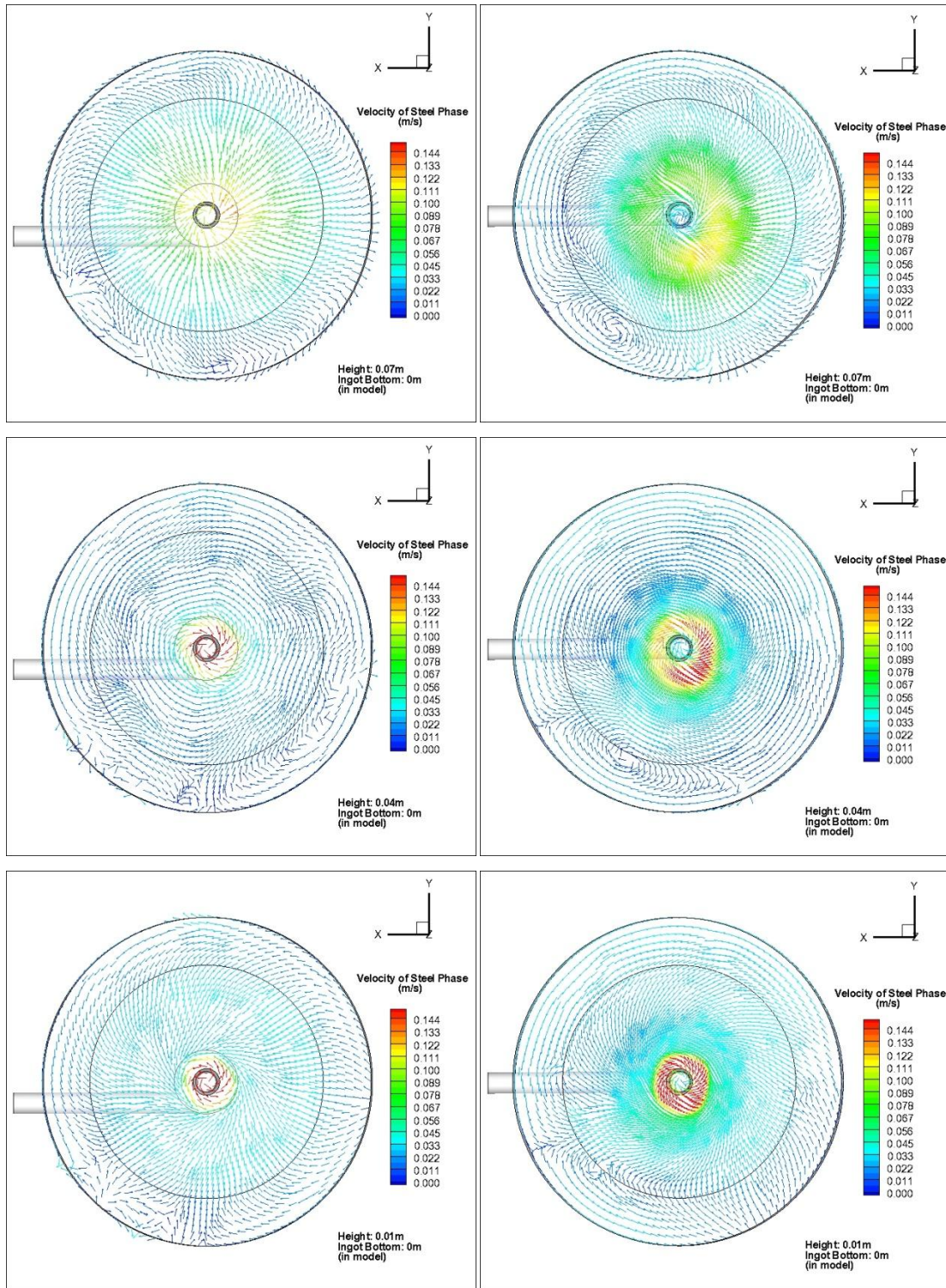
(Column A) Case 4: t = 58.6s   (Column B) Case 2: t = 56.8s

Figure 3.23 Velocity Vectors of Steel Phase at t=56.8s for 50% Open and at t=58.6s for Whirlgate on XY Plane with Different Heights
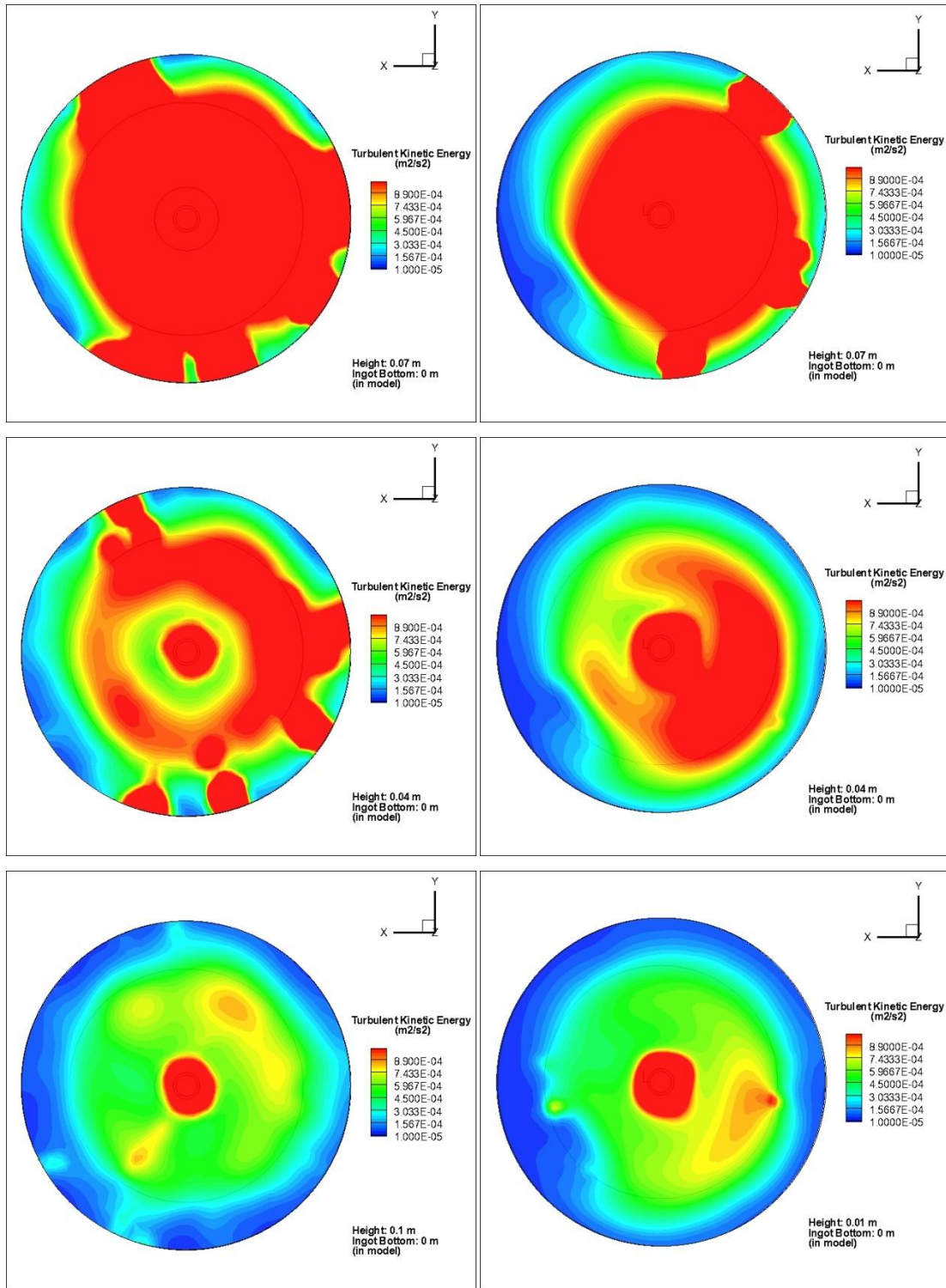
(Column A) Case 4: t = 58.6s   (Column B) Case 2: t = 56.8s

Figure 3.24 Turbulent Energy of Steel Phase at t=56.8s for 50% Open and at t=58.6s for
Whirlgate on XY Plane with Different Heights

Both in 50% open and whirlgate, high turbulent energy is found near the wall at the height of 0.07. As shown in Figure 3.24, the contour profile of turbulent energy at height 0.07m is near the top of the steel phase where higher turbulent energy is reasonable. Moreover, whirlgate has more severe turbulent flows at the top of ingot. At the height of 0.04, higher turbulent energy is distributed at the mid-radius locations in whirlgate; however, 50% open tends to have a similar distribution of turbulent energy according to the velocity vector. This difference influences the distribution of inclusions. Although whirlgate has a more widespread swirl at the bottom of the ingot, the distribution of high turbulent energy is in a smaller area compared to 50% open.

When the radial velocity of steel phase was plotted in Figure 3.25, the result shows that the distribution of radial velocity at the plane of z=0.05m in the two cases shows that Case 4 has more symmetric velocity distribution at x=0 centerline than that of Case 2. Also, they have similar distribution of radial velocity at y=0 centerline.
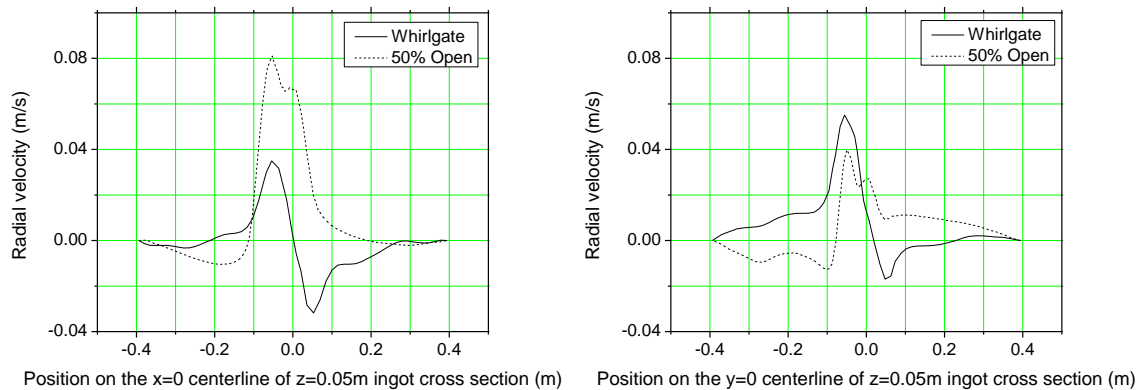
Figure 3.25 Radial Velocity Distributions at Different Heights on the Centerline (x=0, y=0) of the Ingot Cross Section (50% Open and Whirlgate)

In conclusion, the smaller volume and area of the upgate cross section (50% open) gives a higher velocity in the molten steel phase and a stronger recirculation flow but in a smaller region. This affects the overall flow pattern in the ingot. A strong swirl is generated along the side wall. The steel phase has more turbulent flows in the center of

the ingot. On the other hand, the swirl-modified high-volume upgate bottom generates flows with more even but higher velocity at the center and less turbulence except at the top of the steel phase.

3.4.4. Study of Slag Phase Motion in Whirlgate Case. To understand the behavior of the mold flux which was used to protect the molten steel from re-oxidation and heat isolation, the process of the mold flux adding was simulated. In detail, one bag of mold flux will be hanging upon the rising molten steel near inlet. Once the liquid steel reached the bag, the mold flux will be released onto the top of the steel phase with the bag burned up. The mold flux would be melted and one slag layer would be formed and covered the top of the molten steel.

Considered that whirlgate case has a strong turbulence at the top of the steel phase, the case running at 16.55s of whirlgate was chosen to be the simulation case. For simplicity, initially a spherical mold powder lump would be set above the steel phase in simulation with slag fluid properties. The mold powder would drop down and interacted by the fluid motion of molten steel. With the steel phase continuously rising up, the mold flux would stay at the top of the steel phase due to lower density. The main parameters used in this case are listed in Table 3.9.

Table 3.9 Main Parameters of Slag Simulation

Parameter	Value	Parameter	Value
Density of slag	4500 kg/m^3	Radius of Region	0.08m
Viscosity of slag	0.22 kg/m·s	Surface tension (Slag/Air)	1.0 N/m
Surface tension (Slag/Steel)	1.4 N/m	Surface tension (Steel/Air)	1.89 N/m

Figure 3.26 demonstrates the process of powder dropping and slag layer formation. With the slag phase dropping, the steel phase fluctuated and bounced back when it reached the side wall of ingot due to the gravity effect. This provides the possibility of air entrainment in the process of powder dropping. A slag layer formed approximately 20 seconds after the mold powder mixed with molten steel.

(a) t=16.55s   (b) t=16.95s

(c) t=18.05s   (d) t=46.075s
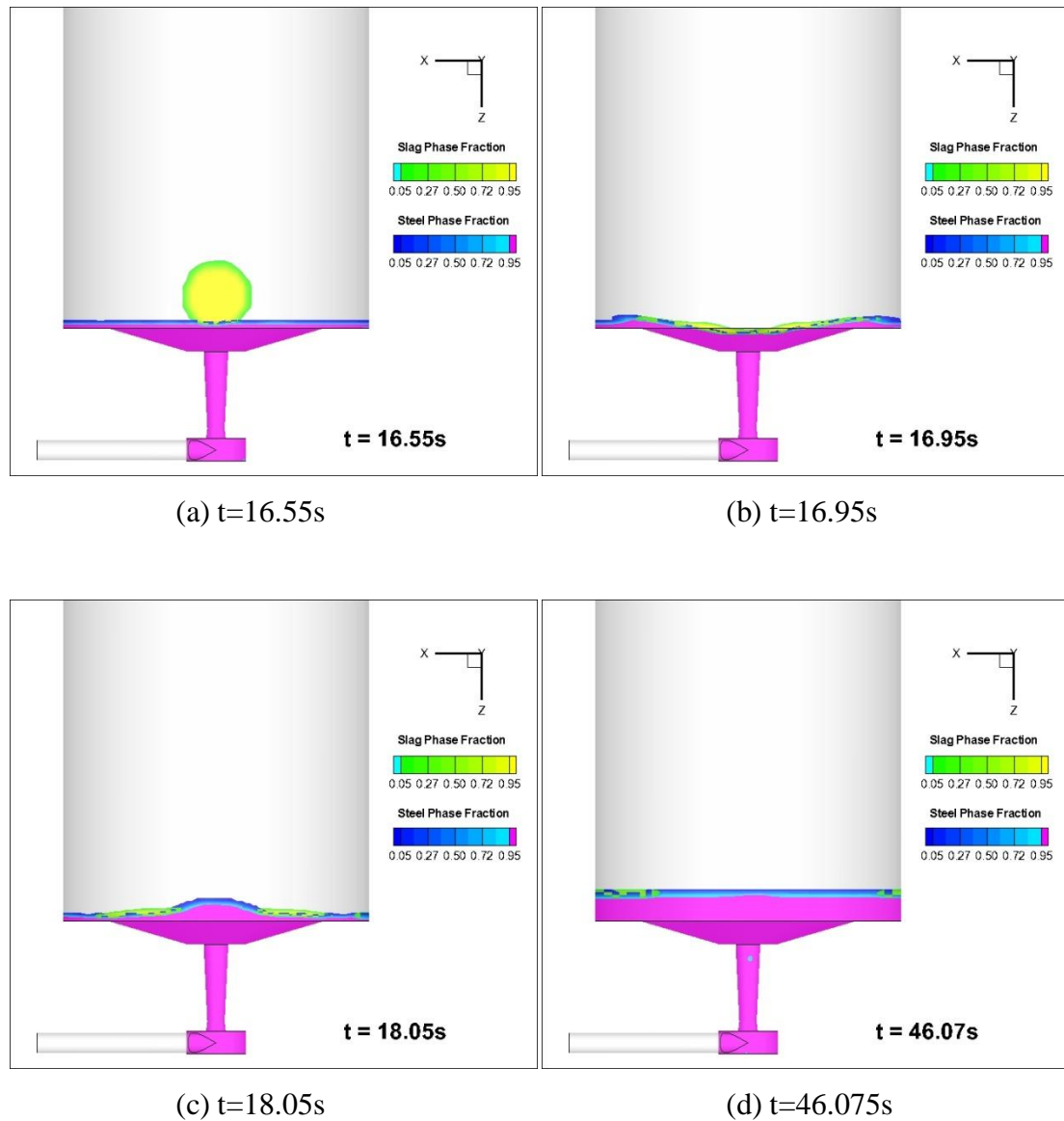
Figure 3.26 Slag Phase and Steel Phase Fraction on XZ Plane in Whirlgate

Due to the low addition of mold powder in this simulation, the slag phase was not fully covered above the steel phase once the slag phase became stable. Liquid steel flowed from the center of the top face to the boundary of the ingot and pushed the mold powder to the side wall. In Figure 3.27, the iso-surfaces of slag phase were shown at different times with different volume fractions.
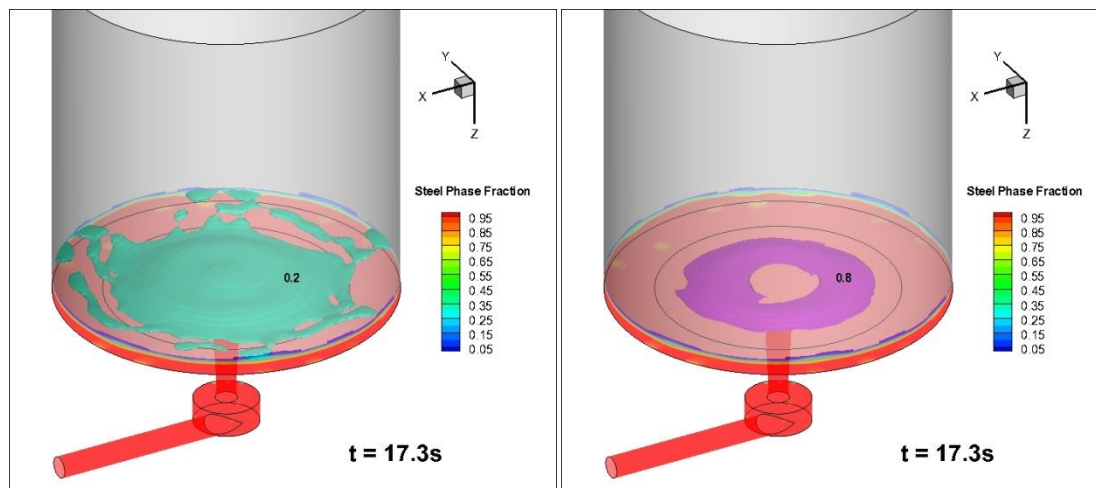
(a) t=17.3s, Slag Phase Fraction=0.2   (b) t=17.3s, Slag Phase Fraction=0.8
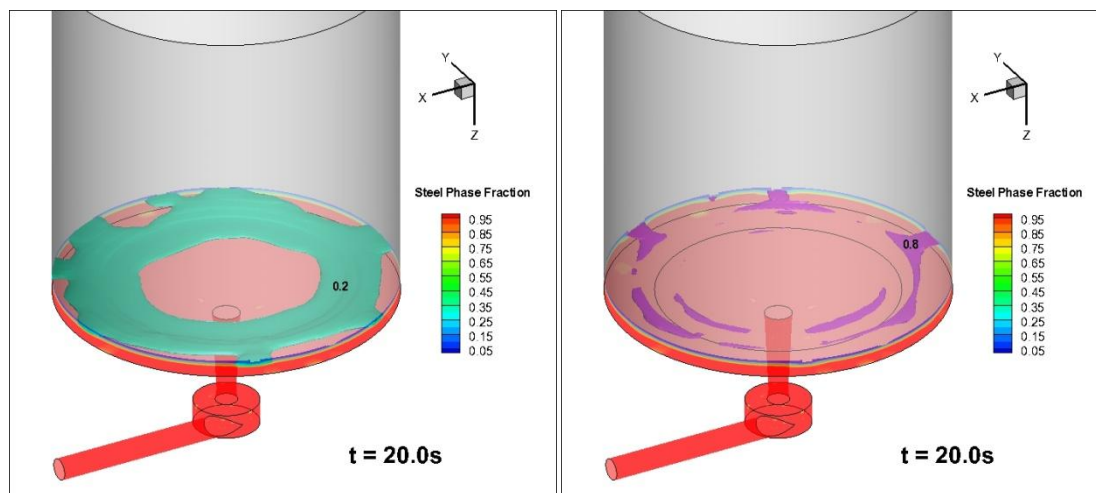
(c) t=20.0s, Slag Phase Fraction=0.2   (d) t=20.0s, Slag Phase Fraction=0.8
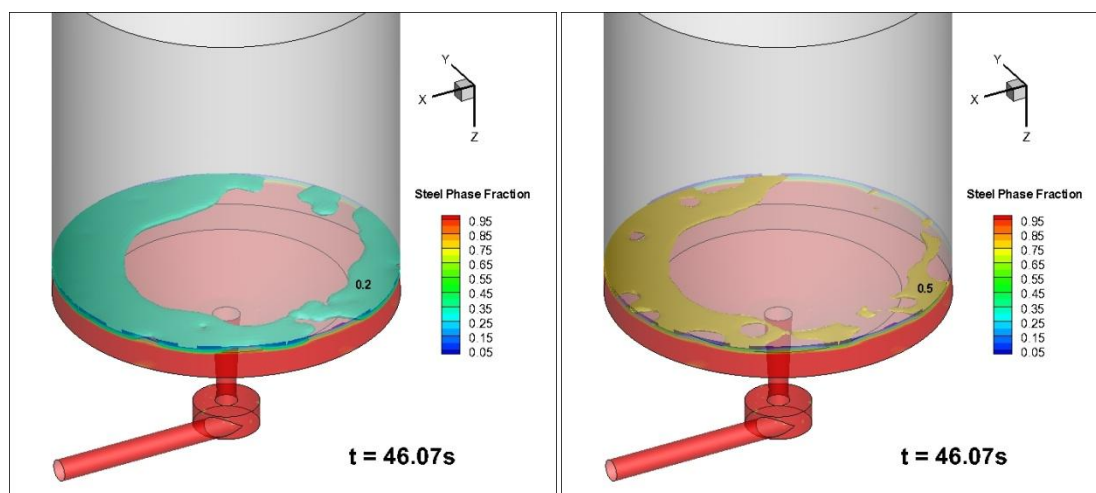
(e) t=46.07s, Slag Phase Fraction=0.2   (f) t=46.07s, Slag Phase Fraction=0.5

Figure 3.27 Iso-Surface of Slag Phase Fraction at t=17.3s, 20.0s, 46.07s

A few seconds after the mold flux dropped onto the molten steel, the slag phase was mainly covered at the center of the top surface of steel like Figure 3.27 (a) and (b). But with molten steel rising up, when the slag phase turned to be stable, most of the mold flux was distributed by interaction with fluid motion of the steel phase at the locations near side wall. At 46 seconds, the slag phase with a volume fraction higher than 0.6 could not be found above the steel phase. This indicates the mixing interaction between the slag and the steel phase is time-dependent.

As a result, air entrainment and the amount of mold powder added are the main factors that affect the protection during ingot casting. With higher amounts of mold powder added, more severe air entrainment takes place. However, if the slag phase is not large enough, the center part of the top face of steel phase will be exposed to air. Thus, an appropriate quantity of mold powder is important to generate an efficient protection layer.

3.5. SUMMARY

By using re-designed upgate systems, swirling and recirculation flows were intentionally generated, which reduced the size of disturbance of molten steel free surface and formed even flows of liquid steel in the ingot.

The ingot with the original upgate has strong turbulence with high velocity distributed at the top surface of rising steel phase. 75% open has a better result compared to original case but still was similar in turbulent energy and velocity distribution.

Generally, in the 50% open and whirlgate cases, turbulent energy is higher at the center and top face of the ingot filled with molten steel. The steel phase flowed upwardly from the inlet to the top of the ingot and then went along the side wall to form asymmetric swirling and recirculation flows. Eddies were found inside the ingot and upgate system.

In the whirlgate case, the swirling flow was examined with higher velocity and larger size at the ingot bottom compared to 50% open. The whirlgate case also has more area with higher turbulent energy on the top surface and turbulence flow near the side

wall. But the 50% open case has a more asymmetrical distribution of turbulent energy and velocity in the steel ingot, which was negative to the fluid flow motion.

The motion of the slag phase was investigated in the process of adding mold powder and the formation of the top protection layer. It is important to determine the optimum addition of mold powder to achieve better reoxidation protection and reduce air entrainment.

4. CONCLUSIONS AND RECOMMENDATIONS

4.1. CONCLUSIONS

This research has led to the following conclusions:

1. In CFD modeling, four simulations were preceded with different upgate systems including original, 50% open, 75% open and whirlgate. The results showed that 75% open case did not have a distinctive effect of improving the fluid flow pattern and reduce the disturbance of steel phase free surface compared to the original case. 50% open and whirlgate did greatly affect the flow pattern to have less turbulence with lower velocity and more even velocity distribution in the ingot especially near the top surface of steel phase. In addition, 50% open has a better turbulence control but a more asymmetrical velocity distribution of the swirling flow.

2. Based on the observation results under optical microscope of steel samples, more inclusions are found in the ingot with a traditional upgate. By using the parameter of area ratio between inclusions and total area observed, the actual inclusion population on the steel samples was revealed. The swirl-modified ingot tended to have fewer inclusions in the size of 0~8µm, but no significant difference on the inclusions at a size larger than 10 µm, which was due to the large amount of silica contamination particles found on the samples. This was most likely because it was hard to remove the oxidized surface on the raw material of steel samples from swirl-modified ingot. Along the radial direction of ingot, fewer inclusions were detected at the boundary for both samples from traditional and swirl-modified ingot. The center part of traditional ingot had much higher inclusion area ratio than that of mid-radius and boundary; however, no apparent regular pattern was found for swirl-modified ingot. This was confirmed by the simulation showing high turbulent energy in the center at the top and bottom but not in the mid-radius at the middle height of ingot. For different heights, the top of the ingot tended to have more inclusions than other regions. At positions of 1/3 height and 2/3 height,

the area ratio of inclusions was close, and the bottom of swirl-ingot had the lowest amount of inclusions observed.

3. Six types of inclusions were classified: oxide, sulfide, oxide with sulfide shell, strip form of oxide-sulfide, alumina based multiphase inclusion, Al_2O_3 chunk cluster. Oxide inclusions always contained high content of alumina accompanied with CaO, SiO_2, MnO, MgO, which formed during solidification at around 1800K. TiO_2 was also detected in oxide inclusions. Sulfide was mainly MnS with low content of CaS. When temperature goes down to around 1500K, sulfide precipitates on nuclei like oxide particles or exogenous inclusions with the growth of oxide particles to form oxide-sulfide and multiphase inclusions. The comparison between the results from ingot with traditional and swirl-modified upgate system gave a basic conclusion. It indicates that the swirling flow generated by intention decreased the formation of sulfides and oxides but introduced in other types of inclusions as multiphase inclusions and alumina cluster.

4.2. RECOMMENDATIONS AND FUTURE WORK

More industrial trials are needed to give comprehensive comparisons with simulations. Water modeling is also necessary to verify the mathematical simulation with the industrial trials. For inclusions, if time is allowed, more SEM inclusion analysis could be taken place to systematically compare the results between SEM and ASPEX.

APPENDIX A.

SAMPLE PAGE OF OPTICAL OBSERVATION RESULT
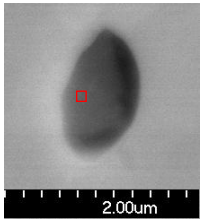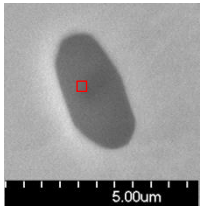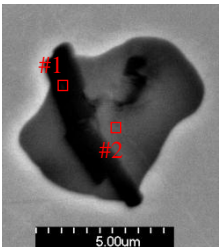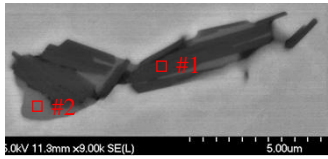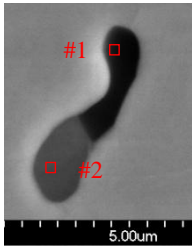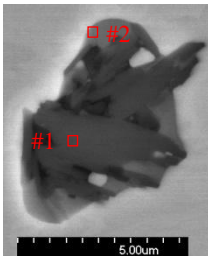
Inclusion figures are captured and listed for all 72 steel samples.

Figures of inclusions in steel sample of 77C_X3 are shown below:
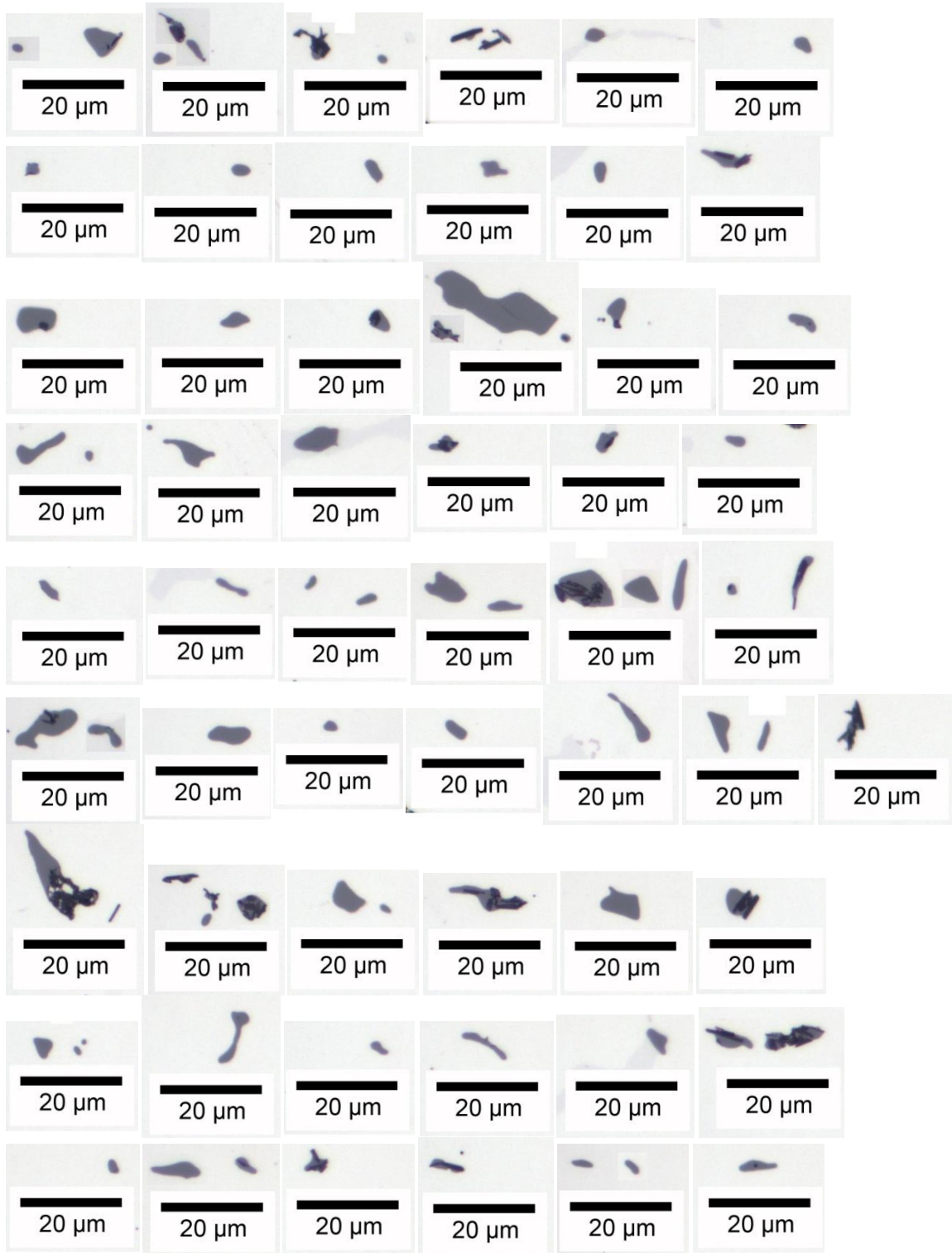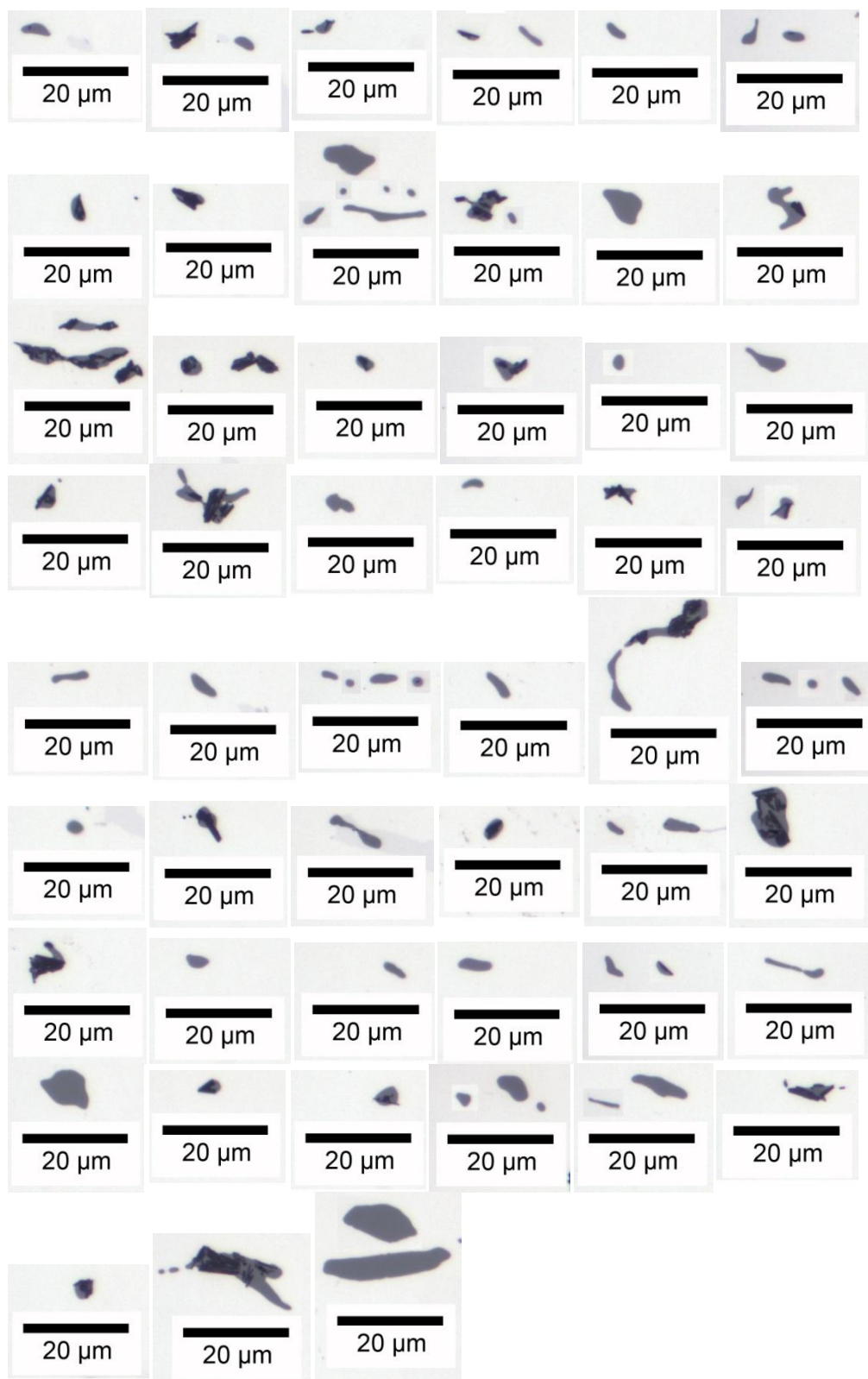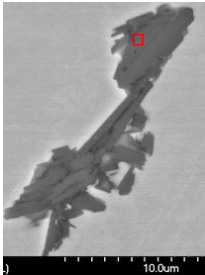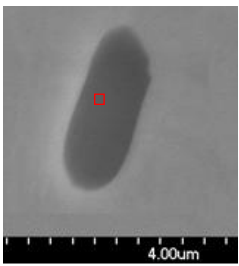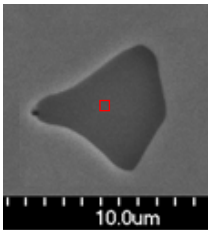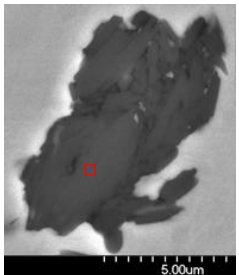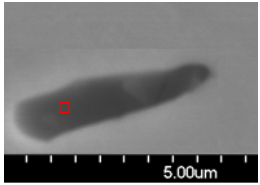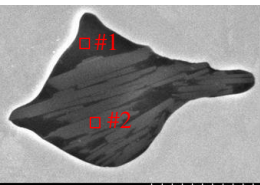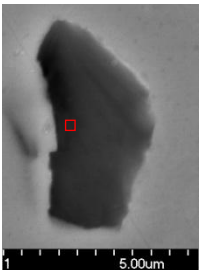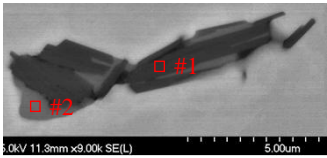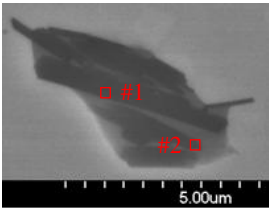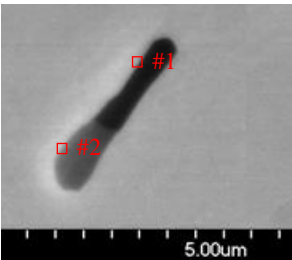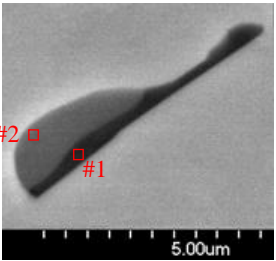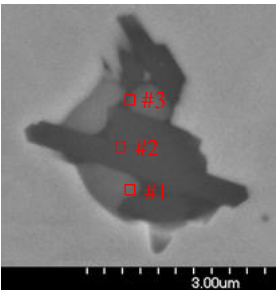
APPENDIX B.

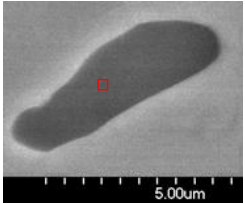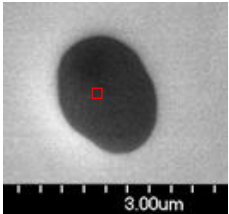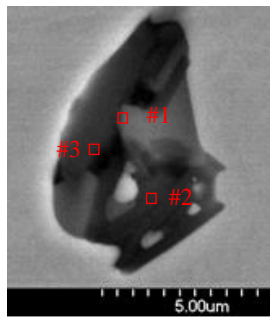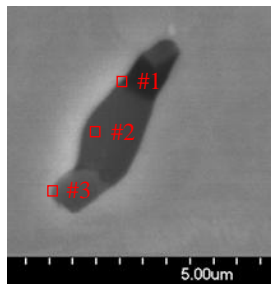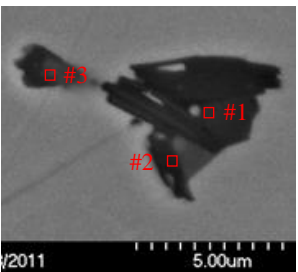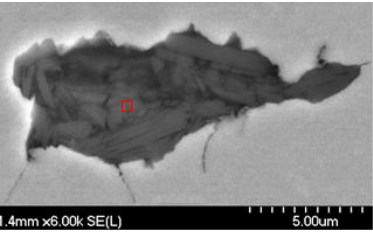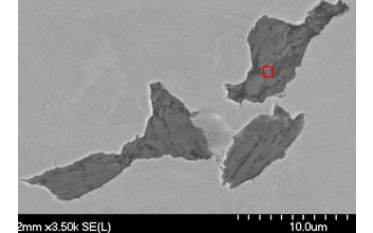LIST OF INCLUSIONS FROM SEM-EDS DETECTION

	Al_2O_3: 42.8%, MnO: 27.5%, SiO_2: 15.7%, TiO: 6.1%, CaO: 4.3%, MgO: 3.8%
	MnS: 52.8%, MnO: 0, CaS: 0, Al_2O_3: 27.1%, SiO_2: 1.4%, TiO: 0, MgO: 2.8%, CuO: 2.4%, [S]: 13.6%
	#1) MnS: 8.3%, MnO: 0, CaS: 3.2%, CaO: 0, Al_2O_3: 82.4%, SiO_2: 1.6%, TiO: 0.7%, MgO: 1.7%, [S]: 2.0% #2) MnS: 35.0%, MnO: 0, CaS: 2.3%, CaO: 0, Al_2O_3: 42.8%, SiO_2: 0.5%, TiO: 0.4%, MgO: 0.7%, [S]: 18.2%
	#1) MnS: 9.4%, MnO: 0, CaS: 2.0%, CaO: 4.6%, Al_2O_3: 78.9%, SiO_2: 2.7%, TiO: 0.4%, MgO: 1.7%, #2) MnS: 34.1%, MnO: 0, CaS: 5.2%, CaO: 0, Al_2O_3: 42.5%, SiO_2: 1.6%, TiO: 0.5%, MgO: 1.4%, [S]: 13.7%, CuO: 0.6%
	#1) MnS: 1.1%, MnO: 17.8%, CaO: 13.3%, Al_2O_3: 16.2%, SiO_2: 46.7%, TiO: 0.2%, MgO: 4.8%, [Mo]: 0.29AT% #2) MnS: 74.1%, MnO: 0, CaS: 1.5%, Al_2O_3: 2.0%, SiO_2: 2.9%, TiO: 0.1%, MgO: 0.2%, [S]: 19.2%
	#1) MnS: 1.7%, MnO: 0, CaS: 1.1%, CaO: 4.3%, Al_2O_3: 84.8%, SiO_2: 4.3%, TiO: 0.4%, MgO: 2.5%, [Mo]: 1.2AT% #2) MnS: 36.0%, MnO: 0, CaS: 6.0%, Al_2O_3: 39.0%, SiO_2: 3.2%, TiO: 0.7%, MgO: 1.2%, [S]: 12.4%

	Al$_2$O$_3$: 80.5%, CaO: 6.9%, MnS: 2.0%, MnO: 0.3%, SiO$_2$: 6.3%, MgO: 2.6%, CuO: 0.7%, Na$_2$O: 0.6%
	MnS: 67.6%, CaS: 0.6%, Al$_2$O$_3$: 3.2%, MgO: 1.0%, SiO$_2$: 0.9%, TiO$_2$: 0.3%, CaO: 0%, [S]: 25.6%
	MnS: 72.1%, CaS: 0.2%, Al$_2$O$_3$: 1.1%, MgO: 0.4%, SiO$_2$: 1.0%, TiO$_2$: 0.3%, CaO: 0%, [S]: 23.5%
	MnS: 64.7%, CaS: 0.9%, Al$_2$O$_3$: 10.4%, MgO: 1.5%, SiO$_2$: 1.2%, TiO$_2$: 0.2%, CaO: 0%, [S]: 21.0%
	MnS: 67.7%, CaS: 2.3%, Al$_2$O$_3$: 1.6%, MgO: 1.3%, SiO$_2$: 0.4%, TiO$_2$: 0.1%, CaO: 0%, [S]: 25.8%
	Al$_2$O$_3$: 88.6%, MnS: 0.6%, SiO$_2$: 2.2%, TiO: 0%, CaO: 5.1%, MgO: 2.8%, MnO: 0

Al_2O_3: 9.8%, MnS: 1.1%, SiO_2: 58.3%, TiO: 0%, CaO: 6.7%, MgO: 1.7%, MnO: 22.3%

#1) Al_2O_3: 44.0%, CaO: 27.1%, SiO_2: 24.0%, MgO: 2.3%, MnS: 0.3%, MnO: 2.2%
#2) Al_2O_3: 93.2%, CaO: 0%, SiO_2: 4.5%, MgO: 1.8%, MnS: 0.3%, MnO: 0.2%

Al_2O_3: 85.7%, MnS: 1.0%, SiO_2: 6.0%, TiO: 0.5%, CaO: 4.0%, MgO: 1.6%, MnO: 0.5%

#1) MnS: 9.4%, MnO: 0, CaS: 2.0%, CaO: 4.6%, Al_2O_3: 78.9%, SiO_2: 2.7%, TiO: 0.4%, MgO: 1.7%,
#2) MnS: 34.1%, MnO: 0, CaS: 5.2%, CaO: 0, Al_2O_3: 42.5%, SiO_2: 1.6%, TiO: 0.5%, MgO: 1.4%, [S]: 13.7%, CuO: 0.6%

#1) MnS: 7.9%, MnO: 0, CaS: 5.4%, CaO: 0.9%, Al_2O_3: 81.7%, SiO_2: 1.0%, TiO: 0.7%, MgO: 2.1%,
#2) MnS: 22.4%, MnO: 0, CaS: 26.3%, CaO: 0, Al_2O_3: 38.3%, SiO_2: 1.0%, TiO: 0.3%, MgO: 1.6%, [S]: 9.5%

#1) MnS: 8.3%, MnO: 0, CaS: 3.2%, CaO: 0, Al_2O_3: 82.4%, SiO_2: 1.6%, TiO: 0.7%, MgO: 1.7%, [S]: 2.0%
#2) MnS: 35.0%, MnO: 0, CaS: 2.3%, CaO: 0, Al_2O_3: 42.8%, SiO_2: 0.5%, TiO: 0.4%, MgO: 0.7%, [S]: 18.2%

#1) MnS: 40.9%, MnO: 0, CaS: 7.1%, CaO: 0, Al_2O_3: 20.2%, SiO_2: 5.0%, TiO: 1.1%, MgO: 1.0%, Na_2O: 1.1%, CuO: 5.1%, [S]: 17.6%
#2) MnS: 51.3%, MnO: 0, CaS: 7.6%, CaO: 0, Al_2O_3: 14.7%, SiO_2: 2.9%, TiO: 0.1%, MgO: 0.3%, CuO: 2.5%, [S]: 20.4%

#1) MnS: 18.4%, MnO: 0, CaS: 6.5%, CaO: 0, Al_2O_3: 59.5%, SiO_2: 2.3%, TiO: 0.3%, MgO: 2.7%, [S]: 9.6%
#2) MnS: 6.1%, MnO: 0, CaS: 7.8%, CaO: 0, Al_2O_3: 74.9%, SiO_2: 5.5%, TiO_2: 0.3%, MgO: 5.0%
#3) MnS: 2.2%, MnO: 0, CaS: 3.7%, CaO: 1.6%, Al_2O_3: 84.8%, SiO_2: 4.9%, TiO_2: 0.3%, MgO: 2.2%

#1) MnS: 28.0%, MnO: 18.0%, CaS: 0%, CaO: 4.2%, Al_2O_3: 6.1%, SiO_2: 41.1%, TiO: 1.3%, MgO: 1.3%
#2) MnS: 75.1%, MnO: 0, CaS: 0.6%, CaO: 0, Al_2O_3: 1.4%, SiO_2: 2.8%, TiO_2: 0.1%, MgO: 0.4%, [S]: 19.5%
#3) MnS: 68.5%, MnO: 0, CaS: 1.1%, CaO: 0%, Al_2O_3: 16.6%, SiO_2: 5.8%, TiO_2: 1.6%, MgO: 1.0%, [S]: 5.4%

#1) MnS: 3.7%, MnO: 3.3%, CaS: 0%, CaO: 1.6%, Al_2O_3: 75.0%, SiO_2: 0.8%, TiO: 0.4%, MgO: 15.3%
#2) MnS: 19.8%, MnO: 0, CaS: 2.6%, CaO: 0, Al_2O_3: 61.3%, SiO_2: 1.5%, TiO_2: 0.3%, MgO: 6.6%, [S]: 7.9%
#3) MnS: 54.3%, MnO: 0, CaS: 1.5%, CaO: 0, Al_2O_3: 25.8%, SiO_2: 2.1%, TiO_2: 0.2%, MgO: 1.6%, [S]: 14.4%

#1) MnS: 2.0%, MnO: 0, CaS: 0.6%, CaO: 7.9%, Al_2O_3: 75.9%, SiO_2: 5.7%, TiO: 0, MgO: 7.8%
#2) MnS: 1.2%, MnO: 0, CaS: 2.2%, CaO: 6.9%, Al_2O_3: 83.6%, SiO_2: 4.1%, TiO_2: 0.3%, MgO: 1.6%
#3) MnS: 12.2%, MnO: 0, CaS: 10.2%, CaO: 3.2%, Al_2O_3: 67.4%, SiO_2: 5.5%, TiO_2: 0.3%, MgO: 1.1%

	Al$_2$O$_3$: 81.8%, MnS: 0.2%, SiO$_2$: 11.3%, TiO: 0.2%, CaS: 0, CaO: 4.3%, MgO: 1.7%, MnO: 0
	Al$_2$O$_3$: 60.2%, MnS: 0.5%, SiO$_2$: 21.8%, TiO: 0.1%, CaS: 0, CaO: 1.0%, MgO: 14.3%, MnO: 2.1%

BIBLIOGRAPHY

[1]   World steel committee, "Steel statistical yearbook 2011," *World Steel Association*, 2012

[2]   Danijela Anica Skobir, "The determination of steel cleanliness in the as-cast steel ingot 26NiCrMoV145," *Vaccum*, Vol. 84, 2010, 205-208

[3]   L. Zhang, B. Rietow, B.G. Thomas, K. Eakin, "Large inclusions in plain-carbon steel ingots cast by bottom teeming," *ISIJ International,* Vol. 46 (5),2006, 670-679.

[4]   L. Zhang and B.G. Thomas, "State of the art in the control of inclusions during steel ingot casting," *Metallurgical and Materials Transactions B: Process Metallurgy and Materials Processing Science,* Vol. 37 (5),2006, 733-761.

[5]   Lifeng Zhang, "State of art in evaluation and control of steel cleanliness," ISIJ International, Vol. 43, 2003, 3, 271-291

[6]   Lifeng Zhang, "Inclusion and bubble in steel – a review," *Journal of Iron and Steel Research International*, 2006, 13(3), 1-8

[7]   R. Dekkers, "Non-metallic inclusions in aluminum killed steels,"*Ironmaking & Steelmaking*, Dec 2002, 29, 6, 437-444.

[8]   L. Ragnarsson, "Inclusions generated during ingot casting of tool steel," *Steel Research Int.* 81(2010) No. 1, 40-47.

[9]   Joo Hyun Park, "Formation mechanism of spinel-type inclusions in high-alloy stainless steel melts," *Metallurgical and Materials Transactions*, Vol. 38B, August 2007, 657-663.

[10]   N. Tripathi and Du Sichen, "Chemical characterisation of non-metallic inclusions during casting of hot work die steel," *Ironmaking and Steelmaking*, Vol. 33, No. 3, 2006, 213-222.

[11]   H. Doostmohammadi, "Inclusion characteristics of bearing steel in a runner after ingot casting," *Steel Research Int.* 81(2010) No. 2, 142-149.

[12]   A. V. Dub, "Nonmetallic inclusions in low-alloy tube steel," *Metallurgist*, Vol. 49, 2005, Nos. 3-4

[13]   A. Gigovic-gekic, "Analyse and research of nonmetallic inclusions for steel 100Cr6," *Metalurgija*, Vol. 48, 2009, 1, 29-32

[14]   J. Cheng, R. Eriksson and P. Jonsson, "Determination of macroinclusions during clean steel production," *Ironmaking and Steelmaking*, Vol. 30, No. 1, 2003, 66-72.

[15]   R. Eriksson, L. Jonsson and P.G. Jönsson, "Effect of entrance nozzle design on the fluid flow in an ingot mold during filling," *ISIJ International*, Vol. 44 (8),2004, 1358-1365

[16]   L. Ragnarsson, "Flow pattern in ingot during mould filling and its impact on inclusion removal," Ironmaking and Steelmaking, Vol. 37, 2010, 5, 347-352

[17]   Line Hallgren, "Effect of nozzle type and swirl on flow pattern for initial filling conditions in the mould for up-hill teeming," Steel Research International, Vol. 78, 2007, 3, 254-259

[18]   Zhi Zhang, "A numerical study of swirl blade effects in uphill teeming casting," *ISIJ International*, Vol. 50, 2010, 12, 1756-1762

[19]   Line Hallgren, Shigeo Takagi, P. Jonsson, "Effect of nozzle swirl blade on flow pattern in runner during uphill teeming," *ISIJ International*, Vol. 46, No. 11, 2006, pp. 1645-1651

[20]   Z. Radovic, "Numerical simulation of steel ingot solidification process," *Journal of Materials Processing Technology*, Vol. 160, 2005, 156-159

[21]   N. M. Tanklevskaya, "Thermodynamic analysis of the formation of nonmetallic inclusions in 40KhGM steel with various sulfur contents,"*Russian Metallurgy*, Vol. 2009, No. 7, 642-643.

[22]   Youn-Bae Kang, "Particle application of thermodynamics to inclusions engineering in steel,"*Journal of Physics and Chemistry of Solids*, 2005, 219-225

[23]   E. A. Chichkarev, "Conditions for nonmetallic inclusion formation in steels deoxidized with aluminum and calcium,"*Metallurgist*, Vol. 53, 2009, Nos. 11-12

[24]   ASM handbook, Volume 15: Casting, *ASM International*, Vol. 15, 2008

[25]   Robert Eriksson, "Effect of entrance nozzle design on the fluid flow in an ingot mold during filling," ISIJ International, Vol. 44, 2004, 8, 1358-1365

VITA

Jun Ge was born in Zhejiang, China on May 4, 1985. He graduated from Central South University, Changsha, Hunan Province in China with a Bachelors Degree of Metallurgy Science and Engineering in 2007.

In September of 2010, he began his first semester of Master program in Department of Material Science and Engineering at Missouri University of Science and Technology.

In December 2012, he received his Master's degree in Material Science and Engineering from Missouri University of Science and Technology.